

Visual Quantification of the Circle of Willis in Stroke Patients

DIPLOMARBEIT

zur Erlangung des akademischen Grades

Diplom-Ingenieur

im Rahmen des Studiums

Medizinische Informatik

eingereicht von

Haichao Miao

Matrikelnummer 0726810

an der
Fakultät für Informatik der Technischen Universität Wien

Betreuung: Ao.Univ-Prof. Dipl.-Ing. Dr.techn. Eduard Gröller

Mitwirkung: Univ.-Prof. Prim. Dr. Christian Nasel

Dipl.-Ing. Dr.techn. Gabriel Mistelbauer

Wien, 23.04.2015

(Unterschrift Verfasser)

(Unterschrift Betreuung)

Visual Quantification of the Circle of Willis in Stroke Patients

MASTER'S THESIS

submitted in partial fulfillment of the requirements for the degree of

Diplom-Ingenieur

in

Medical Informatics

by

Haichao Miao

Registration Number 0726810

to the Faculty of Informatics
at the Vienna University of Technology

Advisor: Ao.Univ-Prof. Dipl.-Ing. Dr.techn. Eduard Gröller
Assistance: Univ.-Prof. Prim. Dr. Christian Nasel
Dipl.-Ing. Dr.techn. Gabriel Mistelbauer

Vienna, 23.04.2015

(Signature of Author)

(Signature of Advisor)

Erklärung zur Verfassung der Arbeit

Haichao Miao
Huttengasse 18/3/13, 1160 Wien

Hiermit erkläre ich, dass ich diese Arbeit selbständig verfasst habe, dass ich die verwendeten Quellen und Hilfsmittel vollständig angegeben habe und dass ich die Stellen der Arbeit - einschließlich Tabellen, Karten und Abbildungen -, die anderen Werken oder dem Internet im Wortlaut oder dem Sinn nach entnommen sind, auf jeden Fall unter Angabe der Quelle als Entlehnung kenntlich gemacht habe.

(Ort, Datum)

(Unterschrift Verfasser)

Acknowledgments

I wish to express my sincere appreciation and gratitude to my co-advisor, Dr. Gabriel Mistelbauer, for the excellent guidance all the way through this thesis. The countless hours we spent in discussions not only extended my knowledge but also sparked my interest for the field of medical visualizations. I am deeply indebted to my co-advisor Prof. Christian Nasel for supporting me not just with his medical and technical expertise but also with his valuable efforts that made the development of this thesis possible. My gratitude also goes to my advisor Meister Eduard Gröller for his support and much appreciated guidance.

Many thanks to the study participants Dr. Marko Faltin, Dr. Michael Konstantin, Dr. Elizabeth Stift and Dr. Florian Wollny for their contributions to this work.

My special thanks goes to my girlfriend Cornelia who encouraged me throughout the ups-and-downs of this thesis. Finally, I wish to thank my family for supporting me and especially my little sister Jenny who, one day will mention me in her thesis' acknowledgments too.

Abstract

This thesis presents a novel method for the visual quantification of cerebral arteries. The Circle of Willis (CoW) is an arterial structure that is responsible for the brain's blood supply. Dysfunctions of this arterial circle can lead to strokes. The diagnosis of stroke patients is complex and relies on the radiologist's expertise and the software tools used. These tools consist of very basic display methods of the volumetric data without support of state-of-the-art technologies in medical image processing and visualization. The goal of this thesis is to create an automated method for the standardized visualization of cerebral arteries in stroke patients in order to allow visual indications of problematic areas as well as straightforward inter-patient comparisons.

Prior to the visualization, this work offers a solution for the extraction of the CoW from Time-of-Flight Magnetic Resonance Angiography (TOF-MRA) images. An enumeration technique for the labeling of the segments is therefore suggested. Furthermore, it proposes a method for the detection of the CoW's main supplying arteries by analyzing the coronal, sagittal and transverse image planes of the volume. This work gives a comprehensive account of the entire pipeline that is required to extract the arteries in the CoW and to build a model for the standardized visualization. The final goal of this thesis is to create an effective display of the arteries based on a radial tree layout.

The feasibility of the visual quantification method is tested in a study of 63 TOF-MRAs. With the proposed methodology applied to the subjects, the results were compared to the findings from radiologists. The obtained results demonstrate that the proposed techniques are effective in detecting the arteries of the CoW. Finally, we focused our methods on the identification of the main arteries.

Kurzfassung

Die vorliegende Arbeit präsentiert eine neuartige Methode zur visuellen Quantifizierung zerebraler Arterien. Der Circle of Willis (CoW) - lat. Circulus arteriosus Willisii - ist eine arterielle Struktur, welche verantwortlich für die Blutversorgung im Gehirn ist. Dysfunktionen dieses arteriellen Kreises können zum Schlaganfall führen. Die Diagnose eines Schlaganfalls ist ein komplexer Vorgang und abhängig vom Expertenwissen des Radiologen sowie von den verwendeten Software-Instrumenten. Diese Instrumente bestehen aus einfachen Darstellungsmethoden volumetrischer Daten, ohne die Unterstützung von State-of-the-art Technologien aus der medizinischen Bildverarbeitung und -visualisierung heranzuziehen. Das Ziel der vorliegenden Diplomarbeit ist die Erarbeitung einer automatisierten Methode für die standardisierte Visualisierung zerebraler Arterien bei Schlaganfall-Patienten. Damit einhergehend sollen visuelle Indikatoren problematischer Bereiche eingeführt, sowie unkomplizierte Vergleiche zwischen verschiedenen Patienten ermöglicht werden.

Im Vorfeld der Visualisierung bietet die vorliegende Arbeit einen Lösungsvorschlag für die Extraktion des CoW aus Time-of-Flight Magnetresonanz-Angiographie-Bildern (TOF-MRA). Hierfür wird eine Enumerationsmethode zur Benennung der arteriellen Segmente vorgeschlagen. Des Weiteren wird eine Methode erarbeitet, welche die Detektion der Versorgungsarterien des CoW durch Analyse der koronalen, sagittalen und transversen Bildebenen übernimmt. Die vorliegende Arbeit bietet eine umfassende Darstellung des gesamten Vorgangs zur Extraktion der Arterien des CoW und zur standardisierten Visualisierung derselben. Das zentrale Ziel dieser Diplomarbeit ist es, eine effektive Darstellung der Arterien basierend auf einer radialen Baum-Struktur zu erarbeiten.

Die Genauigkeit der visuellen Quantifizierungsmethode wird in einer Studie mit 63 TOF-MRA Bildern erprobt. Die Erkenntnisse der Auswertung der Untersuchungsobjekte mit der vorgestellten Methode werden mit den Befunden von Radiologen verglichen. Die daraus resultierenden Ergebnisse demonstrieren die Effektivität der vorgestellten Techniken bei der Detektion der Arterien im CoW. Schlussendlich wurde der Fokus auf die Identifikation der Hauptarterien gelegt.

Contents

1	Introduction	1
1.1	Motivation	1
1.2	Medical Background	2
1.3	Data Acquisition	7
1.4	Objectives	8
2	Related Work	11
2.1	Region of Interest (ROI)	11
2.2	Segmentation	14
2.3	Histogram Analysis	18
2.4	Cluster Analysis	18
2.5	Vessel Modeling	20
2.6	Anatomical Labeling	22
2.7	Graph Conversion	23
2.8	Vessel Visualization	28
3	Methodology	29
3.1	Preprocessing of 3D TOF-MRAs	30
3.2	Vessel Extraction	35
3.3	Anatomical Labeling	57
3.4	Visualization	63
3.5	Implementation	69
3.6	Summary	72
4	Results	73
4.1	Evaluation	77
4.2	Application of the Proposed Methodology	95
4.3	Discussion and Limitation	98
5	Conclusion and Outlook	99
5.1	Conclusion	99
5.2	Future Work	100
	Bibliography	101

Introduction

1.1 Motivation

The human brain is a very delicate structure that is highly dependent on a well-functioning blood supply. A vascular disease in the brain can have tremendous consequences. One of the most critical implications is the stroke. It is the second most common cause of death and the major cause of acquired disability in the developed world [12, 45].

The diagnosis of a stroke requires imaging techniques, which are analyzed by radiologists. The focus is on an arterial structure, called the Circle of Willis (CoW). This structure guarantees the blood supply of the brain. Because of this vital function, many diseases of the brain are related to dysfunctions in this arterial circle. Hence, special attention is paid on the CoW during the diagnosis process.

After scanning the stroke patient, the radiologist inspects the volumetric data set (later simply referred to as volume) by using visualization methods. This permits a glimpse into the brain without surgically opening the head. The expert views the volume slice-by-slice in search of dysfunctions that cause the stroke. Visualization plays an important part during the diagnosis. A so-called Maximum Intensity Projection (MIP) of the data is also used to provide an overview and further insights. Apart from that, the process relies on the knowledge and experience of the radiologist.

Considering the urgent nature and time constraints of stroke treatment, computer-aided assistance can potentially save valuable time by automating certain parts of the diagnostic process. Features such as attention guiding and comparisons between different patients are only two of the possible benefits of computer support. After all, the goal is to offer the best treatment to the patient. Furthermore, the time-consuming investigation of the data sets hampers the comparison of various subjects. This work proposes methods and algorithms to provide visual assistance to radiologists.

Radiologists have to undergo education and training, learning to interpret the content of medical volumes. The interpretation of these volumes is complicated and requires knowledge about the complex anatomy of the cerebral blood flow. Whereas the radiologist sees anatomical

structures, such as vessels and organs, the computer views the data set as a grid with intensity values defined at each point in the volume. These so-called voxels are the atomic elements in the volume. They define the intensity values at each voxel in the grid. The problem with the voxel-based representation is that it requires an intermediate model to apply high-level knowledge. Although the radiologist has comprehensive expertise regarding the physiology of the CoW, it requires an extensive description of the CoW in the volume in order to apply his knowledge.

The first part of this thesis describes methods that allow the computer to extract the cerebral arteries from a grid of voxels. This consists of different image processing techniques. A critical step is to divide the voxels in the volume into vessel and background, which is called segmentation. Then the segmentation result is reduced to a skeleton and afterwards converted into a vascular tree model. This model represents the CoW and describes its features, such as the partition into the subtrees, the artery's path and length, its branching points etc. This process will be referred to as quantification of the CoW in this work.

The next part of this thesis describes a display method for the quantified model. We propose a visualization method that presents the extracted arteries and its branching structure by identifying the main arteries. The information has to be presented to the expert in such a way that he effectively apprehends the content of the volume. The aim of this work is to define a standardized display method that supports a swift overview of the CoW. Visualization is a powerful method to abstract otherwise complex data. The final result is a visualization of the quantified model that allows the viewer a far simpler apprehension of the CoW than traditional methods.

As a result, the proposed visualization can be used to indicate anomalies and guide the attention of the radiologist. It creates an easy complementary display of the CoW without the effort of manually investigating the volume. As a consequence, this has great time-saving potential when analyzing numerous data sets. Furthermore, a standardized representation of the CoW enables an efficient comparison. In this way, additional conclusions can be drawn by comparing the standardized visualizations of a vast number of patient's CoWs.

The data sets for this work were provided by the radiology department of the Universitätsklinikum Tulln [19]. They are 3D TOF-MRAs of patients with various brain diseases. The volumes are partially acquired with the application of a contrast-enhancing agent. The high resolution volumetric data sets are primarily analyzed in order to define a suitable visualization method. A pipeline for automated processing of the data sets is proposed in the following chapters.

1.2 Medical Background

The human brain has a high oxygen and nutrition demand and is, therefore, critically dependent on a well-functioning blood supply. A reduction in the blood supply can cause the loss of brain function as well as permanent damage to the affected area. An ongoing reduction can lead to a stroke, which is a medical emergency that can cause permanent neurological damage or even death.

Numerous diseases are related to dysfunctions of the CoW. In clinical practice, the stroke is regarded as highly urgent and requires swift actions. The causes of a stroke are mainly related to anomalies in the circulatory system. They are categorized into two classes: ischemic and hemor-

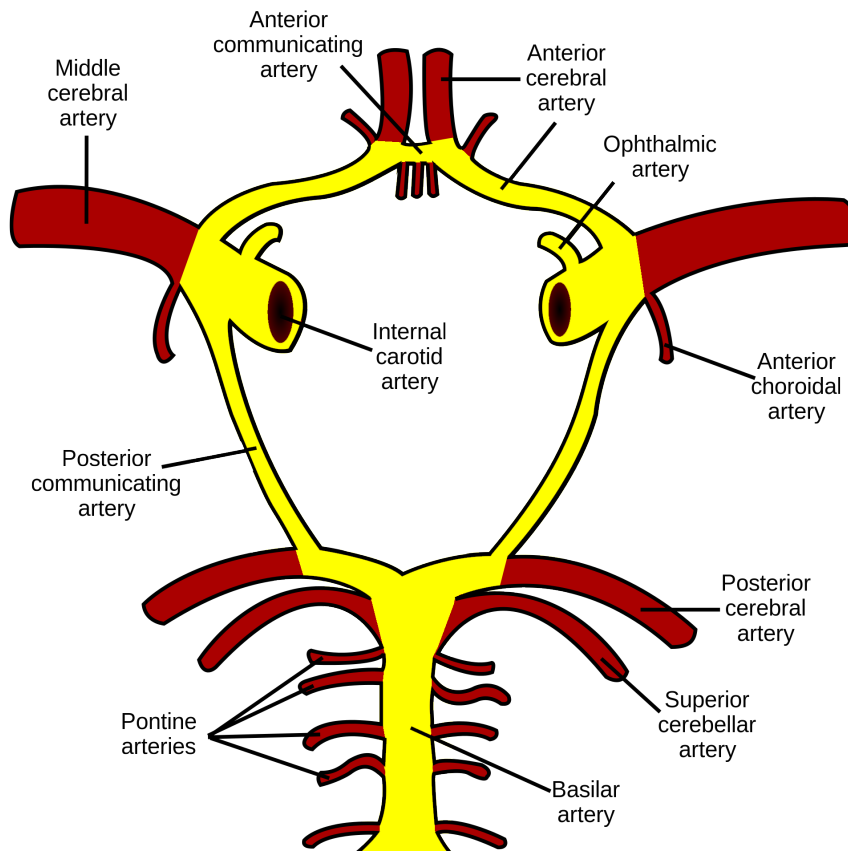


Figure 1.1: Schematic illustration of the arteries of the cerebral blood circulation. The yellow highlighted segments are considered to be part of the Circle of Willis. The two Internal Carotid Arteries supply the anterior part (subtree) of the brain, whereas the Basilar Artery supplies the posterior part. The Posterior Cerebral Artery arises from the Basilar Artery and connects with the Internal Carotid Artery through the Posterior Communicating Artery. Both of the Anterior Cerebral Arteries bifurcate from the Internal Carotid Arteries and are connected via the Anterior Communicating Artery. These arteries form the arterial circle of the brain, known as the Circle of Willis. Figure modified and taken from [34]

rhagic. The majority of strokes are ischemic, which are caused by a decrease or total interruption of the blood supply or by an abnormal vasculature. A hemorrhagic stroke, on the other hand, results from bleedings inside the brain. Analysis of the cerebral blood flow and the detection of ischemic and hemorrhagic strokes are done with the assistance of imaging techniques. The radiologist (the terms radiologist and domain expert are used interchangeably) is thereby focused on anomalies in the vasculature, where particular interest is paid to the patient's CoW.

Anatomy and Physiology of the Circle of Willis

The CoW is located in the base of the brain and is subdivided into three parts depending on the source of blood supply. Its posterior part is supplied through the Basilar Artery (BA). The left and right anterior parts are supplied through the two Internal Carotid Arteries (ICAs). We refer to these parts as subtrees. These three main arteries are then connected in an arterial circle, the Circle of Willis, as shown in Figure 1.1. As this figure shows, the left and right anterior subtrees are connected by the Anterior Communicating Artery whereas the anterior and posterior parts are connected by the respective Posterior Communicating Artery. Together, they form a circle (hence its name) to create a redundant blood supply.

This structure is named after the English neuroanatomist Thomas Willis, who was the first to offer a complete description of the shape, topology and the probable function of the arterial circle [46]. The textbook definition as seen in Figure 1.1 of the CoW is composed of the following arteries:

- Left and Right Internal Carotid Artery (ICA)
- Basilar Artery (BA)
- Left and Right Anterior Cerebral Artery (ACA)
- Anterior Communicating Artery (ACoA)
- Left and Right Posterior Cerebral Artery (PCA)
- Left and Right Posterior Communicating Artery (PCoA)
- Left and Right Middle Cerebral Arteries (MCA)

The three main arteries are the Left Internal Carotid Artery (LICA), the Right Internal Carotid Artery (RICA) and the BA, which are responsible for the blood supply of the circle. Arteries can be subdivided into segments, if they have side branches. The ACA is classified into five segments (A1 - A5), of which only the A1 segment is considered to be part of the circle. The PCA is subdivided into four segments (P1 - P4) and only the P1 segment is part of the circle. The MCA has four segments (M1 - M4) and is not regarded to be part of the CoW, but it can also be affected by occlusions. Therefore, the M1 segments are also considered in this work. For the sake of simplicity, we use CoW as an umbrella term that also contains the M1 segments even though they are not considered to be part of the CoW from a medical perspective.

The left and right ACA are connected by the ACoA, which also forms the junction between the two anterior parts. The posterior part of the CoW is connected via the left and right PCoA to the respective anterior part. Hence, the ACoA and the PCoA are referred to as the communicating arteries.

The delicate shape of the CoW is complex and exhibits considerable anatomical variability in topology and morphology. The standard textbook description of the CoW, as shown in Figure 1.1, only holds true in a rather small subset of patients. There are variants of this configuration where some arteries could be duplicated, underdeveloped or absent at all [22]. The underdevelopment is also referred to as hypoplasia. The shape of the CoW determines not only

its ability to adapt to anomalies in the cerebral vasculature, but also the appropriate treatment chosen by the radiologist. Due to the complex and strongly varying shape of the CoW, it is a common location for vascular pathologies and is therefore of particular interest.

Stroke

The root cause of a stroke is always the shortage of nutrition and oxygen in the brain cells. The separate regions of the brain fulfill different functions. A malfunction of the blood supply can be associated with particular symptoms. As a general rule, the larger the affected area the more functions are lost. The losses are reflected in the behavior of the patient. These symptoms are used to predict the presence of a stroke and its degree. Even though there are different scoring systems, a precise diagnosis relies on the assistance of imaging techniques. The cause and subtype of a stroke is determined via Computed Tomography (CT) and Magnetic Resonance Imaging (MRI). Chalela et al. [9] did a prospective comparison of non-contrast CT and MRI for emergency diagnosis of acute strokes and found that with MRI there was a more frequent detection than by CT. Strokes are roughly divided into two subtypes: ischemic and hemorrhagic. This distinction is a very important step in stroke management [12].

In the standard configuration, the circle is supplied through three main arteries: the RICA, LICA and the BA. They pose as anatomical landmarks and are easily identified by the radiologist since they are large and also appear to have the highest intensity values in the provided angiographies. Using these main arteries as reference allows the radiologist to identify the other arteries of the CoW and investigate the cause of a potential anomaly.

Hemorrhagic Stroke

A hemorrhagic stroke is caused by an abnormal accumulation of blood within the skull. The bleeding causes increased pressure in the skull, which damages the brain tissue. This usually appears suddenly and usually affects patients with hypertension.

According to the American Stroke Association [24] a hemorrhagic stroke results from a weakened vessel that ruptures and bleeds into the surrounding brain tissue. The damage is caused by the undersupply of the affected area and the room-occupying bleeding. The cause of a rupture is either an aneurysm or an arteriovenous malformation [24]. In addition, high blood pressure raises the risk of a spontaneous vessel rupture. The bleeding can be intracerebral (inside the brain) or subarachnoid (area around the central nervous system).

Ischemic Stroke

The majority of all strokes are ischemic. A sudden cerebral hypoperfusion (decreased blood flow) leads to an undersupply of the brain tissue. This condition is called ischemia. It is generally caused by problems related to the vasculature such as embolism, atherosclerosis or thrombosis. The underlying cause of an ischemic stroke is very likely related to dysfunctions of blood vessels within the brain or somewhere else in the body. The different causes of the dysfunctions are described in the following:

- **Embolism**

An embolism describes a clog in the blood stream. An embolic stroke is caused by an embolism. It occurs when a blood clot, that is formed somewhere in the body, travels to the brain arteries and lodges a narrow artery. As a result, the blood flow is reduced or totally blocked.

- **Thrombosis**

A thrombotic stroke occurs when the blood clot is formed within the cerebral arteries. The clot blocks the blood flow and causes the brain tissue to die quickly.

Transient Ischemic Attack

A transient ischemic attack is caused by a clot in a blood vessel. The blockage occurs rapidly and disappears within minutes since the clot dissolves after a while. Hence, it is often referred to as a *warning stroke*. Therefore, the difference between a stroke and a transient ischemic attack is that with the latter the blockage is only temporary [24].

Causes of a Stroke

- **Atherosclerosis**

Atherosclerosis describes the process in which the arterial wall is damaged as a result of an inflammation. Once damaged, deposits of fatty substances, cholesterol, cellular waste, calcium and other particles start to build up [24]. This buildup is called plaque. It usually affects large and medium-sized arteries [24]. As a result of this process, the diameter of the artery reduces and the blood flow decreases. The damage occurs when the plaque grows in size and eventually ruptures. This causes either the formation of a blood clot or the plaque travels to another part of the body. When it blocks smaller vessels in the brain, it will lead to an ischemic stroke. Depending on the location where the blood clot forms, it can be further categorized into thrombotic or embolic stroke.

- **Aneurysm**

Aneurysms refer to an enlargement of an artery. This is due to a disease in the arterial wall (e.g. atherosclerosis). The constant pressure of the blood flow causes the areas to enlarge and create a balloon-like shape. This usually appears in the brain arteries near branching points. The symptoms depend on the size of the aneurysm. Smaller aneurysms remain asymptomatic while the larger ones cause localized pain, difficulty with vision, numbness or weakness of an arm or leg, difficulty with memory or speech, or seizures according to the American Stroke Association [24]. If an aneurysm ruptures, it bleeds into the surrounding tissue and as a result the patient suffers from a hemorrhagic stroke.

- **Arteriovenous Malformation**

Arteriovenous malformation is a congenital disease where the arteries are directly connected with veins. As a result, the artery bypasses brain tissue and directly diverts into the veins, causing an undersupply of the affected brain tissue [24]. The abnormal connec-

tion between the high-pressure arteries and low-pressure veins causes the vein to dilate or burst.

1.3 Data Acquisition

Medical imaging techniques allow the creation of visual representations of a body's interior and are often applied for diagnostic purposes. They provide the necessary tools to detect diseases noninvasively. The acquired data are complex and must be interpreted by an expert. Visualization techniques play a central role in displaying the data to the expert. In clinical practice, a stroke is commonly diagnosed using Magnetic Resonance Angiography (MRA). Its high-quality volumes enable the radiologist to search for abnormalities in the intra- and extra-cranial blood vessels.

Angiography

Angiography describes an imaging technique that acquires an image to display vessels. There are non-invasive and invasive procedures where a catheter is inserted to administer a contrast agent to distinguish vessels from their surrounding tissue. It is a technique that enables the diagnosis of pathologies related to blood vessels.

Magnetic Resonance Imaging

The basic principle of Magnetic Resonance Imaging (MRI) is explained by Preim [37]. MRI exploits the behavior of the hydrogen nuclei under the influence of a strong magnetic field. The hydrogen nucleus consists of one proton and can be considered as a small dipole that aligns either parallel or anti-parallel in that field. A radio frequency (RF) pulse signal perpendicular to the magnetic field is emitted at a specific frequency (= Larmor frequency) that causes the hydrogen nuclei to perform a precession movement. They move into a high-energy state. That means the protons receive some energy from the RF and are forced to spin synchronously (in phase) until the number of parallel and antiparallel protons is equal [37].

When the RF pulse is dissipated, the protons move back to the alignment with the magnetic field and dephase. The emitted energy during the relaxation step is recorded and used to reconstruct the signal. To get the spatial information orthogonal magnetic gradients are applied. The resulting volume consists of intensity values that are based on the specific tissue properties. Most MRI machines operate between 0.3 and 3 Tesla with a resolution around 1 mm^3 [41].

Magnetic Resonance Angiography

MRA is based on MRI and is used to illustrate blood vessels by applying special parameter settings. In comparison to computed tomography angiography, the patient is not exposed to ionizing radiation. Depending on the technique a gadolinium-based agent is administered to improve contrast between a vessel and its surrounding tissue [40]. According to Scherthaner, MRA seems more favorable in general especially with patients suffering from impaired renal

function. However, on the other hand it is more cost-intensive compared to computed tomography [40].

Time-of-Flight MRA

3D TOF-MRA create detailed high-resolution volumes. In this method the magnetization of the inflowing blood is done outside the volume. The flowing blood takes a certain amount of time to reach the observed area and has higher magnetization than the saturated stationary tissue. The magnetization results in a much higher signal. A drawback of this technique is the poor visualization of areas with slow flow, such as large aneurysms. The problem is solved by injecting a contrast enhancing agent. However, this method is not always applicable since it may be dangerous for certain patients. According to the domain expert, the majority of scans is performed without using a contrast agent.

Neuroimaging Informatics Technology Initiative Data Format

For this thesis all data sets were provided in the Neuroimaging Informatics Technology Initiative (NIfTI) data format. NIfTI is widely used by neurological tools. It solves problems with previous neurological data formats. The lack of adequate information about the orientation was a problem, since a volume could not be unambiguously interpreted. Consequently, the left and right sides of the brain were usually confused. This led to the development of the NIfTI data format. Its goal is not only to solve the orientation problem but also to speed up the development of informatics tools related to neuroimaging by providing a data format and services [17].

1.4 Objectives

The goal of this thesis is to provide assistance to the radiologist by visually quantifying the CoW. The main challenges are to automate the steps in the diagnostic process and to provide simpler and more efficient insights into the medical volume of the CoW.

As discussed before, particular interest is paid to the blood supply of the brain through the CoW. Traditional methods such as slice view and MIP are used during the diagnosis to detect the cause of possible dysfunctions. They allow detailed investigations of the cerebral circulatory system. However, it may be unpractical when it comes to comparing different volumes. Considering the capabilities of today's computers, it stands to reason to provide assistance for the radiologist. Slice views and MIPs are well-suited for detailed investigations but are unnecessary, time-consuming processes when it comes to tasks beyond the detailed investigation for diagnostic purposes. The aim of this thesis is to create both an abstraction and a well-suited description of the CoW on the basis of patient-specific volumes provided for this work. Thereby, the focus lies on the automation of this process. The result is a high-level vascular tree model that represents the arterial system beyond voxel intensity values. Finally, a novel visualization method for the CoW is introduced describing the patient's CoW with its branching structure and affiliation to the respective subtrees.

The methods are developed in collaboration with our domain expert from the Universitätsklinikum Tulln [19], who is an expert neuro-radiologist. A key aspect of the visualization is to

show the topology of the cerebral arteries. As mentioned before, the identification of the supplying arteries plays a major role in diagnosis. There are various cases where one of the main arteries is duplicated, hypoplastic or missing at all [22]. The presence of the main arteries influences the configuration of the circle and determines the appropriate treatment methods. Hence, the effective display of the CoW's topology is particularly important. The final goal is the effective visualization of the CoW that displays the artery structure in a standardized manner. The quantification and every step prior to that are necessary to create the advanced visualizations and are described in the following.

Pipeline

For the visual quantification of the CoW, this work presents a software solution that implements the required methods. The detailed pipeline is shown in Figure 1.2. From a software engineering perspective it is necessary to investigate the requirements of the domain expert. The most critical requirement for the application is simplicity. In order to offer good assistance, it is a key aspect that the application does not introduce new working steps for the radiologist. The overall goal is to automate the processing pipeline and thereby reduce the user interactions to a minimum.

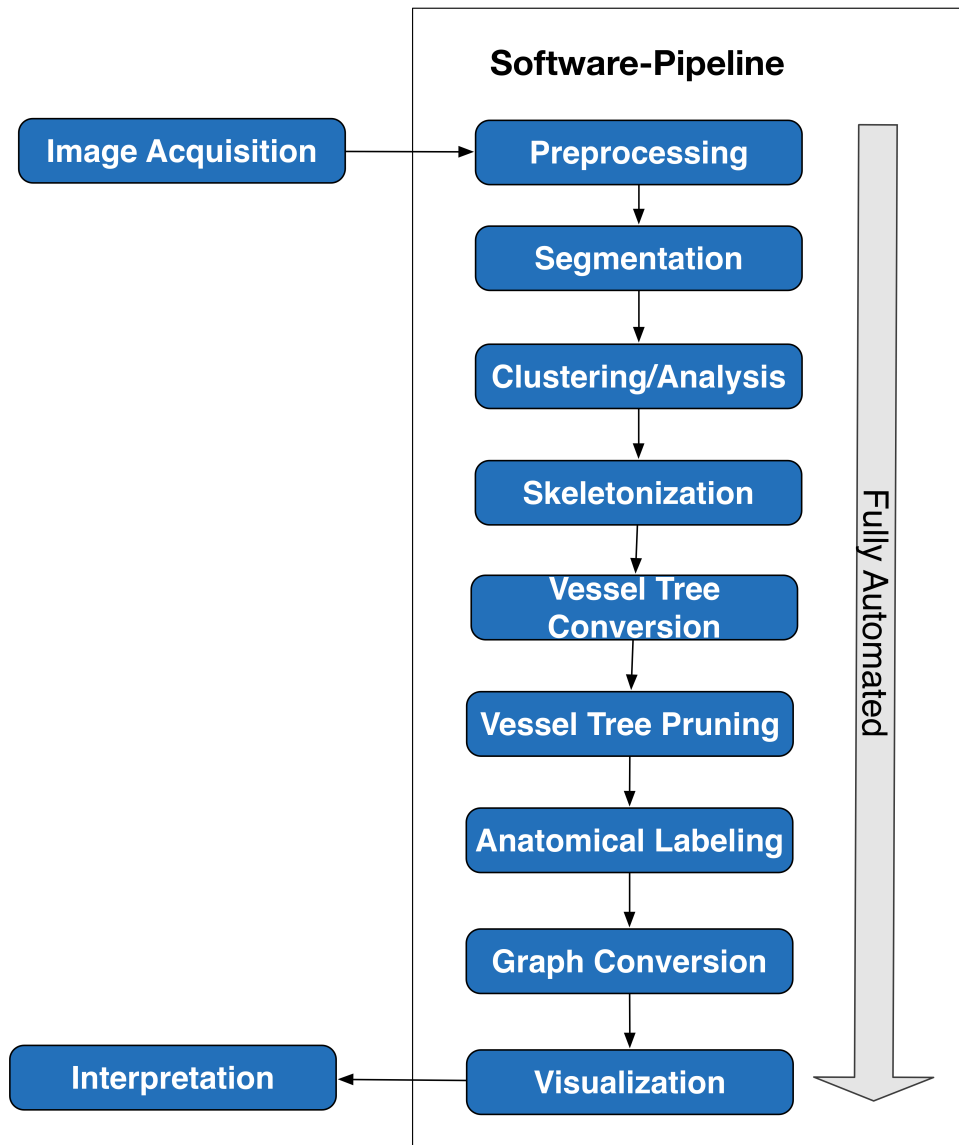


Figure 1.2: The figure shows the pipeline of the software solution that provides fully automated processing of a TOF-MRA. The first step is preprocessing where a rough location of the CoW is estimated. Next the CoW is segmented from the volume. The result is clustered into the three subtrees of the circle. Using skeletonization and conversion rules a vascular tree model is created on the basis of the segmented vasculature. This vascular tree model is then post-processed (pruned) in order to remove noise. In the labeling step additional information will be assigned to the vascular tree model. The labeled tree is then converted into a two-dimensional graph. In the last step, a radial vessel graph is created and presented to the radiologist.

Related Work

Imaging methods are an essential part in today's clinical practice. The non-invasiveness and accurateness of computer aided analysis of angiographies potentially benefits the radiologist and in the end the patient. The quantification of the CoW in particular has already gotten attention in recent years. Several publications have appeared that investigate various attributes of the arteries in the CoW to detect abnormalities, such as Bullitt et al. [6]. They quantify the vessel shapes by a set of geometrical attributes to draw conclusions between the attributes and pathologies.

To the best of our knowledge, the visual quantification of the CoW has not been attempted before. The most related methods and algorithms for the proposed pipeline, as shown in Figure 1.2, are described in this section.

2.1 Region of Interest (ROI)

The CoW only occupies a small spatial part of the volume. Thus, it is not required to analyze the entire volume but only a part of it. A ROI refers to a voxel subset of the volume. Defining a ROI is advantageous in many ways. It reduces the runtime of voxel-based algorithms since the scope is decreased by a major part. In addition, it simplifies further tasks such as segmentation by providing a rough estimation of location and size of the targeted structure. It is commonly defined by a geometric shape that fits the purpose. Proper ROI placement is a very important step in the processing of large volumes. It determines the effectiveness of subsequent algorithms. A common approach is to manually specify the ROI or use anatomical landmarks in the volume as an orientation for automated ROI placement. A general description of the ROI is given by Preim [37]. One of the latest labeling solutions of the CoW is presented by Bogunovic [4]. He defines a ROI in a reference volume and registers it with a test volume that adopts the ROI. Thereby, he uses a cuboidal ROI with a size of 256^3 voxels to reduce the computation time of his segmentation approach.

The shape of the ROI depends on the targeted structure. A cuboidal ROI might be unsuitable to cover a structure inside the human skull since a cuboid has corners, which could intersect

with the skull. A super-ellipsoidal shape is a more suitable choice, which is described in the next section.

Super-ellipsoid

Super-ellipsoids are three-dimensional geometric shapes whose horizontal and vertical sections are super-ellipses [42]. The implicit equation of the super-ellipsoid is given by:

$$\left(\left| \frac{x}{A} \right|^r + \left| \frac{y}{B} \right|^r \right)^{\frac{t}{r}} + \left| \frac{z}{C} \right|^t \leq 1 \quad (2.1)$$

x , y and z are coordinates in \mathbb{R}^3 . The size of the shape is defined by the diameters of the axes A , B , C . The exponents r and t are positive real numbers that control the amount of flattening at the tips and at the equator. r and t are the same exponents for the horizontal and vertical intersecting super-ellipses. However, this equation defines a wide range of different shapes. Only a subset of these shapes is of interest for this work. Setting $t = r$, the flattening at the tips and the equator will be equal, resulting in a more uniform shape that fits the CoW ideally:

$$n = t = r \quad (2.2)$$

The shape is set by the exponent n . Equation 2.1 can be written as follows:

$$\left| \frac{x}{A} \right|^n + \left| \frac{y}{B} \right|^n + \left| \frac{z}{C} \right|^n \leq 1 \quad (2.3)$$

The Equation 2.3 defines a set of geometric shapes that encases the arteries in the CoW. Some examples are shown in Figure 2.1. The placement of a super-ellipsoid in a volume as a ROI is shown in Figure 2.2. The CoW shows a high variability in shape and structure. Depending on how much of the arteries we want to cover with the ROI, the definition of a cuboidal ROI is not ideal, since its corners could include parts of the skull. In TOF-MRA volumes, the skull has a similar intensity range as the arteries, which is especially problematic for the subsequent segmentation step. The use of a super-ellipsoid assures that the arteries of the CoW are covered by the ROI but not other structures. The flexibility in shape and roundedness of the super-ellipsoid makes it a fitting ROI definition for covering the arteries in the CoW.

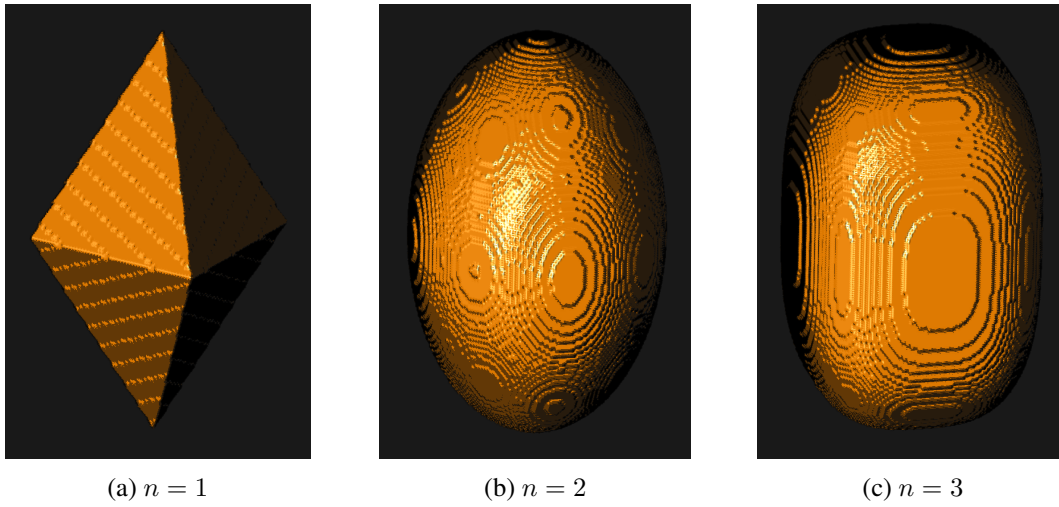


Figure 2.1: Examples of super-ellipsoids using Equation 2.3, with $A = 5$, $B = 5$ and $C = 6$. The figures display the changes in shape when the exponent n is increased.

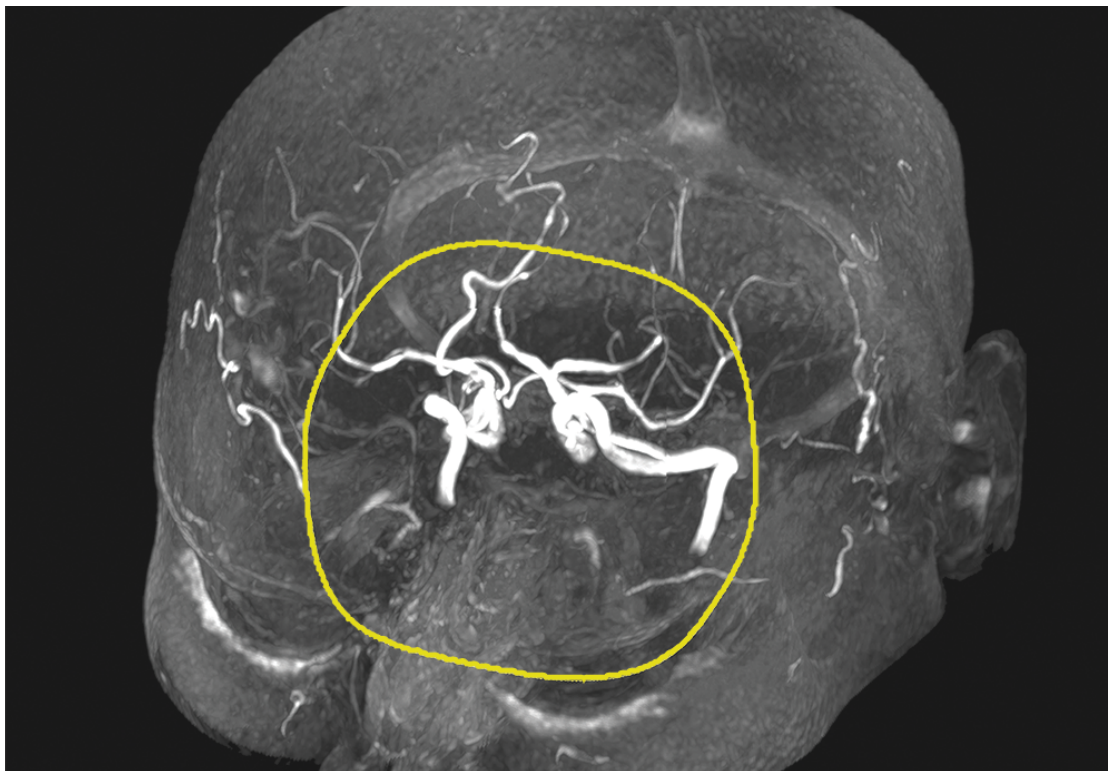


Figure 2.2: The yellow contour displays the super-ellipsoid with $n=3$. The shape covers the CoW entirely without enclosing the skull.

2.2 Segmentation

Advanced visualization techniques require the detection of anatomical structures. The segmentation of objects is one of the first and most important tasks in medical image processing. It forms the basis for advanced tasks. Therefore, segmentation results determine the success of the subsequent algorithms. However, it is not a trivial task, especially in the case of the CoW because of its high variability and the limitations given by TOF-MRAs. A typical problem is a low contrast between vessel and its background. Furthermore, structures that do not belong to the vessels but exhibit similar intensity values also cause problems [37].

Using a suitable technique is the key to get an adequate segmentation. Preim described basic and advanced techniques in the field of medical imaging in his book *Visual Computing for Medicine* [37], which provides fundamental information for the realization of our proposed pipeline. The segmentation of vessels is a widely studied field since many diseases are related to dysfunctions in the vasculature. Successful segmentation depends on the imaging modality and on the respective vasculature that needs to be extracted. Kirbas and Quek [26] compare different vessel extraction methods targeting at neurovascular structures. They distinguish six categories, which are described in the following:

- **Pattern recognition approaches**

These techniques deal with the automatic detection of vessel structures and features by using pattern recognition techniques [26]. There are various approaches to it but they commonly search for regularities in the images such as intensity values, curvatures and other features.

- **Model-based approaches**

Model-based strategies employ knowledge of the size and shape of objects [37]. Many approaches apply a model that fits the shape of the targeted vessel structure.

- **Tracking-based approaches**

These techniques apply local operators on a focus area known to be a vessel and track it [26]. They use the centerline or contour to track it from an initial point. Compared to other techniques, this approach might be unfavorable since the tracking requires a user-specified starting point.

- **Artificial intelligence-based approaches**

The segmentation process is guided by knowledge from different sources. These approaches exploit a priori knowledge of the targeted anatomical structure [26]. They employ low-level image processing algorithms such as thresholding but apply high-level knowledge [26]. The domain expert who forms a set of rules specifies the high-level knowledge.

- **Neural network-based approaches**

Artificial neural networks and machine learning methods have been popular for the segmentation task. The network consists of nodes that are called neurons. They are single processing units that receive input signals and an external parameter. The output depends

on the input and an additional activation function, which is similar to biological neurons. These neurons are connected in a network allowing complex computations for different tasks. Bishop [3] describes neural networks in detail. The main advantage of neural networks and machine learning approaches is their training phase. Prior knowledge is not specified by an expert but extracted from a training set. The segmentation is then considered a classification task where a voxel is either labeled as a vessel or as background.

- **Miscellaneous tube-like object detection approaches**

Algorithms dealing with the extraction of tubular structures fall into this category [26]. There are numerous tubular objects in the human body beyond vessels such as the airway tree. According to Kirbas and Quek [26] the difference to model-based approaches is that these techniques are designed to extract other tubular structures but may be applicable to vessels as well.

Aylward et al. [1] described an approach that makes use of the geometry of blood vessels. The intensity values are associated with elevations where the vessels form the ridges. These ridges are extracted as the medial axis of the vessels.

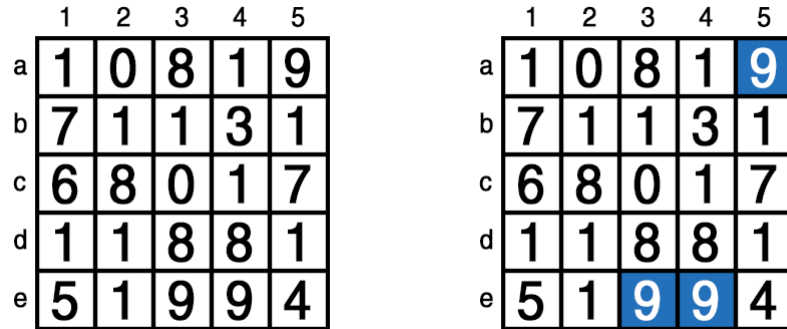
Pock described in his diploma thesis [36] an automated segmentation method using a level set technique for tubular structures. His work also includes a skeletonization and graph construction approach. A probabilistic atlas-based approach on peripheral computed tomography angiography was described by Straka [41].

Hysteresis Thresholding

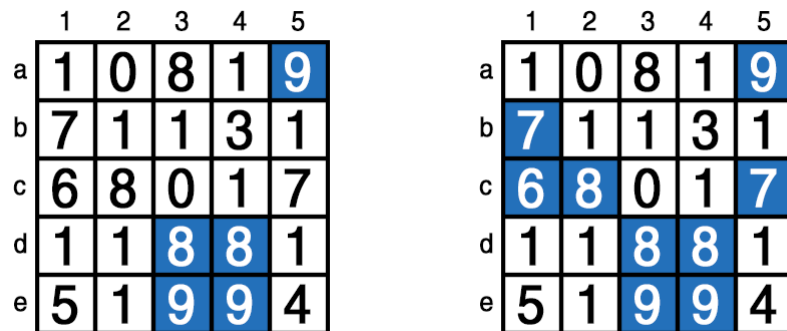
There are different automated or semi-automated segmentation approaches. A very common approach is the simple threshold-based segmentation. Since the intensity values are often associated with tissue types, it is practicable to detect structures by using a defined intensity range. Hysteresis thresholding (HT) proved to be very effective at this task. It was firstly described in Canny's edge detection algorithm [8]. HT employs a high and a low threshold, t_h and t_l . As Condurache and Aach [11] state, this method is motivated by the physiology of vessels. It is based on the assumption that vessel structures are connected. Therefore, it allows the algorithm to follow a path that is given by the blood flow. The high threshold t_h segments the artery voxels with high confidence. The low threshold t_l segments only those voxels that are connected to the high confidence areas.

The disadvantage of this approach is that suitable thresholds have to be specified first. They determine the final result. Consequently, it is normally the user's task to select the threshold either by observing the volume or using the trial-and-error method. However, this is a manual approach, that requires user interactions. The method for an automated computation of these thresholds is discussed in Section 2.3. The HT method is demonstrated in Figure 2.3.

The application of this procedure for the segmentation of vessels is described by Condurache and Aach [11]. They included a vessel enhancement step before an image is segmented and apply their approach on different angiographic images and reported good results. The central disadvantage of this approach is that the effectiveness of the segmentation result depends on the chosen two thresholds. In the provided medical volumes for this thesis, the intensity range of the



(a) A matrix to be segmented by HT with $t_l = 5$ and $t_h = 8$. (b) The high confidence areas, consisting of elements with values above t_h , are shown in blue.



(c) Elements connected to the high confidence areas are added if they have values above t_l . (d) The final result of hysteresis thresholding.

Figure 2.3: This figure depicts an example of the HT algorithm using a low threshold $t_l = 5$ and a high threshold $t_h = 8$. (a) shows the initial matrix. The values represent intensity values of a two-dimensional image. (b) shows the result after the first step where the values above t_h are segmented (shown in blue). They form the high confidence areas. The algorithm then searches in the eight-neighborhood for values above t_l . The result is shown in (c). This step is repeated recursively and (d) shows the final result. The cell a3 may be greater than t_l , but it is not adjacent to a high confidence region; therefore, it is not included in the final segmentation.

arteries in the TOF-MRAs varies since the intensity values are influenced by the conditions during the acquisition. As a result, using the same absolute threshold for all volumes is inadequate. In Section 2.3 an automated approach for the selection of the thresholds based on histogram analysis is described.

Region Growing

Region growing defines a group of growth-based segmentation methods. The approach is based on the idea that the voxels in an anatomical object share similar properties. The difference to HT is the application of different similarity constraints that can be used to adjust the growth behavior. The adjacent voxels are examined and added to the initial region according to the similarity constraints. A basic approach can be described as follows:

- The first step is to specify a seed point or a set of seed points.
- The region grows by adding connected voxels that fulfill the similarity constraints.
- The growth stops when there are no similar and adjacent voxels left to add to the region.

The proper choice of seed points is essential. They must be representatives of the target structure since they determine the similarity and eventually the growth process. A common approach is to use the segmentation result of a different method to leave out the manual seed point selection. Prem [37] concluded that the standard approach is not ideal for tracing vessels because of partial volume effects where two different tissue types are represented by the same voxel.

Salah [39] discussed more advanced region growing approaches. He summarizes different similarity criteria that improve the growth behavior. His statistical-based criterion is of interest since it alters the similarity constraint according to the added voxels on the basis of a statistical analysis. This behavior is especially desirable as the arteries in the MRAs vary constantly in their intensity ranges. A common method is to compute the mean intensity value of the region and only add voxels that are in a close distance to the mean [39]. The mean is regularly updated, which enables the growth to adjust accordingly. However, the drawback is that the growth behavior can be either under- or over-adjusted. The key is to find the ideal balance between desired adjustment and over-adjustment. Another limitation of this approach is the computational expense required to check the similarity between a new element and the elements in the region. In general, arteries in the provided MRAs have heterogeneous shapes and vary greatly in intensity values. A similarity criterion effective for the entire region is inadequate since vessels change their intensity values. A growth criterion might work well for larger vessels but not for smaller ones. Conversely, the criterion for thin vessels is inadequate for larger arteries, since they usually have much higher intensity values. Local growth criteria face this issue. For instance, the growth criterion could adapt to the surroundings of an artery.

2.3 Histogram Analysis

The histogram represents the distribution of intensity values in a medical volume. It is represented by vertical bars and a horizontal axis of values [37]. Each vertical bar represents the frequency of intensity values in the volume. The analysis of the histogram is often employed to derive appropriate parameters for subsequent operations. The peaks in a histogram are most likely related to tissue types. In the volume, only a tiny fraction of voxels is taken by arteries. Consequently, the intensity values of arteries are not represented by a local peak in the histogram. This hampers the search for the intensity values of arteries. However, the intensity range of arteries can still be found by estimating its proportional stake in the volume. This can be achieved by specifying a percentile in the histogram. The intensity range of arteries in MRAs stretches to the upper end of the histogram since the vasculature is represented by the highest intensity values.

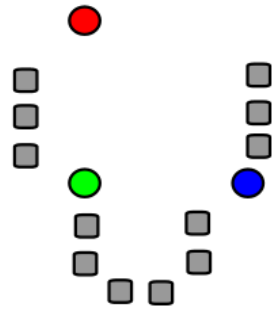
The work by Condurache and Aach [11] describes a method for the fast computation of appropriate thresholds that is related to this work. In order to compute the two parameters for the hysteresis thresholding algorithm used in this thesis, they derive the threshold based on the assumption that vessels occupy a certain part of the volume. They refer to the high threshold as the hard one and the low threshold as the weak one. Condurache and Aach analyze the histogram and consider the area that is clearly covered by vessels and select the high threshold on the basis of this area. The low threshold is then based on the area that is clearly covered by the background. Although this is a very simple approach it employs prior knowledge about the intensity range of the vessels and the background to compute the thresholds quickly. The result yields good estimations for the parameters of the threshold-based segmentation algorithm in this work.

2.4 Cluster Analysis

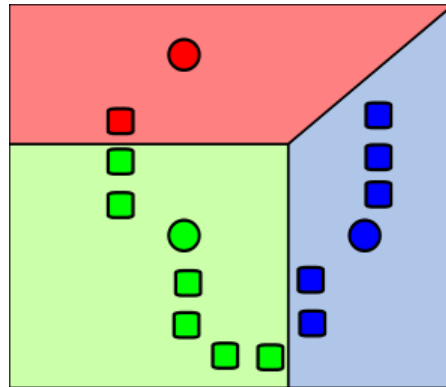
The idea of clustering is to group elements with similar properties together. There are many approaches to clustering. In this work, solely *hard clustering* algorithms are of interest. Compared to other methods, hard-clustering methods assign the elements to a single cluster. The application of clustering in the analysis of the CoW is described by Bullitt et al. [7]. Her approach is based on the subdivision of the intracranial circulation into four vessel clusters. Another method is proposed by Hernandez and Frangi [23]. They apply k-means clustering for the automatic segmentation of aneurysms in Three-Dimensional Rotational Angiography (3DRA) and CTA data sets. They showed good performance in the segmentation of vessels.

K-means

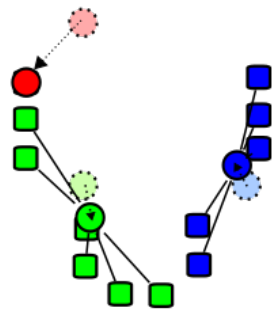
K-means clustering is a very efficient but simple way to group elements into a fixed number of clusters. It was first introduced by Lloyd [30]. The algorithm repeatedly finds the centroid of each cluster and re-partitions the elements according to the closest centroid. The algorithm converges when re-partitions no longer change the position of the centroid. Figure 2.4 demonstrates the k-means algorithm with an example.



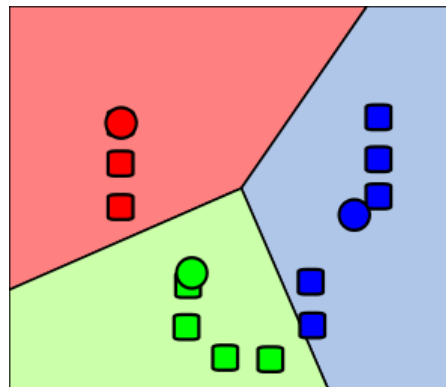
(a) Each colored circle represents a different cluster centroid (mean). The initial means are selected randomly. The gray squares are observations that will be clustered.



(b) The observations are then assigned to their closest mean. The partition generates the Voronoi diagram [25]. Using the closest mean assignment, the decision boundaries are linear.



(c) The mean of each cluster is calculated and becomes the new centroid.



(d) The observations are then reassigned according to the new mean.

Figure 2.4: Demonstration of the k-means algorithm in the two-dimensional space with $k=3$. The steps (b), (c) and (d) are repeated until the assignments do not change anymore. (Images taken from [25].)

A disadvantage of this approach is the dependence of the clustering results on the initial centroids. The method easily converges into a local optimum. In addition, the k-means approach only performs well for clusters that have a spherical distribution. These clusters can be separated with linear borders but vessels are elongated structures and, therefore, require curved decision boundaries. Supervised learning approaches such as a Support Vector Machine (SVM) would provide better results. A SVM is trained on a set of pre-classified data sets. On the basis of that training, it predicts the class membership for new observations. By using radial basis functions, a SVM separates clusters by non-linear decision boundaries.

2.5 Vessel Modeling

The result of the segmentation process is often used for visualization purposes. However, the method described above still leaves the vasculature represented in voxel space. Therefore, the segmentation forms the basis for the construction of a vascular model. In the case of anatomical tree structures such as vessels, the medial axis is commonly extracted. The medial axis of a tubular structure is often referred to as the centerline or the skeleton. The skeleton is an intermediate result that is used to extract the branching structure of the vasculature [37]. Usually, the vessels are then represented as a branching graph where high-level operations can be applied to. This way, the vasculature is no longer represented by a set of voxels in a coordinate system but rather by nodes and edges as a vascular tree.

Skeletonization

The skeleton is defined as a one-voxel wide line representation in the center of volumetric objects [37]. There are different algorithms that compute the skeleton. The majority is based on erosion to segment an object until one voxel in the center remains. These skeletonization methods are called thinning [37]. An approach is presented by Lee et al. [29] that uses a 3D parallel thinning algorithm to extract the medial axis of a 3D object. The points in a three-dimensional space are sequentially deleted in decreasing distance order until a one-voxel-wide centerline remains. A key aspect of skeletonization is to preserve the topology. The boundary points are only deleted if they can be removed without changing the topology of the object. These points are referred to as *simple* points. The authors ensure the topological invariant by using the *Euler characteristic* of the object [29].

The concept of *simple* points is widely used in skeletonization algorithms. Pock [36] summarizes *simple* points as follows. Points are *simple* and can be removed if their removal does not

- create a hole,
- create a cavity,
- disconnect connected components.

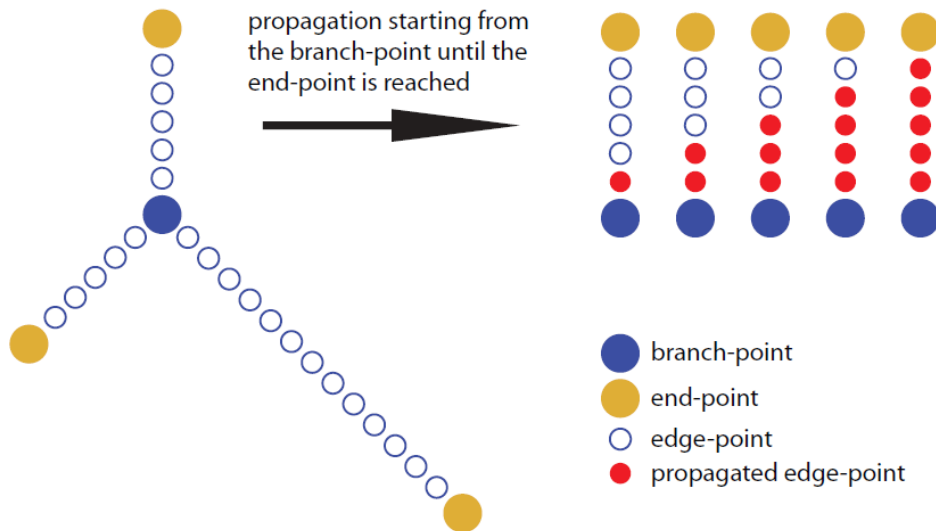


Figure 2.5: Illustration of the conversion from the skeleton to a graph as described by Mistelbauer [32]. The edges are created by propagating from the branching points along the edge points. (Image taken from [32].)

Vessel Tree Conversion

In the last step, the resulting skeleton has to be converted into a three-dimensional graph. In the literature this graph representation is frequently referred to as the *vessel tree* since the vasculature has a tree-like structure [33]. With the skeleton being one voxel wide at each point, the conversion can be done by applying the following rules:

1. $n_{26} = 1 \Rightarrow$ end-point
2. $n_{26} = 2 \Rightarrow$ edge-point
3. $n_{26} \geq 3 \Rightarrow$ branching-point

n_{26} describes the number of skeleton voxels in the 26-neighborhood. These rules are described by Pock [36]. A detailed conversion algorithm is introduced by Mistelbauer [32]. First the nodes of the graph are created on the basis of the first and the third of the above specified rules. Due to the properties of the skeletonization method it is possible to convert the voxels either to an end-point, an edge-point or a branching-point by applying the rules described above. Then the edges of the graph are created by applying the second rule. The edges are built by propagating from the end-points and branching points. Figure 2.5 illustrates the conversion from the skeleton to the vessel tree model defined by Mistelbauer [33].

According to Mistelbauer [33] a vasculature is usually represented as a tree, which consists of roots with various branches but does not contain any loops [33]. However, the cerebral artery structure is normally connected in a circle; hence, the name is *Circle of Willis*. For the sake of

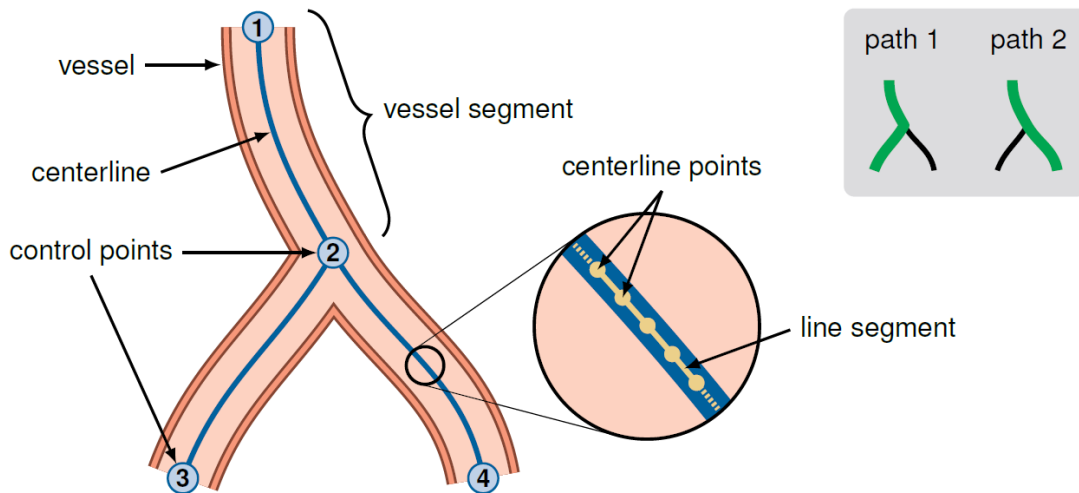


Figure 2.6: Illustration of the vessel tree by Mistelbauer [33]. The vasculature is well represented by this vessel tree model (Figure taken from [33]).

simplicity, this vasculature model of the CoW will also be referred to as vessel tree even though it can contain a cycle. The vessel tree suggested by Mistelbauer is described in the following. The tree consists of edges, representing *segments* and nodes, representing *control points*. Branching points and end-points are converted to *control points*. The segments are usually not linear but rather curved where points specify their route. These points are referred to as *centerline points* and the linear connections are called *line segments*. An illustration is shown in Figure 2.6. A *vessel path* defines a series of segments. The only adaption to this vessel tree model is that cycles have to be allowed in the graph.

A different 3D vascular tree for the description of cerebral arteries is presented by Bullitt et al. [5]. They describe a tree-creation process where a minimum-spanning tree algorithm is employed to evaluate intensity values at the connection points. Their semi-automatic program provides tools to edit the tree. A disadvantage of their approach is the requirement of user-supplied seed points for each vessel.

2.6 Anatomical Labeling

A very recent automated approach for anatomically labeling parts of the CoW using a statistical inference method is proposed by Bilgel et al. [2]. The focus of their method is on the anterior subtree of the CoW using a random forest classifier trained on centerline features. The labeling task is then framed as a statistical inference problem on the Bayesian network representation of the vessels. They tested their approach on 30 subjects and showed an accuracy of over 92%. However, their approach is restricted to the anterior part, but leaves out the posterior part.

Another work that investigates the geometry of the CoW was introduced by Bogunovic [4]. His work is motivated by the search for *geometric risk factors* that cause diseases in the cerebral

vasculature. His approach starts with the automated segmentation of 3DRA and MRAs using a geometric deformable model within the level set framework, which he refers to as *Geodesic Active Regions*. He proceeds with an automated characterization of the CoW using the features on the example of the ICA. In the last part of his thesis, he describes an automated labeling approach of the cerebral arteries. His method models the CoW as a rooted attributed relational graph, which describes the local geometric features of bifurcations as well as their topological relationship. The latter is described by a set of eight reference graphs. Before labeling, the method has to be trained on pre-labeled data. The labeling of a new test vasculature is based on a maximum a posteriori probability estimation where the local features of bifurcations define the likelihood term and the prior term is defined by the reference graphs. The result is a labeled graph description of the CoW. He showed less accuracy than Bilgel et al. but his approach is not restricted on a part of the arterial circle.

Tang and Chung [44] proposed a tree-matching algorithm for 3DRAs based on the concept of theoretical tree edit distance. Even though the approach seems very promising, they only verified their methods on synthetic data; thus, there are no results on the performance on real data.

Bullitt et al. [6] described the automated detection of abnormalities by focusing on the tortuosity metrics. A similar approach was used by Piccinelli et al. [35] where the authors use curvature, torsion and tortuosity of the centerlines to characterize the internal carotid artery. Both works apply a similar approach and the authors showed good results in detecting vessels and abnormalities by abstracting the vasculature to a small set of geometrical parameters.

Hartkamp and Van der Grond [22] have done investigations into morphological variations of the CoW on the basis of MRAs. There are many variants of the typical configuration that is illustrated in medical textbooks. Certain segments can be hypoplastic, absent or duplicated [22]. A classification system based on the circular configuration of the CoW was introduced. The authors presented 20 variations of the CoW and investigated the changes in morphology in relation to the severity of the obstruction in the ICA.

Machine learning approaches for the characterization of vasculature have been proposed by Langs and Donner [13–15, 27]. Charnoz et al. [10] introduced a tree-matching algorithm for the hepatic vascular system.

2.7 Graph Conversion

Graphs have been popular in the field of information visualization. It is a commonly used method for the simple display of the relationships between various objects. The representation of the CoW as a graph is motivated by the illustrations in anatomical textbooks. The previously described methods create a three-dimensional vessel tree that serves as an abstraction of the CoW. However, the display of a three-dimensional structure on a two-dimensional surface is limited since the vessel tree can only be viewed from a certain angle. A partial tree can be hidden behind the vessels closer to the viewer. In order to get an entire view on the vessel tree it is necessary to interact with it. This circumstance suggests that a special depiction of the vessel tree is required that allows the radiologist to get a simple and effective overview without the need for interactions. The illustration of the CoW in Figure 1.1 motivates an unfolded display of the arteries

so that the complete CoW can be shown on a flat surface without hiding arteries. In order to do so, the labeled vessel tree has to be converted to a formal graph. The benefit of the graph lies in its simplicity and expressiveness. The definition of a graph is $G = (V, E)$. V is a set of nodes and E defines a set of edges between the nodes. A tree is an undirected graph, where two nodes in the tree are connected by exactly one edge. If a node is designated as the root, the graph becomes a rooted tree, in which case it has a direction that is oriented away from the root. The connected nodes are commonly referred to as the children.

A rooted tree is typically depicted in diagrammatic form, where the nodes are represented by ellipses that are connected by lines for the edges. An example of a rooted tree is shown in Figure 2.7. In this example the node 1 is the root of the tree as indicated by the doubled contour. However, the formal definition of a graph does not specify how it should be displayed to the viewer. For that purpose there are graph description languages, which provide a set of instructions to formally define a graph and its appearance. A well-known example is the DOT description language, which is described in the next section.

DOT Graph Description Language

DOT is a simple graph description language that both humans and computer programs are able to use [28]. It is widely applied and there are numerous applications that can process DOT files. The code in Listing 2.1 shows a simple example of a rooted tree with eight nodes and seven edges. Arrows are used to show the directed edges. The resulting graph is shown in Figure 2.7.

Listing 2.1: A rooted tree with eight nodes and seven edges described by the DOT description language. The node 1 is set as the root node.

```
digraph examplegraph
{
  1 [peripheries=2];
  1 -> 2 -> 4;
  2 -> 5;
  2 -> 6;
  1 -> 3;
  3 -> 7;
  3 -> 8;
}
```

Graph Visualization

As described in the previous sections, the tree pattern of the vasculature in the human brain is particularly suited to be depicted as a rooted tree, which is a subtype of a graph. Creating a graph representation means the transition from a text-based description of a graph to a visual representation. The method is called *graph drawing* or *graph visualization*. It combines graph theory and information visualization to create two-dimensional depictions of graphs.

DOT is a commonly used description language for graphs, which can be processed by the GraphViz software package [21]. It reads DOT files and uses different layout programs (dot,

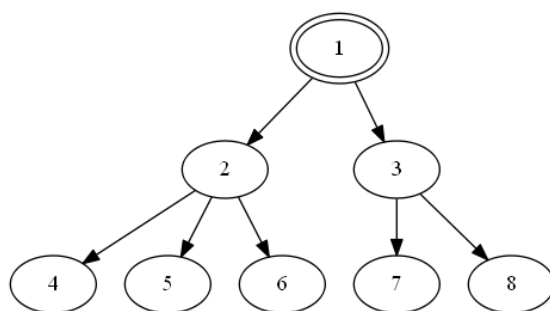


Figure 2.7: The figure displays a rooted tree that is specified using the DOT language. The code is shown in Listing 2.1. The graph is rendered by using the GraphViz package [21].

neato, fdp, twopi) to render it in diagrammatic form. Thereby the goal of the programs is to arrange the nodes and edges in a layout so that they represent the underlying data ideally and consequently provide a comprehensible visualization. General goals of a layout are to

- minimize the total area of the layout,
- minimize the crossing edges,
- group together similar nodes.

Gansner and North [20] describe the design of the GraphViz framework in detail. The *Handbook of Graph Drawing and Visualization* by Tamassia [43] provides a broad survey of current graph drawing algorithms and visualizations as well as the geometric foundations.

Radial visualizations are used to display data in a circular layout. Draper et al. [16] did a study of this visualization strategy. They describe radial design methods as visualizations that arrange data in an elliptical fashion [16]. The authors did a historical review of radial visualizations and identified seven types of radial design patterns, each having different applications: *Tree, Star, Concentric, Spiral, Euler, Connected and Disconnected Pattern*.

The tree in Figure 2.7 is visualized in a radial tree layout in Figure 2.8. With the root node in the center, the child nodes are drawn on the levels of the radial layout. The hierarchy is retained by the increasing levels. Draper et al. [16] refers to this as a concentric pattern since the root is at the centroid. This however requires a single rooted tree. By comparison, Figure 2.9 contains a second tree. Since there are two roots, the radial tree can not be concentric. The space is therefore divided into two sectors, each tree having its own spatial spread.

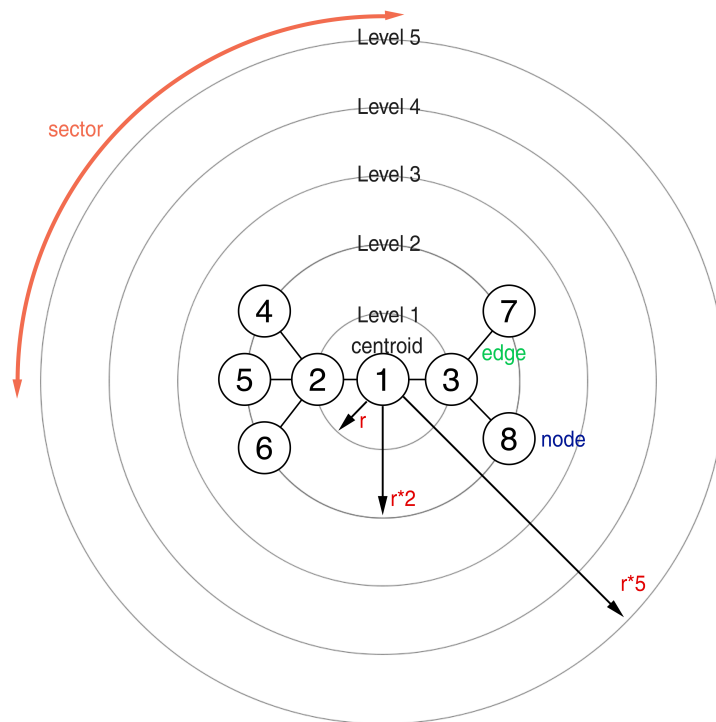


Figure 2.8: The tree of Figure 2.7 is drawn as a radial graph. Node 1 is the root of the tree; hence, it is drawn in the centroid. The levels correspond to the distance between the node and the root. The sector of a node is specified in degrees.

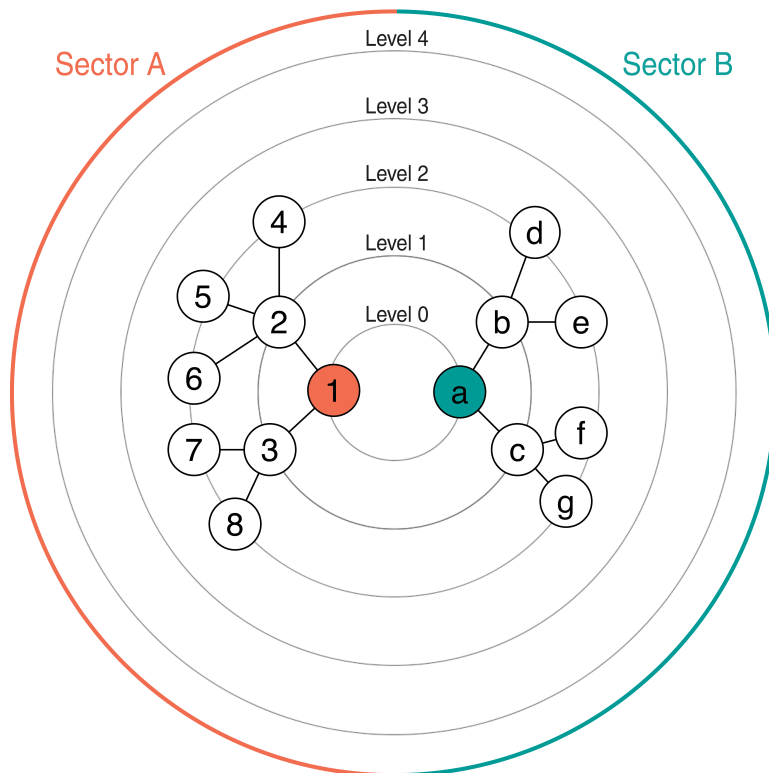


Figure 2.9: A non-concentric radial tree with two trees is shown. The root nodes are not positioned in the center but on the first level. The layout is divided into two sectors so that each tree has its own space.

2.8 Vessel Visualization

Visualization is an important aspect of this work since the results have to be comprehensibly presented to the radiologist. Even though the goal is to create a fully automated pipeline, it is still desirable to provide adjustment options for certain steps. For this purpose, basic visualization techniques such as slice views and MIP are also implemented in this work. Basic visualization techniques are described by Preim [37].

An effective display of the CoW guarantees an accurate interpretation. Conventional visualization techniques of anatomic structures such as direct volume rendering and iso-surface rendering are well suited to create an overview of the volume, however they are not appropriate for the diagnosis of stenosis or aneurysms. A detailed diagnosis relies on the slice-by-slice view of the volume. This work is focused on creating an overview of the intricate features of the cerebral artery without requiring user interactions.

Adequate segmentation and centerline extraction are prerequisites for advanced visualization techniques for vascular structures, which are described in the Sections 2.2 and 2.5. MIP is a simple but widely used technique for vessel visualization. With this technique a two-dimensional image is generated from the volume by tracing rays along the viewing direction. For each pixel in the resulting image the maximum intensity value along the ray is chosen. Blood vessels normally exhibit high intensity values and are therefore well depicted by this method.

Mistelbauer [32] proposes an improved version of the Centerline Reformation technique, which provide arbitrary viewing angles for the investigation of the interior of blood vessels. This depiction of the blood vessels is especially useful to diagnose patients with atherosclerosis.

A recent approach to visualization is the consideration of the uncertainty of medical data. During the processing pipeline, a certain amount of uncertainty is always introduced at each step because of errors, inaccuracies and assumptions. This information is typically omitted in visualizations and only one result is shown even though there might be other possible solutions. Uncertainty visualization can benefit the domain expert by providing decision support. Ritovski et al. [38] discussed various approaches of uncertainty in medical visualizations and their limitations. Lundström et al. [31] proposed probabilistic animation methods to convey uncertainty in volume renderings. Using probabilistic transfer functions, the authors developed an application for efficient stenosis assessment.

Methodology

The underlying data for a standardized visualization of the CoW has to be extracted from the medical volume. Several steps have to be implemented in order to build the underlying data for the visualization. The pipeline consists of methods known from the field of image processing and computer vision. The first step is to define a ROI that specifies the scope of subsequent algorithms. In the next step, labels are assigned to every voxel in the volume, indicating its membership to the CoW. This task is called segmentation and the quality of its results determines the performance of further steps. After that, a clustering method is applied that exploits the appearance of the segmentation result in the three axis-aligned image planes. Further on, a skeletonization method is applied to get the centerlines of the arteries. These centerlines are a good representation of the arteries' tubular structure. The centerlines are converted into the representation of nodes and edges in the three-dimensional space (this 3D graph is subsequently called vessel tree). A high-level labeling algorithm is applied to the vessel tree to identify the segments of the vasculature. The aim is to extract a high-level description from a voxel-based representation of the CoW. Finally, we propose a novel method to visually quantify the CoW in order to create a simplified display of it. The result is a standardized radial vessel graph that describes the CoW on the basis of a radial tree layout. The methods described in this chapter processes 3D TOF-MRAs that have been provided by the Universitätsklinikum Tulln [19]. We demonstrate the methods on the same example volumes throughout this chapter. Figure 3.1 shows an example CoW and its orientation inside the volume.

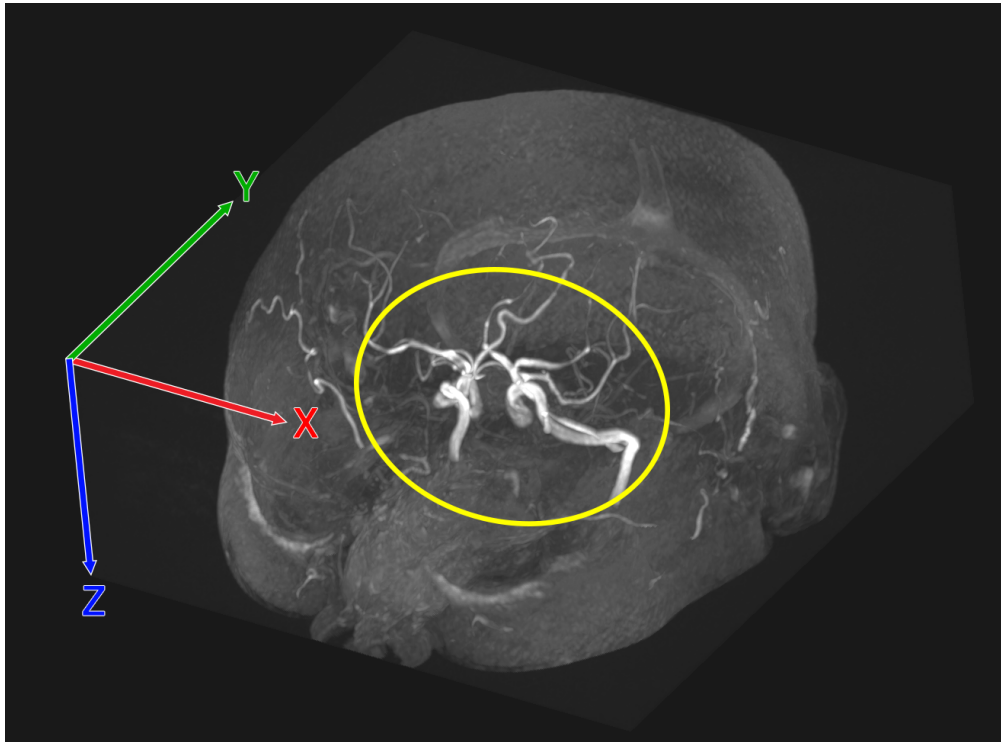


Figure 3.1: The figure shows the volume orientation in a coordinate system with three axes. The location of the CoW is indicated by the ellipse.

3.1 Preprocessing of 3D TOF-MRAs

In the preprocessing step, the volume is prepared for the subsequent methods. This step is carried out to estimate the location of the CoW. In the literature, this approximate location is often referred to as the ROI. We propose a simple method for the definition of a ROI around the CoW by using the skull as a reference.

Skull Detection by Ray Casting

The first step in the proposed pipeline is to segment the skull. It can be detected easier than the CoW itself by using a ray casting method. On the basis of the skull voxels, the location of the CoW can be estimated. Furthermore, the intensity ranges of bone structures and the arteries in TOF-MRAs can potentially overlap, depending on the conditions during the acquisition. Figure 3.2 demonstrates this circumstance. The intensity range of bones in the example volume is approximately (80, 250) and the arteries have a range of about (200, 782). For example, using a threshold value of 230 segments the artery voxels but also some bone voxels as demonstrated in the figure.

The intensity range overlap is problematic during the segmentation phase. Hence, the skull needs to be excluded from further algorithms. This method relies on two prior assumptions

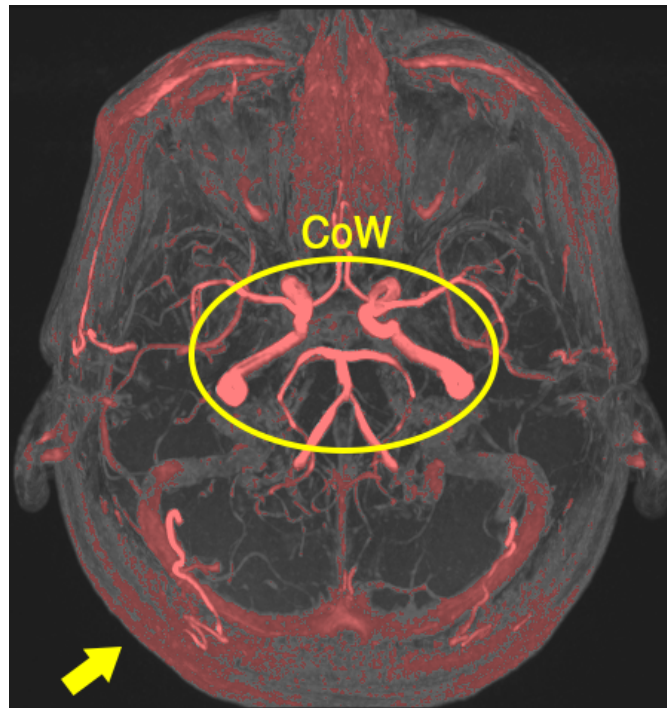


Figure 3.2: The figure displays the transverse MIP of the example volume where the voxels with intensity values above the threshold value of 230 are marked in red. The CoW, as indicated by the ellipse, is segmented by this threshold value. However, there are bone voxels that also have intensity values above this threshold (indicated by the arrow).

about the scan:

1. The brain is surrounded by the skull.
2. The skull appears within the scan.

However, the human skull has holes in the eye sockets and the base of the skull that allow rays to pass through. Furthermore, the head is normally clipped at the top, bottom, back and front part of the skull because only the approximate area around the CoW is usually scanned as it is shown in Figure 3.4 (a). Therefore, it only makes sense to shoot rays along the x-axis. The bones are hereby detected by using a threshold of 150, which is an empirically motivated value. Figure 3.3 demonstrates the principle of this approach with two example rays.

This approach is implemented as an algorithm, where rays are shot laterally into the volume along the positive and negative x-direction. Each time a ray hits two consecutive voxels with intensity values above the bone threshold the ray stops. The idea is that two consecutive voxels with higher intensity values are considered to be an indicator for an intensity peak, which is likely caused by the skull. For both directions, the rays will hit the skull first before reaching the brain and its arteries. When all rays are casted, the detected intensity peaks give a rough

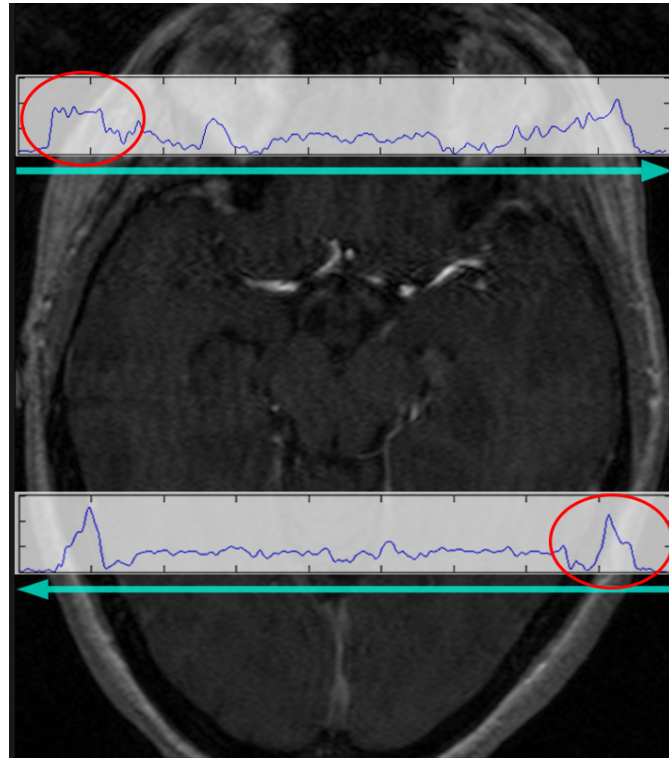


Figure 3.3: The figure demonstrates the skull detection method. Two lateral rays are sent from both directions indicated by the blue arrows. The intensity values are shown in the plot above. The method searches for the first intensity peak along the rays. The red ellipses mark the first intensity peaks that are detected by this method. It clearly shows that the first peaks are at the location of the bone.

estimation of the skull voxel's location. The result of this method applied to the example volume is shown in Figure 3.4.

Automated ROI Definition

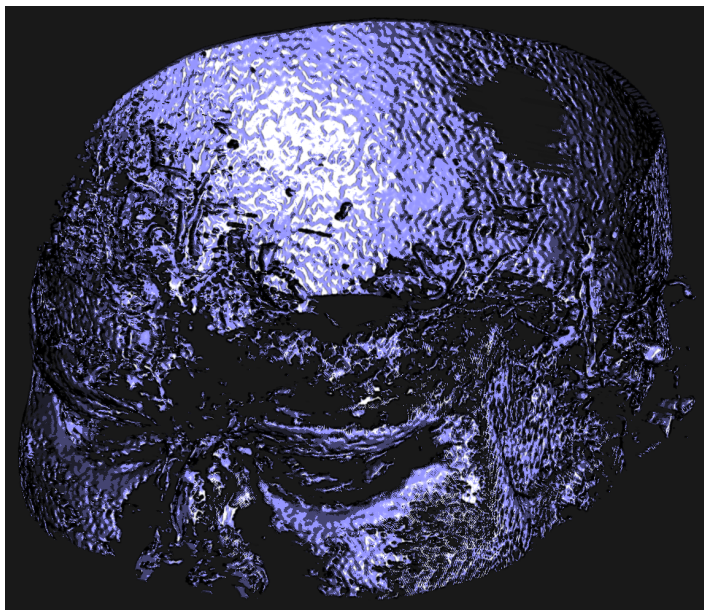
The definition of a ROI inside the volume plays an important role in extracting the arteries, because it gives an approximation of the CoW's location. This estimation provides valuable information for subsequent methods. In addition, it reduces the computational time of the algorithms since it cuts out a major part of the volume.

In this work, we suggest a super-ellipsoidal ROI to cover the CoW including a safe distance. The position and shape of the ROI heavily influences the subsequent steps. The advantage of a super-ellipsoid is its flexibility compared to a sphere, cuboid, ellipsoid. By adjusting the exponent n and the parameters A , B and C , the high variability of the CoW can be covered.

The manual placement of the ROI would introduce user interactions. Hence, we suggest an automatic approach that takes advantage of the previous skull detection step is proposed.



(a) The MIP.



(b) The result of the skull detection approach.

Figure 3.4: (a) displays the MIP of the example volume. (b) displays the result of the proposed method for the detection of the skull. It is marked in blue.

The center position (c_x, c_y, c_z) of the skull voxels is computed as the mean of the skull voxels' positions. However, the CoW is not centered in the skull. In order for the ROI to adequately cover the CoW, it has to be calculated from the skull voxels's center position (c_x, c_y, c_z) . The center coordinate of the ROI (p_x, p_y, p_z) is shifted from (c_x, c_y, c_z) by using the following empirically motivated equations:

$$p_x = c_x * 1.02 \quad (3.1)$$

$$p_y = c_y * 0.78 \quad (3.2)$$

$$p_z = c_z * 1.2 \quad (3.3)$$

These equations guarantee the placement of the ROI in close proximity to all arteries in the CoW. Next, the shape of ROI has to be set. The goal is to cover the CoW but not the surrounding tissue. This is done by setting the axes A , B and C of the suggested super-ellipsoid. For this purpose, the average Euclidean distance r between (c_x, c_y, c_z) and the skull voxels' positions are computed. r is thereby regarded as an approximated radius of the skull. The values for the axes A , B and C in the super-ellipsoid Equation 2.1 are then adjusted from the following empirically motivated equations:

$$A = r * 0.52 \quad (3.4)$$

$$B = r * 0.46 \quad (3.5)$$

$$C = Z * 0.52 \quad (3.6)$$

Z defines the volume size in the z-axis. Since the scan is clipped, the C-parameter of the super-ellipsoid is adjusted by using Z . For automated computation, the exponent n is fixed with $n = 3$, which is also empirically motivated. Of course, the adjustment of these parameters may be done manually by the user. However, it is normally not necessary since the provided volumes usually showed little variation in the CoW's location relative to the skull. Finally, the super-ellipsoid is placed in the volume and the voxels outside the ROI are marked as background and excluded from subsequent algorithms. Figure 2.2 shows the defined ROI using our proposed method.

The use of a super-ellipsoid instead of a cuboid, sphere or ellipsoid comes with higher computational costs. After the ROI is placed in the volume, each voxel's location relative to the super-ellipsoid has to be calculated using the Equation 2.3. Compared to the above mentioned shapes, this is more complex and hence more time-consuming. However, the ROI is placed only once at the beginning of the proposed pipeline and performance measurements showed that the computation of the voxel's location in a $512 \times 512 \times 156$ volume takes in average 1.28s on a CPU with 3.4 GHz. Performance details are shown in Section 3.5. Considering this relative short computational time and the given benefits of a super-ellipsoids' flexibility, the use of this shape is feasible. Future work could include the automated computation of the exponent n on the basis of the CoW's shape.

A limitation of this approach is the dependence on the ratio between the spread of the arteries in the CoW and the volume size. Different ratios could cause the ROI to exclude part of the CoW. For example, scans of children are affected by this limitation. Another drawback is that the current implementation is based on a rough estimation of the skull. For future work, the approximation of the skull using an ellipse-fitting method could increase the precision of our ROI placement approach.

3.2 Vessel Extraction

The volume has to be separated into regions where a subset is declared as part of the CoW and the rest as background. Next, the centerline is calculated on the basis of the segmentation. A centerline is an abstraction since vessels have a tubular shape. Based on this representation, a vessel tree model is created to get a high-level representation of the vasculature. This vessel tree model is then used for further analysis such as labeling and visualization, as described in the next section.

Segmentation

Segmentation is the task of identifying particular anatomical structures in the volume, which are relevant for a specific purpose. This step is the basis for visualization and image processing techniques. In medical imaging, segmentation is normally required to selectively show certain objects or to suppress distracting structures [37]. Technically, a label (or mask) is assigned to each voxel in the volume representing the membership to a particular structure [37]. There are different challenges to this task. First, a segmentation algorithm has to terminate in adequate time when it comes to time-critical scenarios. On the other hand, an inaccurate segmentation with too much noise is useless for further analysis. In the literature there are various segmentation algorithms that have benefits as well as drawbacks. In general, there are no superior segmentation methods but rather more or less suitable methods for a specific use case. Using hysteresis thresholding showed good performance in detecting the arteries of the CoW and still terminates in adequate time. This approach has two assumptions on the data sets that can be fulfilled by the provided TOF-MRAs:

1. The intensity value of a voxel is related to its probability of belonging to a vessel.
2. The structure has to be connected.

The first assumption is fulfilled after the application of the skull detection method described in Section 3.1. Whereas the second assumption is easily fulfilled due to the physiology of the vasculature and their representation in TOF-MRAs. The application of the HT approach is therefore motivated due to its simplicity and suitability. The high intensity areas most likely belong to the main arteries, which are detected by the high threshold (t_h). Vessels are connected tubular structures that typically bifurcate from bigger to smaller vessels. The blood flow normally guarantees that this connectivity is represented by high intensity values in the MRA. The connected arteries in the CoW are then detected by the low threshold (t_l). But there are problematic

areas in TOF-MRAs where thin arteries with minor blood flow appear with low intensity values. Especially the low intensity values of the communicating arteries cause difficulties during the segmentation.

A practical advantage of the HT segmentation is its straightforward implementation. It does not rely on a predefined model or trained data. The application on the provided data sets created good segmentation results of the CoW. However, the approach can not segment arteries that are not clearly represented by higher intensity values than the background. The detection of the small communicating or hypoplastic arteries depends on t_l . This threshold is the similarity criterion that is applied on a global scope. Due to the variation in the intensity values of the arteries, the adaption of the segmentation approach to these local intensity values could be beneficial. This way, the communicating and hypoplastic arteries could be detected more successfully.

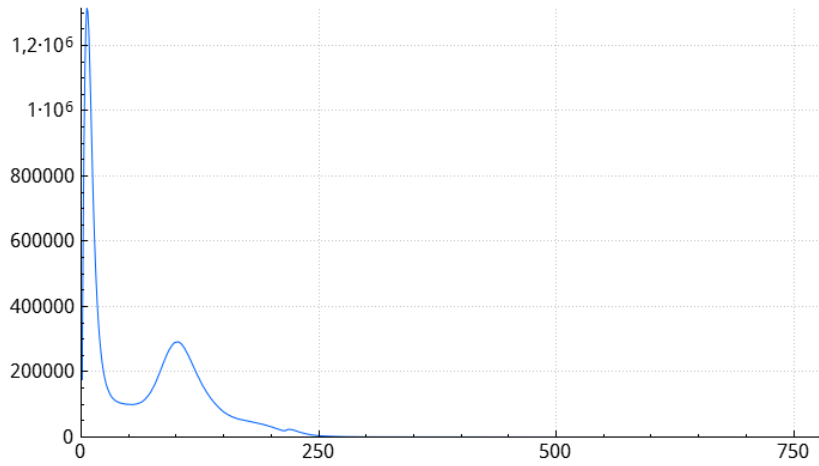
Threshold Estimation

This work suggests a histogram-based estimation of the HT thresholds that is related to the work of Condurache and Aach [11]. The distribution of the intensity values provides valuable information about the relationship between intensity value and tissue type. The distribution is known as the histogram. It can either be computed from the whole volume or from the voxels in the ROI. The histogram of the whole volume is shown in Figure 3.5a. However, this also includes the skull, which might distort the estimation due to the possible intensity range overlap. The other method solely includes the voxels inside the above-proposed ROI as shown in Figure 3.5b where the skull is excluded. This estimates more accurate ranges for the arteries. As shown in the figures in 3.5, the high intensity voxels only represent a relatively small part in the histogram, which means that the vessels make up a relatively small part of space compared to their surroundings. Therefore, the threshold can not be derived from a local maximum in the histogram. However, the proportional stake of the arteries in the defined ROI is similar in the provided volumes. In addition, the arteries are usually represented by the highest intensity values, since the scanning parameters are set to obtain the highest contrast for the arteries. Values around $t_l = 98.9\%$ and $t_h = 99.9\%$ have shown to create adequate results with the provided data sets.

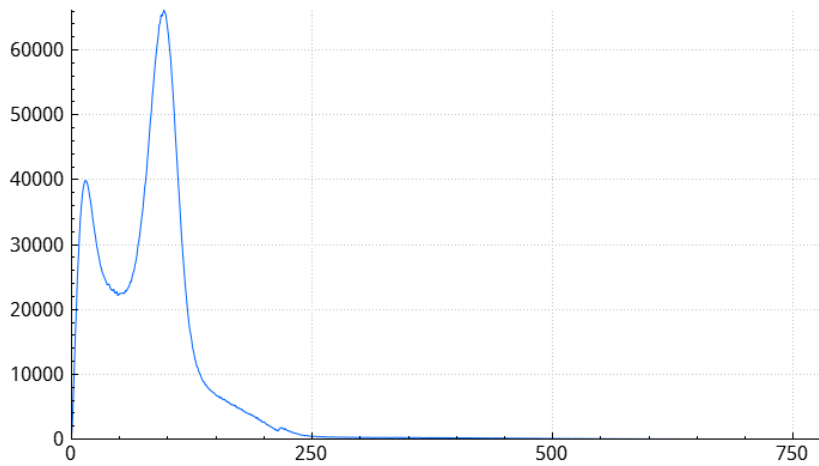
Vessel Detection

The figures in 3.6 illustrate the segmentation approach on our accompanying example. Thereby, a heatmap is used to emphasize intensity differences. In the MIP, the high intensity areas are clearly visible in red. They are segmented first and act as the high confidence areas. The connected areas in green are then segmented in the second step. The algorithm stops if there is no adjacent voxel with an intensity value above t_l left. The CoW is segmented in a breadth-first manner, meaning the region grows equally everywhere.

Using the high intensity voxels as high confidence areas has two benefits. First, it assures that a connected voxel will belong to the vasculature since there is an intensity difference between arteries and surrounding tissue. Second, it guarantees that only the arteries are reached by the algorithm, discarding the veins as long as they do not overlap with the arteries. The resulting segmentation is shown in Figure 3.6. The values are mapped to a heatmap, in order to



(a) Entire volume



(b) ROI

Figure 3.5: The histograms of the example volume are shown. The intensity range is $(0, 782)$. In histogram (a) every voxel in the volume is considered. Here, the global maximum is close to zero, which is caused by the background. In histogram (b), only the voxels in the ROI are considered. The global maximum is at around 100 representing soft tissue. The arteries are in an intensity range of about $(200, 782)$.

emphasize the intensity difference. The mapping is shown in Figure 3.7. It displays the high confidence areas in red and the segmented arteries in green. Starting from the high intensity areas and growing along the connected voxels make it possible to compute a distance field. At each segmented voxel, the Euclidean distance to the closest high confidence area is also encoded in the color. Whereas the main arteries are red, the peripheral arteries appear blue since they are far away from the high intensity areas.

This segmentation approach is limited by the large signal variations of TOF-MRAs. The intensity values are distorted by turbulent or slow blood flow. Figure 3.8 demonstrates this by an example. It displays very low intensity values in the LICA and RICA. This causes the segmentation algorithm to discontinue at these areas. Another limitation is the performance of the method in small, low intensity arteries. This affects the communicating arteries in particular (ACoA, PCoAs) since they normally carry lower intensity values than the larger ones. Decreasing the intensity threshold would detect them but causes the algorithm to leak at different locations, since the small arteries carry about the same intensity value as the surrounding soft tissue.

Clustering

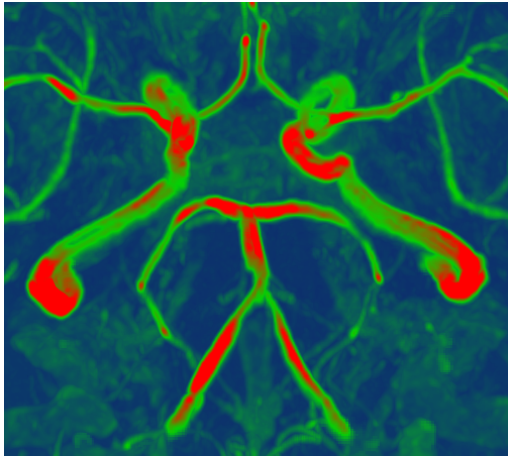
For this work, two approaches for the clustering of the CoW were developed. In the first approach, the previously segmented high intensity areas are separated into three clusters using the k-means algorithm. This algorithm groups the high intensity voxels using their spatial information. As discussed in Section 2.4, the resulting groups of the k-means algorithm are reliant on the initial centroids. This approach is based on the assumption that the high intensity areas are evenly spread in the three main arteries, LICA, RICA and BA. However, empirical observations show that the BA is weaker in its intensity values than LICA and RICA. The spatial alignment of the three clusters is then geometrically analyzed. In the case of missing arteries, the distribution of the high intensity areas in the volume is different from the normally configured CoW. Geometrical methods are used to detect missing main arteries. This approach was tested in a study of ten subjects. Although it could detect a missing main artery, it turned out to be too sensible. The method frequently raised false alarms in those subjects where all three main arteries are present. As a result, the false negative rate was too high.

The separation of the CoW into subtrees is an important aspect, especially in the detection of missing arteries. Therefore, a different approach was developed for the clustering of the CoW based on the analysis of the two-dimensional image planes.

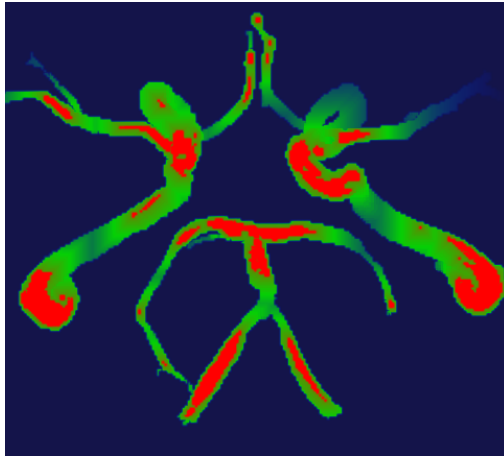
Image Plane Based Clustering

In the second approach, the entire segmentation result is separated into three clusters by employing knowledge about the spatial location of the voxels in a two-dimensional plane. Each cluster covers a subtree of the CoW, which is supplied through the respective main artery. This approach is based on the physiological partition of the cerebral blood circulation into these three parts:

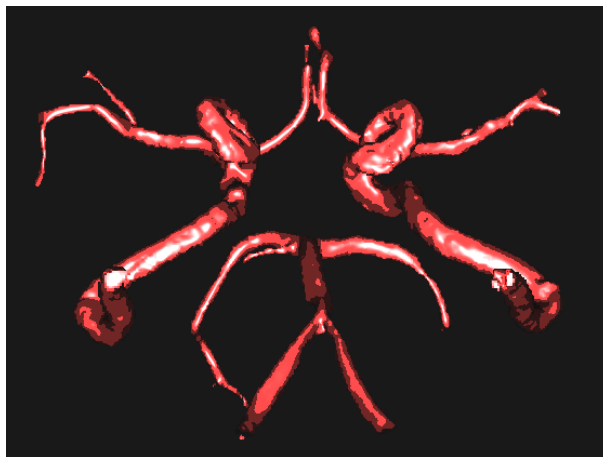
- The left anterior subtree is primarily supplied through the LICA.



(a) The MIP is projected to a heatmap in order to emphasize the intensity differences.



(b) The distance field of the segmentation result.



(c) The final segmentation result visualized with an illustrative rendering method.

Figure 3.6: The segmentation approach is demonstrated on the example volume. In (a) the high intensity areas are marked in red, which are segmented first. The connected areas with lower intensity values are shown in different shades of green. These areas are segmented in the second step. Figure (b) shows the distance field of the segmented result. The arteries of the CoW are shown in red and green. There are no veins or soft tissue segmented. Figure (c) displays the final segmentation in an illustrative manner. It clearly shows that the posterior subtree is not connected with the anterior subtrees.

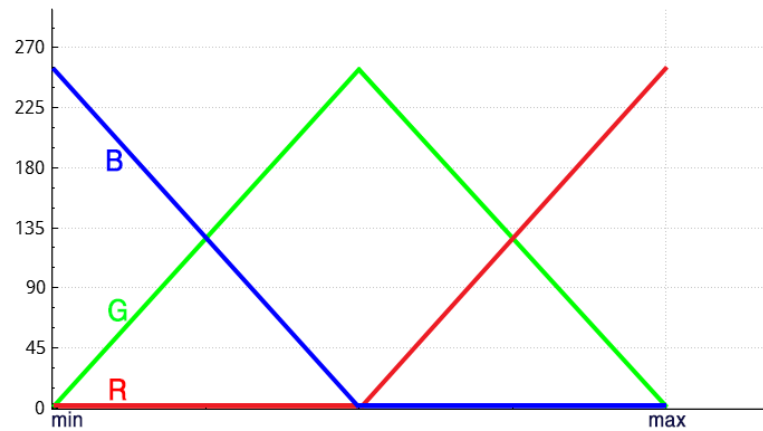
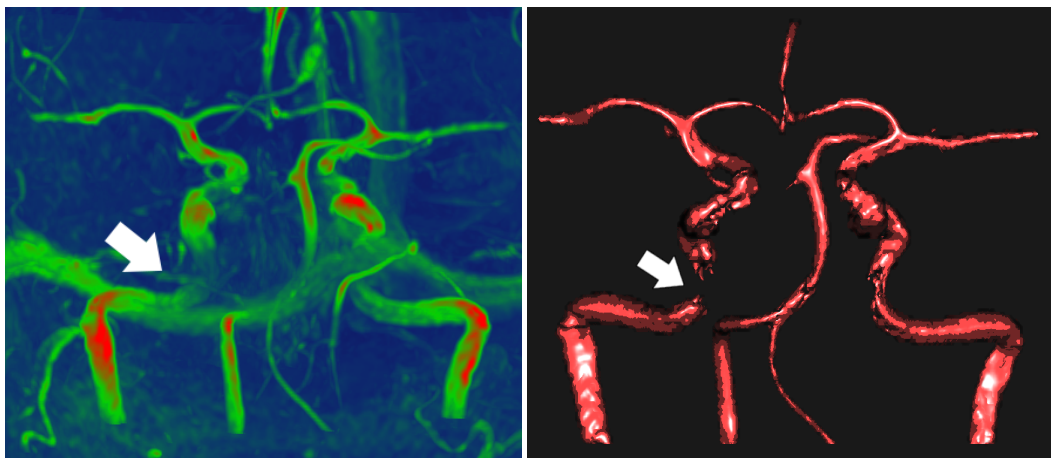


Figure 3.7: The figure shows the mapping of intensity values to a heatmap, where the maximal value is assigned to red (R), the minimal value to blue (B) and the values in between to green (G). This RGB value ranges from (0, 0, 0) to (255, 255, 255) and is used to emphasize the intensity difference.



(a) The MIP. The arrow points to the low intensity area.

(b) The segmentation result. The low intensity area causes a disconnection in the artery.

Figure 3.8: The figure displays the abrupt loss of signal in a different example volume. The proposed method is not able to segment these areas due to low intensity values. The volume is displayed in the coronal view for a better visibility of the problematic area.

- The right anterior subtree is primarily supplied through the RICA.
- The posterior subtree is primarily supplied through the BA.

The CoW's separation is demonstrated on a scheme shown in Figure 3.9. In this approach, prior knowledge about the location of the three subtrees in the provided MRAs is utilized. The posterior subtree is thereby extracted differently than the two anterior subtrees. The main idea is to reduce the segmented CoW into three two-dimensional binary planes, where the segmented arteries are set to one, representing the foreground, and the background is set to zero. These planes are flat projections of the CoW as shown in Figure 3.10. In the next step, the points are separated into three parts, each representing a subtree. The Figures in 3.10 display the two-dimensional projections of the volume along the y-axis (coronal plane), the z-axis (transverse plane) and the x-axis (sagittal plane). The computations of the three planes are shown in the Algorithms 1, 3 and 2. Then, the voxels in the volumes are marked accordingly by using these separate planes.

The reduction into a two-dimensional image enables a fast and straightforward separation of the arterial subtrees. The CoW in the volume is not directly separated into clusters, but instead the two-dimensional image planes are used to calculate the cluster affiliations of the voxels. Each plane offers a different angle on the volume and can be used to cluster a certain part of the CoW. Furthermore, the analysis of a two-dimensional image is less complex than a volume.

Algorithm 1 The computation of the coronal plane.

Input: The segmented *volume* with size $v_x \times v_y \times v_z$

Output: The *coronal* plane with size $v_x \times v_z$

Initialize *coronal* plane with 0

Initialize *coronal* plane with unknown mask

```

for  $x \leftarrow 0$  to  $v_x$  do
  for  $z \leftarrow 0$  to  $v_z$  do
    for  $y \leftarrow 0$  to  $v_y$  do
      if  $volume.mask(x, y, z) == vessel$  then
         $coronal.at(x, z) \leftarrow 1$ 
        break
      end if
    end for
  end for
end for

```

The separation of the points in a plane is done by using reference points. These reference points are based on the shape and location of the super-ellipsoidal ROI. All points in the binary plane are assigned to their closest reference point and are therefore separated.

In the coronal plane two reference points are defined, the left anterior reference point is at the location $(p_x + A, p_z + C)$ and the right anterior reference point is at $(p_x - A, p_z + C)$. They are shown in Figure 3.11 (a). First, each point on the coronal plane is assigned to the closest reference point and marked accordingly. The details are shown in Algorithm 4. However, as the

Algorithm 2 The computation of the sagittal plane.

Input: The segmented *volume* with size $v_x \times v_y \times v_z$

Output: The *sagittal* plane with size $v_y \times v_z$

Initialize *sagittal* plane with 0

Initialize *sagittal* plane with unknown mask

```
for  $y \leftarrow 0$  to  $v_y$  do
  for  $z \leftarrow 0$  to  $v_z$  do
    for  $x \leftarrow 0$  to  $v_x$  do
      if  $volume.mask(x, y, z) == vessel$  then
         $sagittal.at(y, z) \leftarrow 1$ 
        break
      end if
    end for
  end for
end for
```

Algorithm 3 The computation of the transverse plane.

Input: The segmented *volume* with size $v_x \times v_y \times v_z$

Output: The *transverse* plane with size $v_x \times v_y$

Initialize *transverse* plane with 0

Initialize *transverse* plane with unknown mask

```
for  $x \leftarrow 0$  to  $v_x$  do
  for  $y \leftarrow 0$  to  $v_y$  do
    for  $z \leftarrow 0$  to  $v_z$  do
      if  $volume.mask(x, y, z) == vessel$  then
         $transverse.at(x, y) \leftarrow 1$ 
        break
      end if
    end for
  end for
end for
```

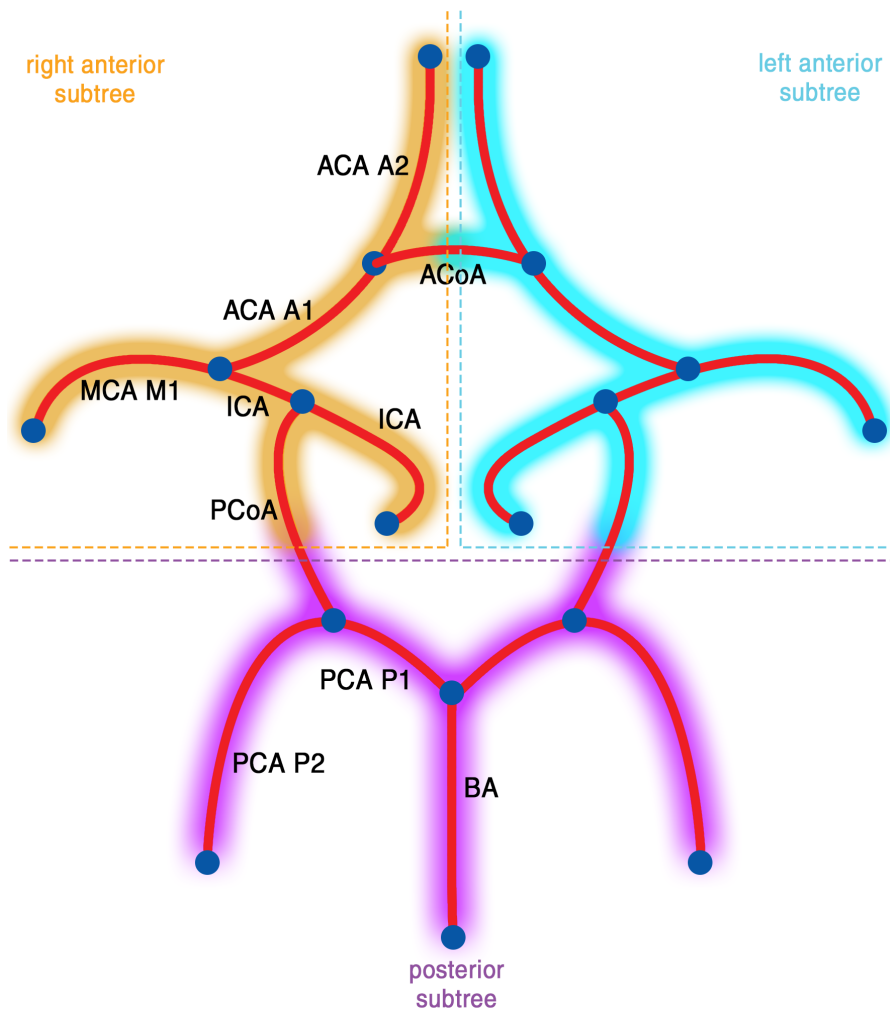


Figure 3.9: A scheme of the arterial circle clustered into three subtrees. The orange part is associated with the right anterior subtree, the cyan part with the left anterior subtree and the violet part with the posterior subtree.

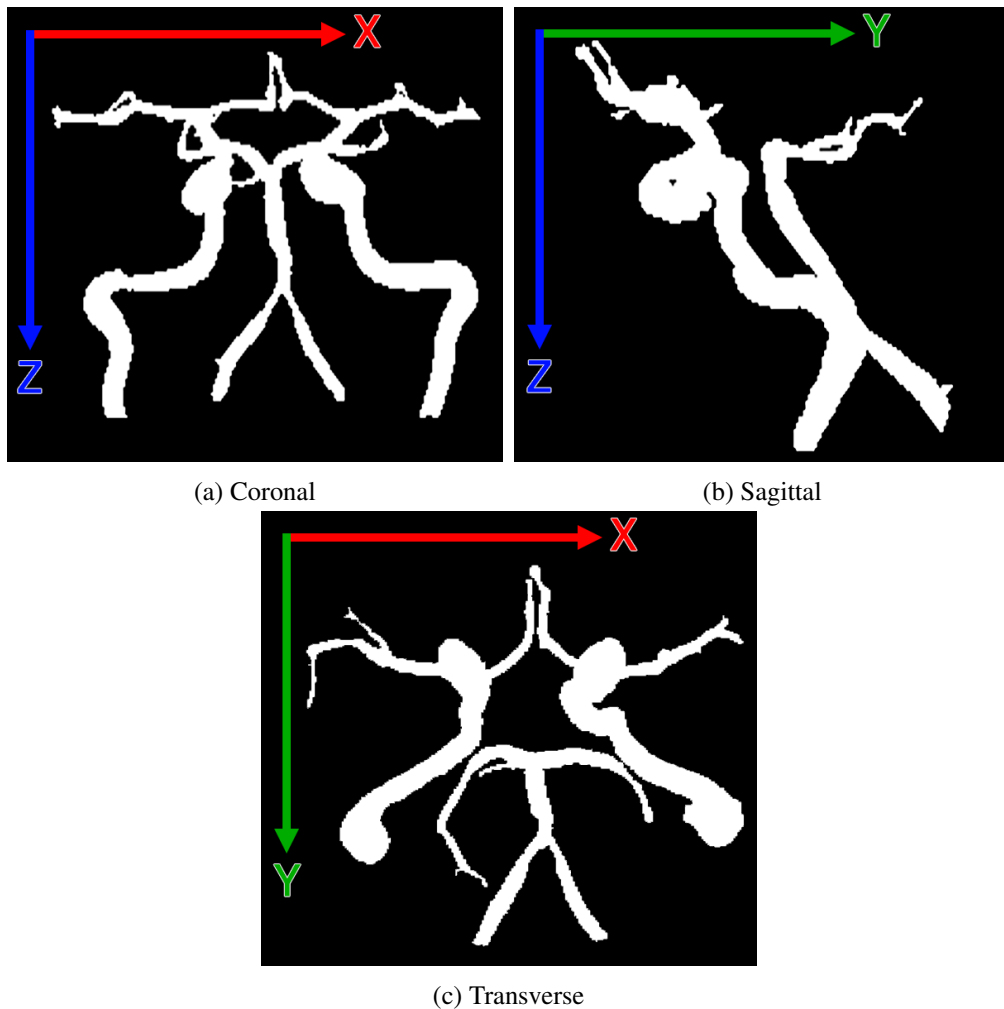


Figure 3.10: The segmentation results are projected along the three axes into binary images.

coronal plane in Figure 3.10 shows, the basilar artery is normally enclosed by the two carotid arteries. This circumstance is exploited to get a better separation. For this reason, a ray casting method is additionally applied. Rays are shot from left and right. Only the areas that are hit first by the rays keep their markings. After the first hit, the ray terminates when it hits a background point. Algorithm 5 describes the details of this method, where the rays are cast along the positive x -direction in order to mark the right anterior subtree. For the left anterior subtree, an equivalent algorithm is implemented, that casts the rays along the negative x -direction. Figure 3.11 (a) shows the result. The orange marked area is associated with the right anterior tree, whereas the cyan marked area is associated with the left anterior tree. The areas in white are caused by the points that lost their markings, since they could not be reached by the ray. Additionally, the center c_{BA} of the left (cyan) and right (orange) areas is calculated as an approximation of the BA's location on the x -axis.

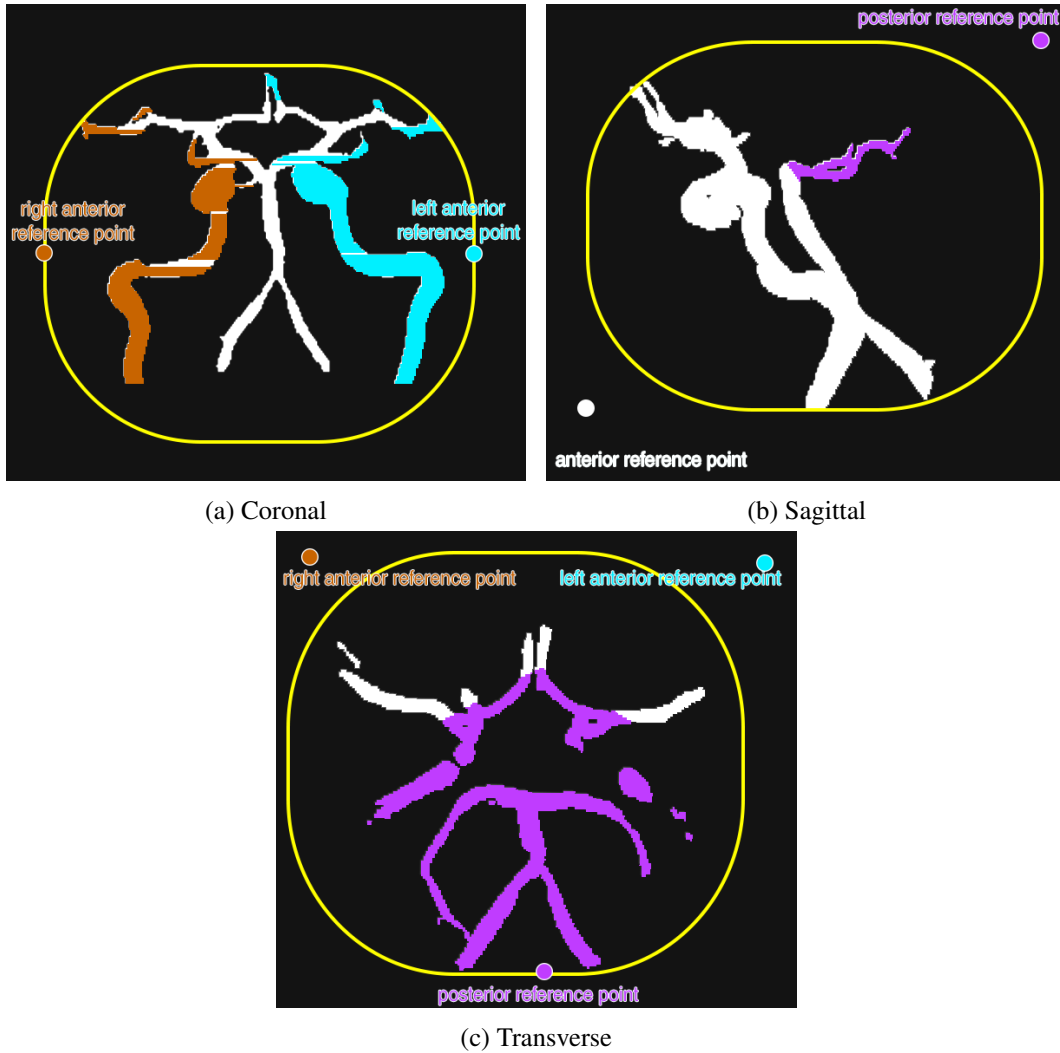
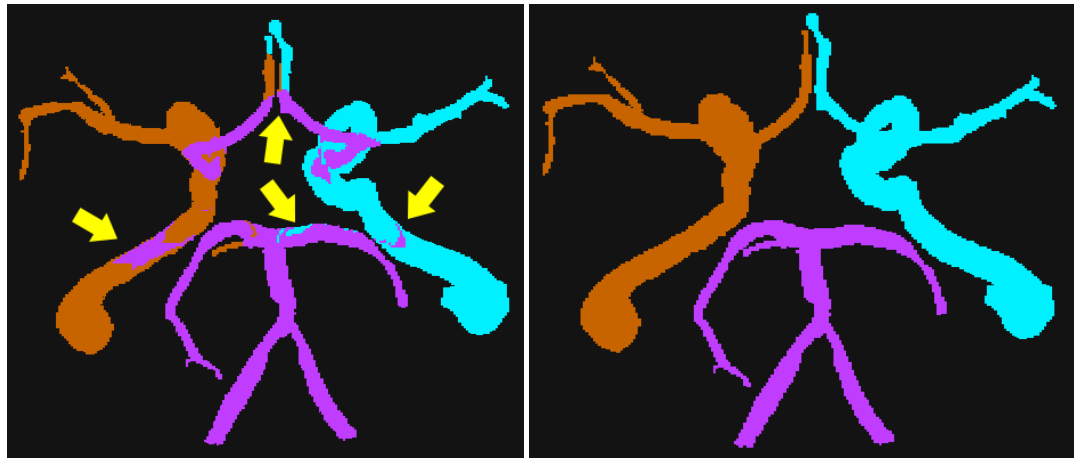


Figure 3.11: The three image planes in Figure (a), (b) and (c) are used to separate the segmentation into three clusters. The orange part is associated with the right anterior subtree, the cyan part is associated with the left anterior subtree and the violet part is associated with the posterior subtree.



(a) The segmentation result marked according to the coronal, sagittal and transverse plane. (b) The final clustering result of the segmented CoW.

Figure 3.12: The Figure (a) shows the resulting volume after Algorithm 6 is applied. The arrows point to small areas that are not assigned to the correct cluster yet. Figure (b) shows the final clustering result of the segmented CoW from the transverse view after the small areas are reassigned according to their larger surrounding areas.

Algorithm 4 The separation of the coronal plane into a left and right part.

Input: The *coronal* plane with reference points $\text{leftRefP} = (p_x - A, p_z + C)$ and $\text{rightRefP} = (p_x + A, p_z + C)$

Output: The separated *coronal* plane

```

for  $x \leftarrow 0$  to  $v_x$  do
  for  $z \leftarrow 0$  to  $v_z$  do
     $p = (x, z)$ 
    if  $\text{plane.at}(p) == 1$  then
      if  $\text{EuclideanDist}(p, \text{leftRefP}) < \text{EuclideanDist}(p, \text{rightRefP})$  then
         $\text{coronal.mask}(p) \leftarrow \text{leftSubtree}$ 
      else
         $\text{coronal.mask}(p) \leftarrow \text{rightSubtree}$ 
      end if
    end if
  end for
end for

```

Algorithm 5 A ray casting algorithm to separate the coronal plane into a left and right anterior subtree without the posterior subtree. The first area hit by the ray is marked respectively. The rest is marked as unknown.

Input: The separated *coronal* plane

Output: A more accurately separated *coronal* plane

```

for  $z \leftarrow 0$  to  $v_z$  do
  firstHit  $\leftarrow$  false
  rayLeftFirstHit  $\leftarrow$  false
  for  $x \leftarrow 0$  to  $v_x$  do
     $p \leftarrow (x, z)$ 
    mask  $\leftarrow$  coronal.mask( $x, z$ )
    if mask == rightSubtree and firstHit == false then
      firstHit  $\leftarrow$  true
    end if
    if firstHit == true and mask != rightSubtree then
      rayLeftFirstHit  $\leftarrow$  true
    end if
    if rayLeftFirstHit == true and mask == rightSubtree then
      coronal.mask( $p$ )  $\leftarrow$  unknown
    end if
  end for
end for

```

The posterior tree is extracted from the transverse plane. The posterior reference point is defined by $(c_{BA}, p_y + B)$, the left anterior reference point is at $(c_{BA} + A, p_y - B)$ and the right anterior reference point is at $(c_{BA} - A, p_y - B)$. The x-coordinate is determined by the c_{BA} value from the coronal plane. The algorithm for the separation into an anterior and a posterior part is equivalent to the Algorithm 4 for the coronal plane. In Figure 3.11 (c) the result is shown where the points are assigned to their nearest reference point. The posterior part is marked in violet. The points nearest to the anterior reference points lose their markings and are displayed in white. In addition, only those voxels that have not been marked by the coronal plane are considered in this step. Figure 3.10 (c) and Figure 3.11 (c) show that the majority of the anterior part is marked as background in the transverse plane.

The sagittal plane is separated in order to mark the P1 segments. The posterior reference point is at $(p_y + B, 0)$ and the anterior reference point is at $(p_y - B, p_z + C)$. Since the left and right anterior parts can not be distinguished from this view, the anterior part is separated by one reference point. Figure 3.11 (b) shows the result.

Next, the segmented voxels in the volume are assigned to the clusters according to the separated planes. Algorithm 6 shows the details. The result is shown in Figure 3.12 (a). As the example in the figure reveals, some parts are still marked incorrectly. In the last step, these small parts will be absorbed by their larger surroundings. Thereby, each subtree computes its largest connected areas using connected component analysis. These three initial areas absorb the adjacent voxels as long as they are not part of one of the two other initial areas. This is a

breadth-first algorithm that guarantees the subtrees to be homogeneous. The final result is shown in Figure 3.12 (b).

Algorithm 6 The voxels in the volume are marked by the planes.

Input: The separated *coronal*, *sagittal* and *transverse* planes and the not yet clustered *volume*.

Output: The clustered *volume*.

```

for  $x \leftarrow 0$  to  $v_x$  do
  for  $y \leftarrow 0$  to  $v_y$  do
    for  $z \leftarrow 0$  to  $v_z$  do
       $p \leftarrow (x, y, z)$ 
       $volume.mask(p) \leftarrow transverse.mask(x, y)$ 
       $volume.mask(p) \leftarrow coronal.mask(x, z)$ 
       $volume.mask(p) \leftarrow sagittal.mask(y, z)$ 
    end for
  end for
end for

```

The subdivision of the CoW into three subtrees reflects the physiological property of the arterial supply of the circle. Each subtree is supplied through one of the three main arteries. The clustering is the first step in the identification of the main arteries and in addition provides a rough classification of the arteries in the CoW into their respective subtrees. This information proved to be beneficial in the labeling phase.

The drawback of the proposed method is the reliance on the position and shape of the super-ellipsoidal ROI. An unfavorable placement of the ROI causes an inaccurate subdivision of the segmentation result. Furthermore, this approach employs knowledge about the shape and location of the CoW. This makes it rather inflexible if the initial conditions change. However, the main benefit of this approach is less the detection of the present parts of the CoW but rather the identification of missing parts as discussed in the next section.

Missing Artery Detection

As already mentioned, the anatomy of the CoW shows substantial variance. The geometry and topology is greatly influenced by the way the circle is supplied through the main arteries, the LICA, RICA and the BA. These main arteries have a major influence in the configuration of the CoW. In diagnosis, they act as visual guides due to their large size.

The labeling of the structure of cerebral arteries has been discussed by Bilgel et al. [2] and Bogunovic [4]. Each concentrated on different aspects of the labeling step. However, what they have in common is the identification of the main arteries at a late phase in their processing pipeline. In this work, a method for detecting the absence of these supplying arteries in an early phase of the pipeline is suggested.

The main arteries are the largest arteries in the CoW. If one is missing, the number of high intensity voxels drops considerably in the respective subtree. Exploiting this circumstance, the absence of a main artery can be detected by using the clustering method described in Section 3.2. The method is demonstrated on an example CoW with missing RICA shown in Figure 3.13. In

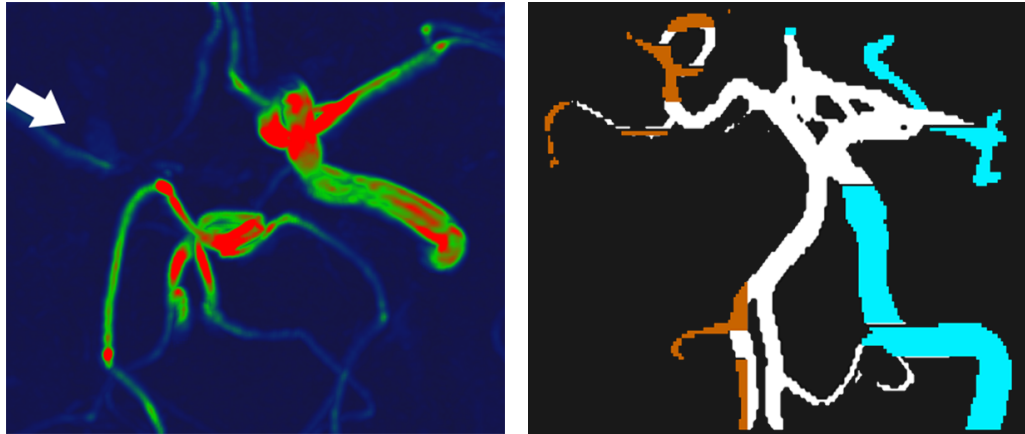
the MIP, we can see that the right anterior tree is not visible. The missing RICA causes the coronal plane to be subdivided unevenly. Figure 3.13 (b) displays the coronal plane of the example. The plane is separated using the previously described approach. The figure shows that the left part (cyan) is substantially larger than the right part (orange). By comparing the size of the left and the right part in the coronal plane, it can be derived that the RICA is missing. In general the ratio of a part to the other has to be smaller than 35% in order to be detected as missing. This is an empirical value that showed good performance with the provided data sets.

The presence of the BA is assessed using the same approach in the transverse plane. If the ratio of the posterior part falls under 10%, the BA artery will be detected as missing. If a main artery is missing, the CoW is divided into two instead of three subtrees. Figure 3.13 (c) displays the clustering result of the example CoW. We can see that only the left anterior and the posterior subtree are clustered. This is a far more representative separation of the CoW than to assume that there are always three subtrees present.

Skeletonization

A skeletonization algorithm is applied in the pipeline after the segmentation in order to create the basis for the vascular tree model. We use the method described in Section 2.5. Due to the tubular structure of blood vessels, the skeleton is a suitable representation of the vasculature. This, however, relies on the assumption that the segmentation of the vessel is of high quality. This assumption is not always met since the MRAs may exhibit artifacts that cause the segmentation method to perform poorly. These artifacts are the cause of noise in the segmentation. Small arteries are particularly affected by this circumstance. As a consequence, the small arteries with low intensity values tend to be disconnected in the segmentation result. Additionally, the low intensity voxels inside the arteries can cause holes in the segmentation. Figure 3.14 shows an example where noise produces holes. This circumstance causes considerable problems for the thinning based skeletonization method. Since skeletonization is prone to noise or changes of the boundary of the object, post-processing operations are applied. Otherwise, the noise can result in circles in the extracted centerline, which then will not be representative due to the changed topology. One option is to decrease the low threshold (t_l) in the HT approach in order to avoid the holes. However, this is problematic since it bears the risk of segmentation leakage where surrounding soft tissue will be detected as vessels, leading to an unsatisfying result.

Therefore, morphological operations are suggested to post-process the segmentation result. A closing operation is applied to fill the holes in the segmentation. The outcome is displayed in Figure 3.14. A 3x3 structuring element is used. Larger holes however can not be filled. Applying a structuring element with larger dimensions would be problematic since it would falsely connect arteries. For that reason, a flood fill algorithm is applied additionally after the morphological operations to make sure that there are no larger holes left inside the segmentation. Hereby, the voxels in the volume either belong to the segmented arteries or to the background. The approach used for this work flood-fills the background of the volume. The algorithm takes two parameters: the start voxel and the target mask of the segmented arteries. It starts at a background voxel and iteratively flood-fills the connected voxels. The origin voxel (0, 0, 0) of the volume is chosen as the start, since it is outside of the head and is therefore unlikely to contain a segmented artery. The filling stops at the segmented areas.



(a) The transverse MIP.

(b) The coronal plane.



(c) The division of the CoW into two subtrees.

Figure 3.13: The missing artery detection method is demonstrated on an example CoW with the RICA missing. Figure (a) shows the MIP, where the arrow points to the location of the missing artery. Figure (b) displays the separated coronal plane. The right part is significantly smaller than the left, which is used as an indicator for the missing RICA. The CoW is then clustered into the left anterior (cyan) and the posterior part (violet). The clustered CoW is shown in Figure (c).

Afterwards, the volume is divided into three parts: flood filled background, arteries and unfilled areas. The unfilled areas are then added to the segmentation since they are assumed to be holes inside the segmentation. In contrast to the closing operator, the flood fill algorithm only detects *hollow* areas inside the segmentation results, whereas *closing* plugs small tunnel-like gaps in the segmentation as well. These two complementary methods guarantee a segmentation result where holes and gaps are removed. The resulting skeleton is then free of small loops. The morphological operations and the flood fill algorithm solve the noise problem in the segmentation without introducing blurriness.

There are problematic areas in the segmentation result of the CoW, that can cause the closing operation to falsely fill gaps between two arteries. The left and right ACA have pathways that are sometimes only separated by a one-voxel-wide gap. Figure 3.15 displays a transverse slice view at the height of the ACAs in the example volume. We can see that the tight gap between the ACAs is filled after the closing operation is applied. This creates a false positive connection between the two anterior parts. Finally, the skeletonization of the post-processed segmentation is applied and the result is used as the input for the construction of a vascular tree model described in the following section.

Vessel Tree Construction

The conversion of the skeleton into a vascular tree model (vessel tree) is key for further analysis. Until this step in the pipeline, the CoW had been represented in voxel space. Now the skeleton has to be converted into a vessel tree consisting of nodes and edges in three-dimensional space.

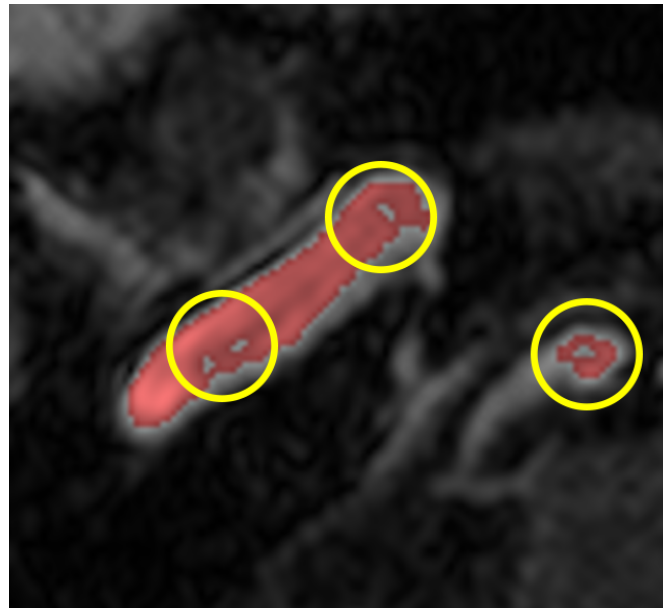
For the construction of the vessel tree this work applies the conversion rules defined by Pock [36] described in Section 2.5. The control points (CPs) are inserted at the position of the skeleton voxels with 1 or 3 neighbors, since they depict either end-points or branching points. The segments are determined by tracing along the voxels with two neighbors. Figure 3.16 demonstrates the conversion with an example in two-dimensional space. The resulting vessel tree of the example volume is shown in Figure 3.17.

Vessel Tree Pruning

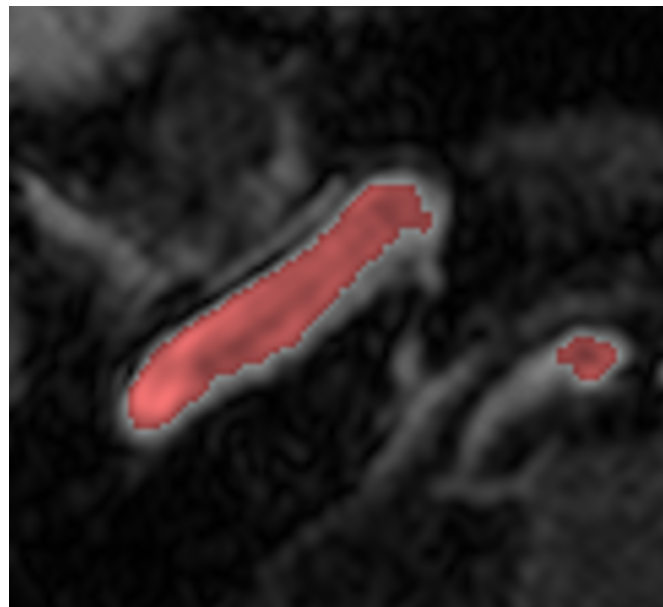
After the conversion, the vessel tree has to be post-processed in order to remove noise introduced during the segmentation and skeletonization phase. This assures a more accurate representation of the vasculature by the vessel tree. In this way, artifacts can be dealt with by discarding particular short and doubled segments. This is motivated by the physiology of the CoW.

Bifurcation Merging

The conversion rules described in Section 2.5 tend to disconnect the tree at the bifurcations. The thinning algorithm tends to leave multiple skeleton voxels with three or more neighbors at the bifurcations. By applying the third conversion rule on the skeleton voxels, multiple CPs at the bifurcations are created. This causes the vessel tree to disconnect at bifurcations. Figure 3.18 illustrates this case with a two-dimensional example. Both skeleton voxels with three neighbors are converted into CPs, causing the vessel tree to disconnect at this point as shown



(a) Before closing



(b) After closing

Figure 3.14: Noise causes holes in the segmentation. Figure (a) demonstrates this problem, where low intensity values create small holes in the RICA and BA, indicated by the circles. The holes are closed by the closing operator using a 3x3 structuring element.

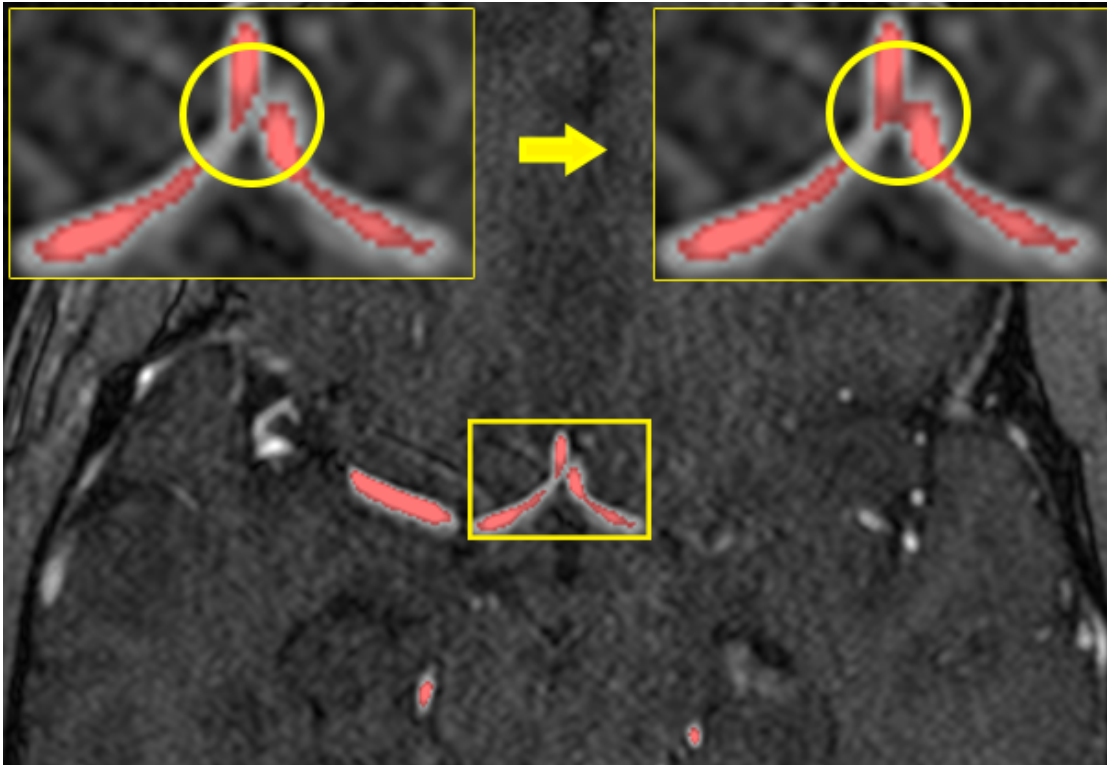
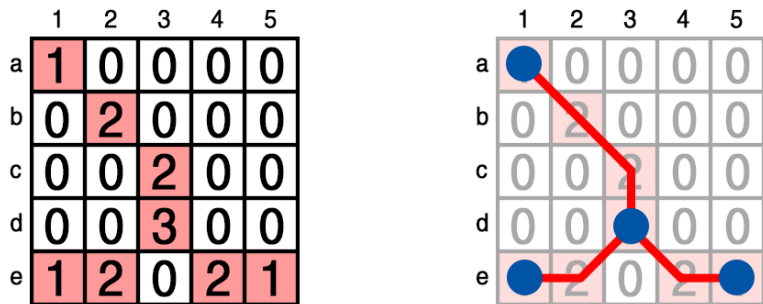


Figure 3.15: The closing operation falsely closes the tight gap between the ACAs.



(a) The red cells represent the skeleton voxels where the number defines the number of neighbors in the 8-neighborhood.

(b) The converted vessel tree where the control points are represented by the blue circles and the segments are represented by the red edges.

Figure 3.16: The construction of a vessel tree from skeleton voxels.

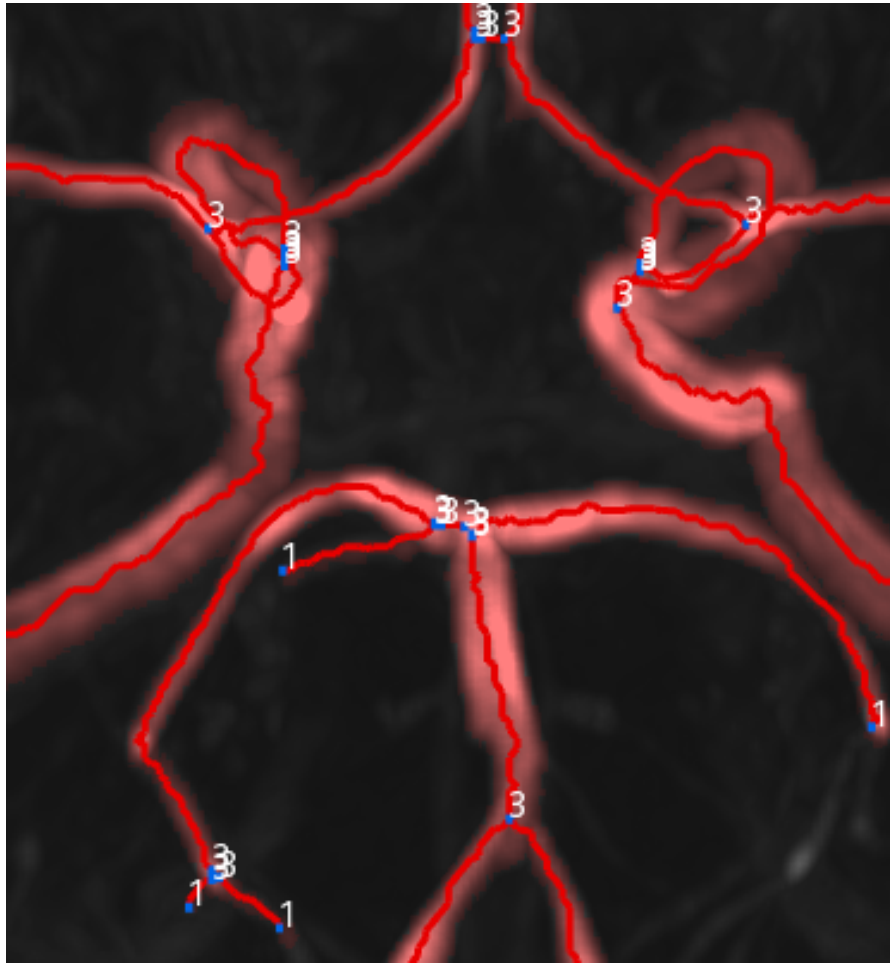
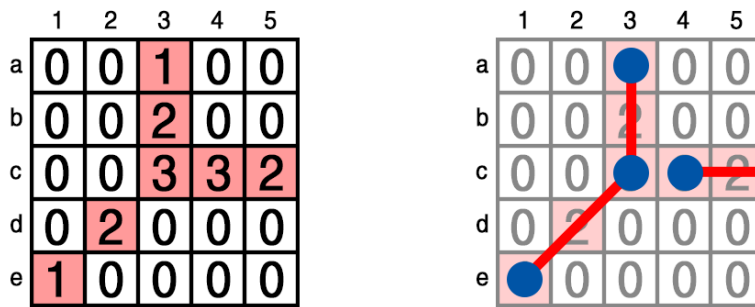


Figure 3.17: The vessel tree of the example volume before pruning. The control points are shown with the number of neighbors in the skeleton. The vessel tree disconnects at the bifurcations.

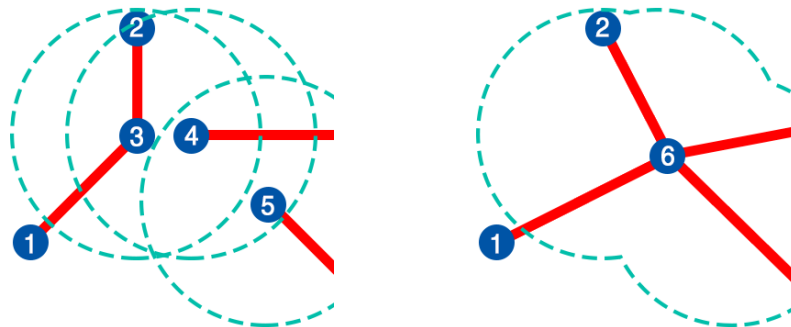
in Figure 3.19 (a). In this figure an approach for the reconnection of these CPs is shown. A CP is considered as a candidate for reconnection if it has CPs with degree one inside a small search radius around the CP. The idea is that these end-points that are in close proximity to each other, must be part of a bifurcation that is disconnected by using the conversion rules. If an unconnected CP is found inside the search area, the search will be continued inside the new CP's search radius. In the example, the *CP 3* detects the *CP 4* as unconnected inside its radius. The search area is then extended and the *CP 5* is added to the merging area as well. A new CP is added at the center and replaces the initial CPs. The segments are connected to the new CP as shown in Figure 3.19 (b).



(a) An two-dimensional example of a skeleton, where two of the voxels count three neighbors.

(b) Using the conversion rules, two control points are inserted at the bifurcation. The vessel tree disconnects at this bifurcation since these short gaps between the CPs are not connected by segments during the conversion.

Figure 3.18: Illustration of the disconnected bifurcations during the conversion from skeleton to vessel tree.



(a) The search radius around the CPs 3, 4 and 5.

(b) The merged bifurcation. CP 2 is not merged since it is already connect to one of the initial CPs.

Figure 3.19: Illustration of the merging of a disconnected bifurcation.

Segment Merging

The merging of disconnected segments is an important step to create a representative vessel tree for the CoW. As discussed before, disconnections are caused by artifacts in the volume. The physiology of vessels suggests that they can not simply disconnect and maintain the blood flow. Based on this knowledge, it is safe to assume that small gaps between segments are noise. Therefore, removing small gaps creates a more accurate vessel tree.

A small search radius around the CPs is defined to look for candidates. Figure 3.20 demonstrates the reconnection and merging of two disconnected segments and the subsequent removal of duplicate segments. Double connections are physiologically possible but they can also appear from artifacts, especially in short segments. Figure 3.20 (a) shows an example where the CPs 7 and 8 are disconnected. They are reconnected in Figure 3.20 (b) and the CPs are deleted. In Figure 3.20 (c), the shorter segment between CP 6 and CP 9 is deleted, since it is considered to be noise due to its shortness. This is motivated by the idea that the shorter segment is more likely caused by noise than the longer segment. Removing a duplicate segment affects the degree of CP 9. With only two connected segments the CP is deleted and the segments are merged, as shown in Figure 3.20 (d).

The above-proposed vessel tree pruning methods are feasible techniques to deal with the noise introduced during the preceding steps and by artifacts in the volume. However, the pruning can not distinguish between noise and correct segments. This results in the removal of short segments that actually represent hypoplastic arteries. This poses a limitation of this proposed method which was revealed during the evaluation.

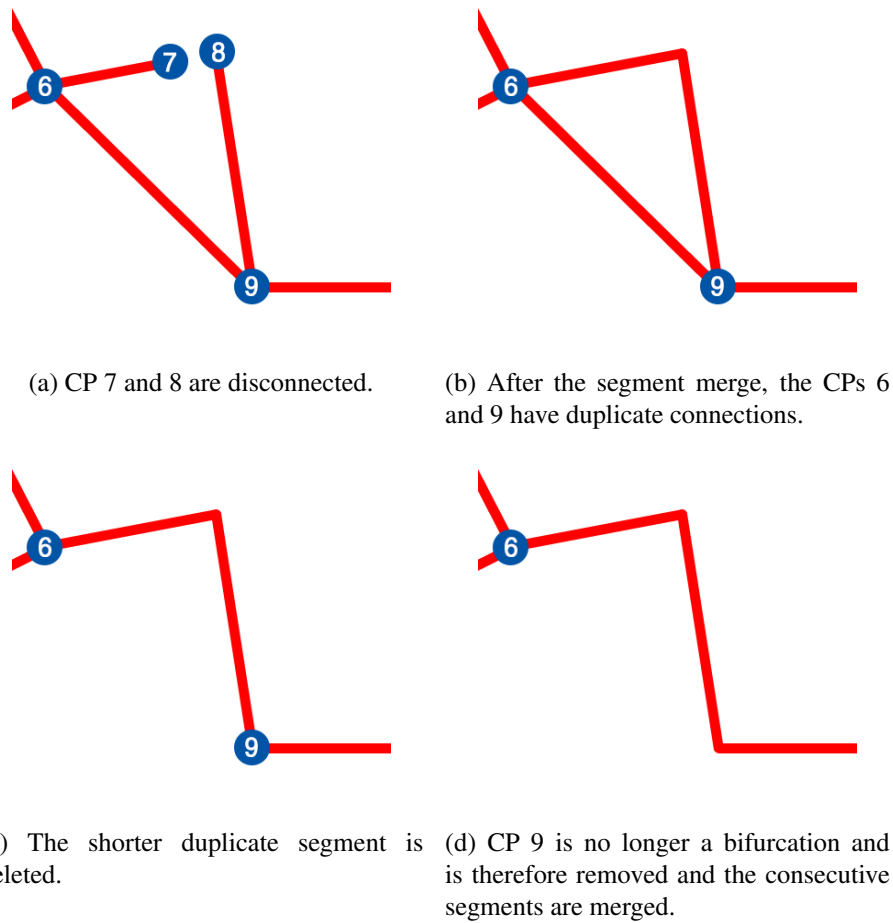


Figure 3.20: Illustration of segment reconnection and the removal of duplicate segments.

3.3 Anatomical Labeling

This thesis proposes a labeling approach which is not focused on identifying the Latin names of the arteries but rather their source of blood supply. Figure 3.9 displays a scheme of the CoW with its names. Assigning the correct Latin names of vessels is not a trivial task since they have been developed historically and not systematically. This makes automated labeling rather complex and difficult, since there are many rules and special cases to consider. As a consequence, many labeling approaches in the literature are restricted to certain anatomical structures.

Usually, arteries carry their name through one or more segments. An arterial segment is defined as the part between two branching points. The presence of an artery is defined by its preceding artery that guarantees its supply. This work suggests a systematic labeling method on the basis of the enumeration of the arterial segments in the CoW, starting from the main arteries LICA, RICA and BA. The approach was developed during the active collaboration with our domain expert. It is based on the assumption that the radiologist is better assisted by a simple

display of how the parts of the CoW are supplied (or rather which regions are not supplied) than by the Latin names of arteries.

The enumeration value is based on the distance of a segment to the main arteries. Each segment is defined by the number of bifurcations that lie between them and the three main arteries. The correct detection of the starting segment for this method is essential. A heuristic approach is suggested in the following.

Root Segment Selection

The two anterior arteries LICA and RICA are normally composed of two or more segments in the volume while the BA is normally composed of only one segment. These main arteries are set as the starting point of the labeling approach. One segment of these arteries is defined as the *root* of the enumeration. The segments are characterized by certain attributes, which are explained in the following:

1. **Length l .** The main arteries are very likely long compared to the other arteries in the CoW.
2. **Position on the z-axis u .** The position on the z-axis u is significant since the main arteries supply the CoW from below. Therefore, their position on the z-axis is likely to be lower than the other arteries of their subtrees.
3. **Centrality on the x-axis v .** The centrality attribute v is required for the BA root segment. Normally, the BA has the most central position on the x-axis. The value is calculated as the average distance between the points on the segment and c_{BA} . If the LICA or RICA is missing then the center point of the ROI p_x is used since c_{BA} is not computed in this case.
4. **Distance to the centroid of the cluster d .** Each subtree has a cluster centroid, which is usually very close to its main artery, since the main artery is the largest one in the subtree. The number of voxels belonging to the main artery is relatively large compared to the other arteries. Hence, the root segment must be close to the centroid of its cluster. d is calculated as the average Euclidean distance between the points in the segment and the centroid.
5. **Brightness b .** Due to the properties of MRAs, the main arteries have the highest intensity values. This, however, depends on the scanning parameters.
6. **Spatial alignment a .** The main arteries run vertically upwards until they bifurcate into the CoW. The vertical alignment is an important feature that characterizes them. The pathway of a segment is simplified by a vector between the start and end CP. The angle a between this vector and the z-axis is computed as an abstraction of the segment's alignment in the volume.
7. **Affiliation to the respective subtree s .** Each subtree is supplied through one main artery. This means, for each subtree, only those segments are considered to be candidates for the respective root segment which are actually part of the cluster. LICA and RICA share

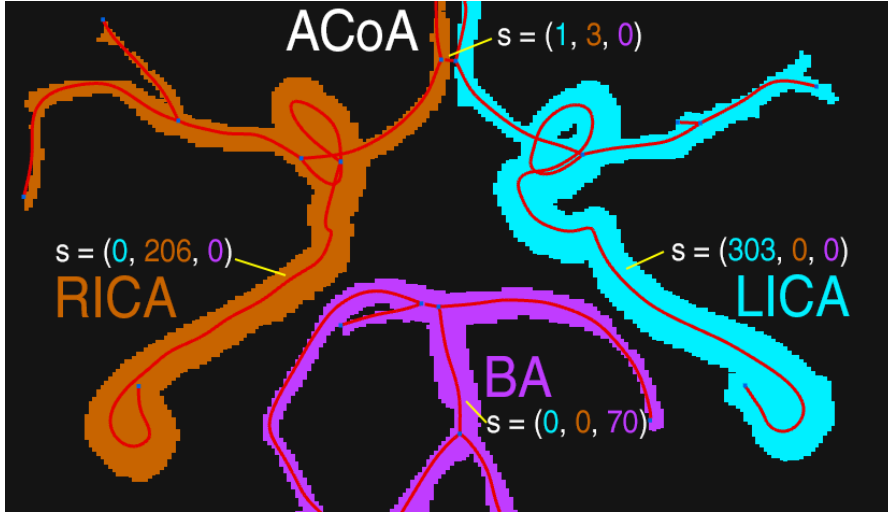


Figure 3.21: The Figure demonstrates the calculation of s for the example segments. For instance, the vector for the ACoA of the example volume is $s = (1, 3, 0)$. The first component refers to the number of voxels in the left anterior subtree, the second component to the number of voxels in the right anterior subtree and the third component to the number of voxels in the posterior subtree. The segment is four voxels long, whereby the vector shows that 1 voxel is part of the left anterior subtree and 3 are part of the right anterior subtree. It is therefore considered as a candidate for both subtrees.

similar attributes. The s attribute ensures that the LICA is selected as the root of the left anterior subtree and the RICA for the right anterior subtree. A segment can be part of either one or two subtrees. s is calculated from the clustering result described in Section 3.2. s is therefore a three-dimensional vector which counts the number of cluster voxels in the segment's pathway. This is demonstrated on the example volume in Figure 3.21

For each segment in the vessel tree, a final rank is computed based on the suggested attributes. Hereby, a cost function is used in order to select the root segments with maximal rank. Equation 3.7 defines the cost function:

$$C_{i,j} = \text{sgn}(s_{i,j}) \cdot (l_i \cdot L_j + u_i \cdot U_j + v_i \cdot V_j + d_i \cdot D_j + b_i \cdot B_j + a_i \cdot A_j) \quad (3.7)$$

$C_{i,j}$ is the rank of segment i to be selected as the root of subtree j , where $j = 1, 2, 3$. The variable $s_{i,j}$ is the component j of affiliation vector s of segment i . It describes which subtree the segment i can be assigned to. The variables $l_i, u_i, v_i, d_i, b_i, a_i$ define the attributes of segment i , which are mapped to values between 0 and 1 in order to standardize the range. $\text{sgn}(\cdot)$ is the sign function, which is defined as

$$\text{sgn}(k) = \begin{cases} 1 & \text{if } k > 0 \\ 0 & \text{if } k = 0 \\ -1 & \text{if } k < 0 \end{cases}$$

If a segment is not part of a cluster then $sgn(s_{i,j})$ is 0. Consequently, the final rank $C_{i,j}$ is also 0. This guarantees that a segment is only considered as a candidate for its respective subtree. The influence of the attributes is regulated by the factors $L_j, U_j, V_j, D_j, B_j, A_j$, which function as weightings. However, the root segments for LICA ($j = 1$), RICA ($j = 2$) and BA ($j = 3$) are not determined by the same attributes. For this reason, the weightings have to be adjusted accordingly. $L_1 = 0.4, U_1 = 0.2, V_1 = 0, D_1 = 0.5, B_1 = 0.5, A_1 = 0.2$ are the weightings for the LICA and RICA root segment. Hereby, the centrality attribute v is eliminated, since the LICA and the RICA are in the lateral part of the ROI. Otherwise, v would favor other segments over LICA or RICA. For the BA root the weightings are $L_3 = 0.3, U_3 = 0, V_3 = 1, D_3 = 0.3, B_3 = 0.4, A_3 = 0.8$. Hereby, u is eliminated since the BA is not the lowest segment in the posterior subtree. Usually the two vertebral arteries are below the BA. v has the largest influence with $V_3 = 1$ since the BA is most likely located near the middle axis of the ROI. The weightings of the attributes are empirically motivated. The best ranked segment is then selected as the root segment for the respective subtree.

The selection of the correct root segments and therefore the identification of the main arteries is crucial for the accurate labeling of the CoW. A wrong root segment causes the entire subtree to be labeled incorrectly, since it starts at the wrong segment. Nevertheless, the clustering approach described in Section 3.2 and the above described artery attributes turned out to be robust in the detection of the root segments in the provided data sets. The main advantage of this approach is the fast and straightforward computation.

Vessel Tree Labeling

Starting from the root segments, the vessel tree is segment-wise labeled. The enumerator at the root segments is 0 per definition. At each branching point the enumerator is increased by 1. The labeling term is declared by the following regular expression:

$$[RLB][0 - 9]^+[a - z]$$

The capitals R, L and B specify the root segment where R stands for the RICA, L for LICA and B for the BA. The next numerals specify the number of branching points between the segment and its root segment. Lower case characters at the end declare the number of the branch at the bifurcations. The branching number is thereby mapped to a letter in order to distinguish it from the number of branching points, which is defined by a number. A segment in the vessel tree has between zero and three labeling terms. It has no labeling terms if it is not connected to any root segment and three labeling terms if it is connected to all three root segments. The final label is composed of these labeling terms, depending on how it is connected to the root segments.

This labeling approach is illustrated in Figure 3.22. The segments are subsequently labeled starting at ROa . The first branching point has two subbranches: a and b . Figure 3.23 illustrates a standard CoW that is labeled with this approach. The tree is traversed in a breadth-first manner. This means that the neighbors are labeled first before moving to the next neighbor level. As the example shows, there are some segments with the same term, since they have the same number of branching points between them and the root. However, by labeling the tree from three directions the uniqueness of the labels can usually be ensured.

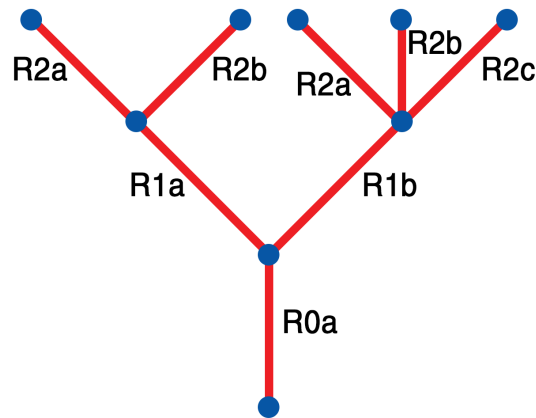


Figure 3.22: Illustration of the labeling method on a tree example. The enumerator increases with the number of branching points. In addition, it indicates the direction the tree is labeled.

The benefit of this approach lies in its flexible nature. It is not restricted to the CoW but can be applied to other tubular structures in the human body as well. Each arterial segment is described by its connection to its supplying arteries.

With the labeled segments, the configuration of the circle can be comprehended by this textual description of the segments. We demonstrate this by using an example label $R0aL5aB8a$. The $R0a$ term describes the root segment of the right anterior tree, which is part of the RICA. The $L5a$ term indicates the presence of the LICA, which is separated by five branching points, hence five segments from the LICA root segment. The fact that the RICA root segment is enumerated from the left anterior tree after all already implies the presence of the ACoA since the left and right anterior tree are connected by this artery. Furthermore, the $B8a$ term requires a connection to the posterior tree, which is guaranteed by the PCoA. Yet, the high enumerator implies that the segment is labeled through the left anterior tree. Consequently, it can be assumed that the arteries are not connected in a circle, since the right PCoA might be missing. However the left PCoA must be present, otherwise the label would not carry the $B0a$ term from the posterior tree. This example demonstrates the expressiveness of our labeling approach. It has been shown that the configuration of the CoW can be captured using the proposed method. The labeled vessel tree allows swift interpretations of the CoW's configuration. It forms the basis for a comprehensive description of the CoW. For future work, a rule-based system is suggested that assigns the correct Latin names to the segments based on this labeling method. For example, the $R3aL3a$ is likely to be the ACoA since the label indicates its position to be in the middle of the two anterior trees. Furthermore, various configurations of the CoW can be identified considering these labels.

There is a current drawback of this method as the vessel tree is assumed to be correct. As discussed before, an erroneous vessel tree hampers the interpretability of the labels. Especially disconnections and the false segmentation of soft tissue result in inaccuracies of the vessel tree. For future work, the segmentation step in the pipeline can be exchanged for a more robust method that is not prone to artifacts in the volume.

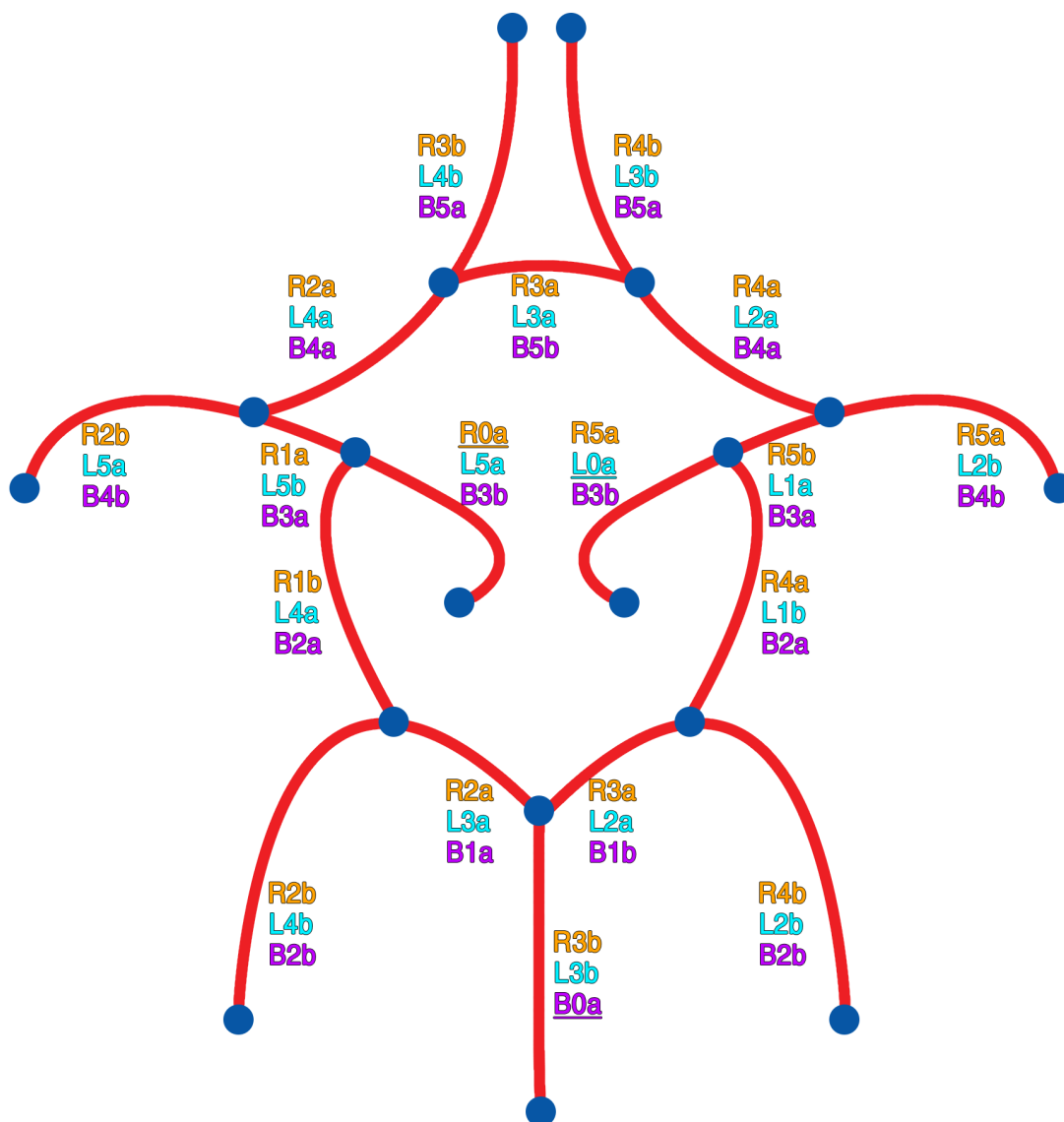


Figure 3.23: Illustration of the labeling of the standard CoW. The segments are labeled starting from each main artery (root segment), which are underlined. Since the standard configuration of the CoW has all communicating arteries, each segment receives three labeling terms. The left anterior root segment is the $R5a\underline{L0a}B3b$, the right anterior root segments is the $\underline{R0a}L5aB3b$ and the posterior root segment is the $R3bL3b\underline{B0a}$.

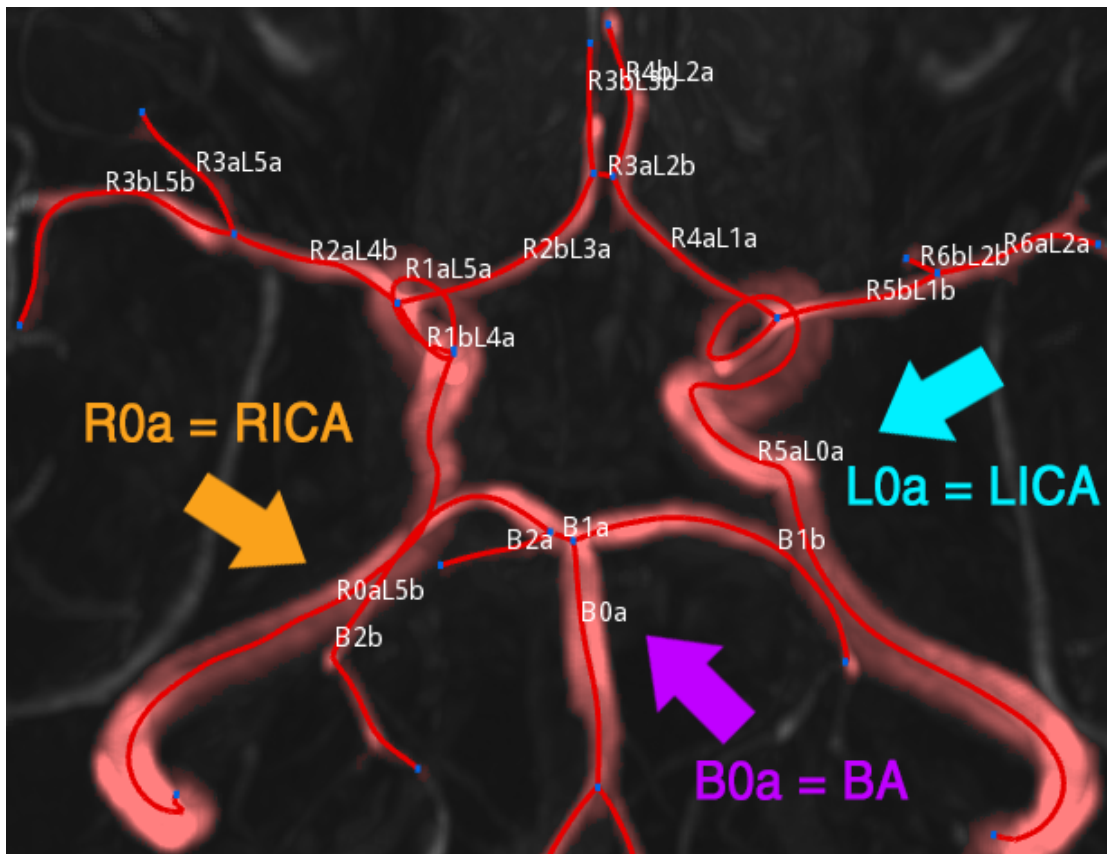


Figure 3.24: The vessel tree of the example volume labeled with the proposed approach. The root segments are selected correctly, indicated by the arrows. The labels show that the anterior part is separated from the posterior part since both PCoAs are missing. The left and right anterior subtrees are connected by the $R3aL2b$ segment, which is the ACoA.

3.4 Visualization

Visualization plays a key role in medical imaging. The previous steps proposed in this work are necessary to build the foundation for visualization techniques. MIPs and slice views are commonly used techniques in the clinical routine. These methods allow the radiologists detailed insights into the patient's CoW and constitute indispensable tools. However, they only display one patient at a time. The analysis of multiple volumes and the comparison of them is time-consuming. For a larger number of data sets, this is not only an inconvenience but a restriction, since it would require too much time. Furthermore, they can not simply be viewed side-by-side. In this section, a standardized visualization is proposed that visually quantifies the CoW in a TOF-MRA and provides a simple and quick overview of the cerebral arteries.

The benefit of a standardized visualization are manifold. It guarantees that a CoW is always displayed in the same way, no matter how it is configured. This has the potential to offer a preliminary assessment of the patient's status before deeper investigations. It enables the radiologist

a very quick assessment at one glance. In addition, it acts as an abstract display of the CoW's configuration. The simplified description of the arteries could guide the attention of the viewer to problematic areas. Knowing where to look is potentially time saving and in the end benefits the patient. Furthermore, displaying the CoW in the same way provides quick comparisons between different CoWs. These swift comparisons enable to draw conclusions from a vast number of patient data.

3D Vessel Tree to 2D Graph Conversion

The vessel tree contains information about different properties of the CoW, which have to be visually displayed. This section proposes a method that organizes the information and visualizes it in a diagrammatic form. The goal is to give a graphical description of the CoW and its connected arteries. The inclusion of a standardized layout and colors enable a simple comprehension of otherwise complex information content. In order to organize the information in a meaningful way, the labeled vessel tree has to be converted to a two-dimensional vessel graph first, which is defined by the following rules:

- For each segment in the vessel tree an equivalent node in the vessel graph is created.
- Root segments are converted into starting nodes.
- For each branching point an edge in the graph is inserted between the nodes in the direction of the increasing enumerator.

At this point it is important to mention that the nodes of the vessel graph represent the segments and not the branching points of the vasculature. This representation might be unconventional for medical practitioners but we chose this approach on the basis of the following reasons. The first and most important motive is to standardize the display of the different configurations of the CoW. We abstract the CoW as much as possible and dissociate the visualization from the traditional representation of the CoW. A segment, much like an edge, has a length and a pathway. Encoding this information in an edge would restrict the standardization since the edges would have different appearances. Furthermore, segments carry different attributes such as length, intensity values etc. that could be important to the viewer. Therefore, we assume that the nodes are more suited to display the different attributes than edges. We suggest that all segments are represented equally by nodes no matter of their length or pathway. The different attributes are instead depicted in a diagram inside the node.

Figure 3.25 shows the vessel graph of the example volume's CoW. Even without the spatial information the topology of the vasculature can be clearly perceived. The three starting nodes represent the root segments of the supplying arteries. The BA is not connected to the anterior subtrees since both PCoAs are missing. The anterior subtrees are connected by the ACoA.

The vessel tree model is converted into a vessel graph described in the DOT language. As previously mentioned, the GraphViz framework can be employed to draw a graph that is formally described using the DOT language. It is drawn using the program *neato*, which is part of GraphViz. The next step is to create a standard layout of the CoW.

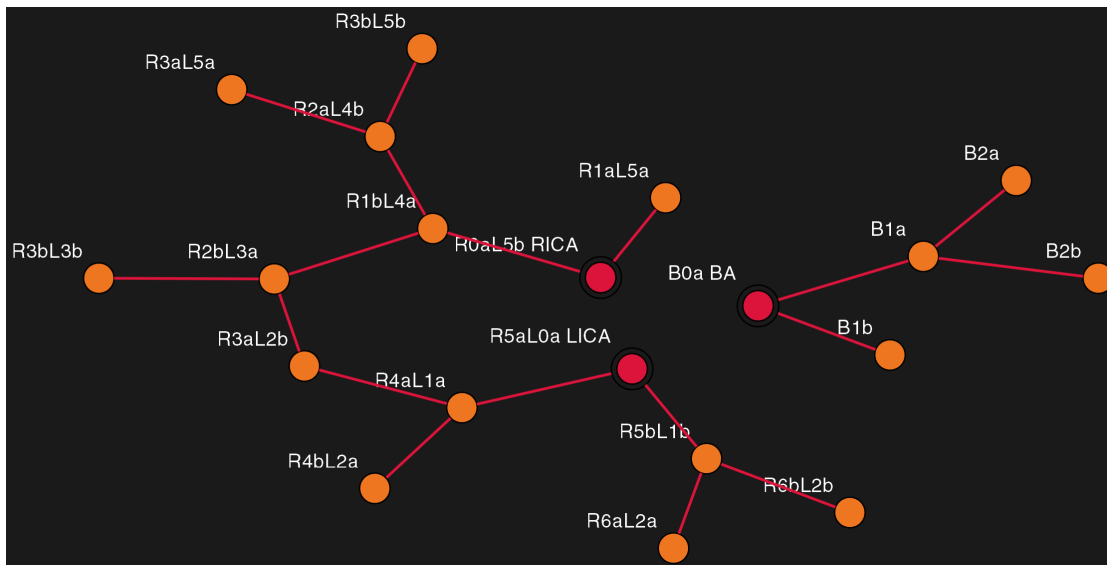


Figure 3.25: The example volume's CoW represented by a graph. The red double contoured nodes represent the root segments and the orange nodes represent the segments of the CoW. The edges define the connectivity between the segments along the direction of the blood flow. In the graph the disconnection between the anterior trees and the posterior tree is immediately observable.

Standardized Visualization

The standardization in the display of the CoW helps to increase its comprehensibility. In general, standardization organizes information in such a way that the viewer's expectation is satisfied. It allows the viewer to focus on the content instead of the concept of a visualization. The graph described in Figure 3.25 is to some degree standardized. The arteries and its bifurcations are displayed in the same way by the colored nodes and edges. However, the layout follows various goals such as minimizing crossing edges and the total area of the graph. Another configured CoW will result in a completely different layout. This makes the comparison of the vessel graphs rather inconvenient.

Using DOT and the GraphViz environment is too restrictive for a standardized display of the CoW. Therefore, we implemented our own graph drawing method to display the CoW in a standardized layout based on a radial layout. This visualization is referred to as radial vessel graph. The main concept of this visualization is grounded on the following ideas:

1. The circular arrangement of the arteries suggests a radial layout.
2. A standardization creates an interface to compare the CoWs from multiple patients.
3. A standardized visualization is an interface for the communication between multiple parties such as the radiologist and the neurologist.

The reason we propose this radial layout of the vessel graph instead of a traditional display such as the illustration in Figure 1.1 lies in the variability of the CoW and its representation in a TOF-MRA. The illustration is well-suited to display the standard-configured CoW but the high variability that is observed in the provided data sets could be potentially problematic for this illustrative depiction. The scans are mostly acquired from patients who suffer from a stroke, which is highly related to an abnormality in the CoW. In addition, a pathological artery can be represented much differently than a healthy one in TOF-MRA, which is currently a challenge for the labeling. Finally, the extraction of the CoW from a TOF-MRA and the representation in such an illustration require a correctly labeled vessel tree with their Latin names, in order to provide the depiction that the viewer associates with the CoW. To the best of our knowledge, the anatomical labeling of the full CoW is a challenge that has not been solved yet. Even Bogunovic [4], who most recently proposed a promising approach could only label 60% of the CoWs correctly. Therefore, we propose our radial vessel graph to display the arteries that can be actually detected from the TOF-MRA. In our work, we identify the three main arteries and use them to systematically label the vessel tree. Using the radial layout for the vessel graph organizes the segments in such a way that they can be easily associated with actual shape and topology of the CoW, but does not require a fully (Latin names) labeled vessel tree. Furthermore, the presence and absence of certain arteries is depicted in the visualization, which can provide valuable information and indicate problematic areas.

The radial vessel graph potentially offers benefits for clinical practice. The main challenge is finding a visualization method that is able to capture the complex structure of the CoW and still is expressive itself. The preceding steps in the pipeline described in this work are intended to extract the data necessary for a standardized visualization.

The visualization consists of two parts: The first is a method to display the overview topology of the CoW. Figure 3.26 shows the CoW of the example volume using the proposed method. The radial vessel graph is subdivided into three sectors (R, L and B) based on the physiological arrangement of the CoW in three subtrees. The left and right anterior subtrees in the L- and R-sector are shown in the cyan and orange sector and the posterior subtree in the violet B-sector. The color gradient indicates the transition between the subtrees since the communicating arteries are the connections between the subtrees but are assigned to only sector. The right anterior part is depicted on the left side of the figure and vice-versa, because of the traditional way the medical volume is viewed by radiologists, which is normally from the transverse view.

The nodes represent the segments and are positioned at the levels depending on their distance to their root segment. The level at which a segment is placed is derived from the enumerators of its labeling terms, which indicate the number of branching points between them. The root segment is positioned at the level 0 in the respective section.

The connectedness of the segments along the blood flow direction is indicated by the edges. As described in Section 1.2 the supplying arteries come together at the base of the brain and form the CoW. In Figure 3.26 the arc-shaped edge between a node of the R- and the L-sector exists because of the connection between the left and right anterior subtree (R3bL3b - R3aL2b), which can be interpreted as the ACoA.

This radial vessel graph provides a standard display of the CoWs configuration. Figure 3.26 shows the simple radial vessel graph of the example volume. The viewer can immediately see the

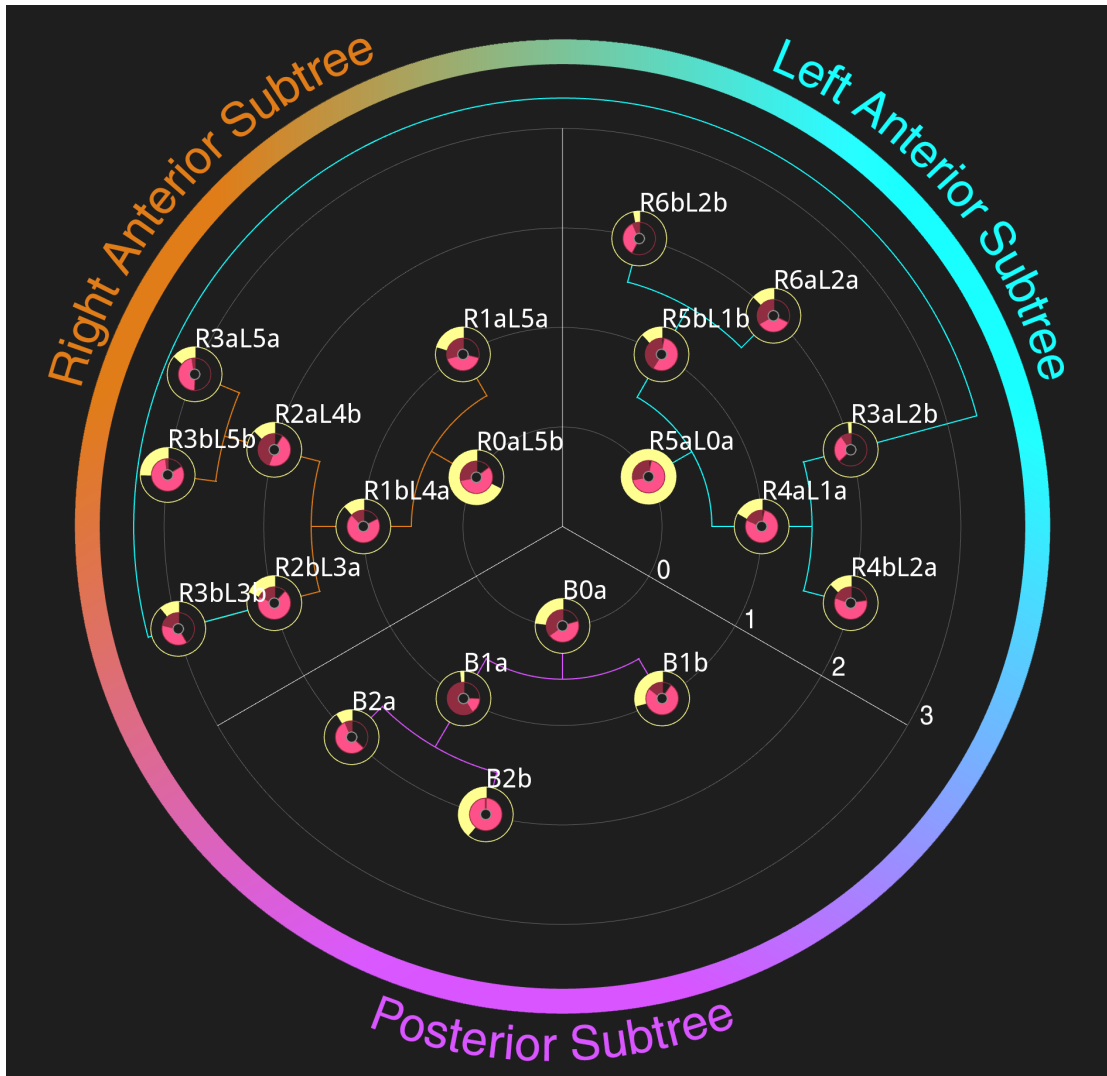


Figure 3.26: The radial vessel graph of the example volume using the proposed method. The nodes represent the segments in the CoW. Each sector represents a subtree of the CoW. The connections between the subtrees are indicated by the arc-shaped edges. In this case, the connection between the L- and R-sector is established by the ACoA (R3aL2b). The detailed attributes are displayed inside the nodes by radial bars. The gradient represent the transition between the subtrees.

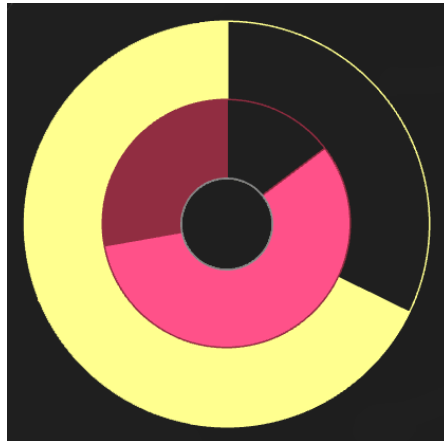


Figure 3.27: The figure shows a detailed view of the right anterior root segment in the radial vessel graph, where the node itself is a radial diagram with multiple bars. The attributes of the segment are encoded in the radial bars, where the inner (red) bar displays the intensity values along the pathway of this segment and the outer (yellow) bar encodes the segment's length in voxels. The bars increase in counter-clockwise direction. The first bar is divided into two parts: the first, shorter part displays the minimum intensity value and the second, longer part depicts the maximum intensity value of this segment. The values depend on the maximum intensity value of all segment points.

connection between the L- and R-sector indicated by the arc-shaped edge. In fact, the connection is established by the ACoA. Furthermore, his attention is guided to the posterior part since the B-sector seems to be not connected to the others. As a matter of fact, both PCoAs are missing in our example volume as confirmed by our domain expert.

The second part of the visualization is to provide further insights into the vasculature. Segments differ in length, thickness and have many attributes. These attributes can be visualized in the node itself, which is a radial diagram with multiple bars. Figure 3.27 shows the root segment of the right anterior tree. The attributes are displayed by the radial bars, which show the values in proportion to the maximum value of all segments. The inner bar displays the intensity range. The outer bar shows the length of the segment. The RICA segment (R0aL5b) is fairly long hence the bar is almost full. The second bar reveals two values: the minimum and the maximum intensity value of the segment. This radial bar diagram is convenient, since it shows many attributes in a compact space. These two attributes have already been discussed for the selection of the root segment since they characterize the main artery. For the same reason, they are encoded in the radial vessel graph in order to provide details about the arterial segment. However, the individual bars could encode different attributes depending on the information the radiologist is interested in.

The graph is based on the labeled vessel tree model. According to our domain expert, there is a huge number of angiographies saved on the Picture Archiving and Communicating System (PACS). These scans are not utilized for research or diagnostic purposes since the manual investigation of the volumes consumes a substantial amount of time. In this case, the automated

processing capabilities of the proposed methods in this work can be harnessed. Each angiography could be visually quantified and described by the radial vessel graph. For future work, the automated construction of a database may be a well-suited application for the proposed methodology.

3.5 Implementation

The methods described in this section were implemented within the AngioVis framework [18]. It defines a data structure for handling medical data and the vessel tree model. Furthermore, it provides the basic visualization techniques needed for the User Interface (UI) such as a slice view or MIP. From a software development point of view, it was more pragmatic to extend the functionality of AngioVis instead of developing an entire new visualization software.

The current implementation of the proposed method is fully automated. In order for the proposed method to be potentially applied in the clinical environment, it is essential that it does not introduce new work steps. Hence, the user interactions are reduced to a minimum.

The processing of a data set is as simple as pressing a button. A common challenge for a fully automated method is its generality. It has to be prepared for each and every special case, which is a challenging task. A UI for automated processing of TOF-MRAs has been implemented. In addition, the UI is prepared for the manual processing of special cases as well. A screenshot of the implemented software is displayed in Figure 3.28. The purpose of the slice view is to provide a detailed analysis of the volume whereas the MIP allows a rough overview. The final result is the radial vessel graph, which is displayed in the lower right of the UI shown in Figure 3.28.

Workflow

The main use case of the application requires the radiologist to open the volume and start the processing pipeline. No further adjustments have to be done since the pipeline processes the volume automatically. However, special cases may require the additional adjustments of certain parameters. As discussed before, the pipeline has critical parts that heavily influences the subsequent methods. The placement of the ROI is a crucial step in the early phase. If the arteries are not covered by the ROI they cannot be detected. Usually, the ROI is automatically computed on the basis of the segmented skull. However, a deviation from the initial conditions may influence the effectiveness of this method. For this reason, the super-ellipsoidal ROI can be placed and shaped manually. The ROI can be adjusted in the slice view by dragging the slice-intersecting super-ellipse as shown in Figure 3.28 on the left side.

Another critical part is the segmentation, which is determined by the t_h and t_l threshold values. They are computed on the basis of a histogram analysis. The domain expert is more capable to judge the segmentation result and if necessary he/she can adjust these parameters. Thus, it is necessary to provide the appropriate interaction methods for the domain expert to carry out these steps manually. The last critical part is the selection of the root segments. The selection depends on the influence factor of the attributes. The influence of each attribute can be regulated in the user interface.

Technique	Average Computation Time (in seconds)
Skull detection	2.11
Placement of ROI	1.28
Histogram computation and t_h/t_l estimation	0.83
Extraction of vasculature	31.28
Morphological operations	1.72
Skeletonization	15.84
Vessel tree conversion	0.42
Vessel tree pruning	0.51
Labeling	0.27
Conversion to vessel graph and radial vessel graph	0.36
Total time	54.62

Table 3.1: The average performance of each step in the pipeline tested on 63 data sets. The measurements were done on an *Intel Core i5 @ 3.4 GHz / 16 GB RAM*.

For the provided data sets we observed that in about three out of 63 cases, the manual adjustment could potentially improve the results. The details are discussed in the following chapter.

When the automated pipeline finishes processing, the domain expert can inspect the results of our approach in three viewing sections:

- A multi-axial slice view.
- A 3D MIP rendering blended with the extracted vessel tree and its labels.
- A radial vessel graph.

The automated pipeline contains various methods with benefits and drawbacks. The manual adjustment of certain parameters enables the handling of special cases, which otherwise would be processed incorrectly. However, the automated approach was tested in a study described in the next section. It has been shown that the accuracy of the proposed methods is close to that of a radiologist. Consequently, the manual processing of the volume would only increase the results in some special cases.

Performance

In order for the techniques to be operational, it is necessary that they terminate in adequate time. The techniques described in this thesis are implemented on the CPU. The performance of the individual steps is shown in Table 3.1 (based on the average processing times for 63 data sets). The volume size varies between $448 \times 512 \times 64$ and $512 \times 512 \times 156$ voxels. The voxels are represented by *16 bit unsigned integers* where 12 bits are used for the intensity values and the remaining 4 bits for the mask. The final performance is dependent on the volume size.



Figure 3.28: The figure displays the UI of the software developed as a part of this thesis. On the left side, the slice view of the figure is shown. The yellow super-ellipsoid displays the slice-intersection of the super-ellipsoid and the selected transverse slice. The shape and size of the ROI can be adjusted herein. In the middle column the histogram is displayed. The button for the automated execution of the proposed method and the elements for the manual execution of the proposed method are visible in the control panel. A MIP of the volume as well as the vessel tree and its labels are displayed in the upper right. The lower right window displays the corresponding radial vessel graph visualized using the proposed method.

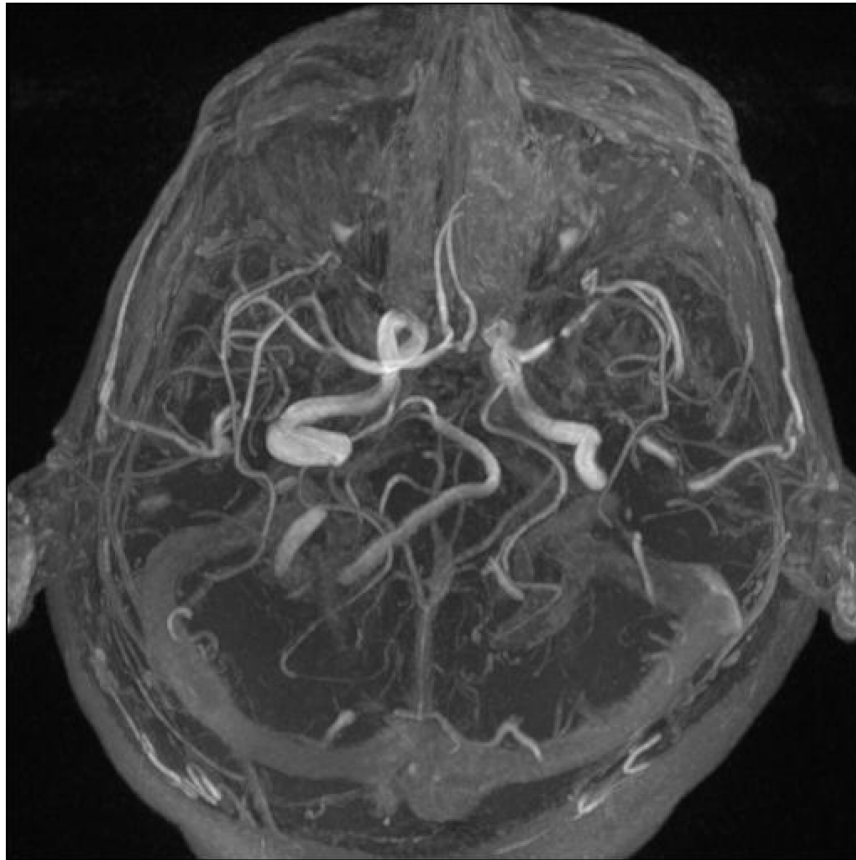
3.6 Summary

This section described a number of methods for the visual quantification of the CoW. Some of them are already well-established methods in image processing such as skeletonization and the conversion to a vascular tree model. However, a method for the labeling of the CoW has been introduced. The second part is the novel visualization method of the CoW. The visualization of a data set requires a correctly extracted vascular model. The pipeline described in this section is a series of methods that aims to create a representative model. However, due to variations in the patient's anatomy and image quality this requirement can not always be fulfilled. Inaccuracies and errors especially in the early phase of the pipeline can cause a snowball effect resulting in an inaccurate visualization. For this reason, the automated pipeline is complemented with manual adjustments. However, this work is not focused on a particular part but rather on the development of an entire pipeline that is necessary to visually describe the configuration of the CoW.

Results

The methodology described in Chapter 3 has been evaluated in a study of 63 data sets acquired with 3D TOF-MRA at the radiology department of the Universitätsklinikum Tulln [19]. The data sets were acquired from patients with different diseases. Most are acquired from stroke patients. Among them are also patients with brain tumors and other cerebrovascular diseases. The volume size varies between $448 \times 512 \times 64$ and $512 \times 512 \times 156$ voxels. The volumes were automatically processed using the proposed methodology, without manual adjustments. As a comparison, the data sets were studied by our experienced domain expert, who is an expert neuro-radiologist and three volunteering radiologists. Their task was to identify the presence of the following 12 cerebral arteries of the CoW.

1. the main arteries supplying the CoW:
 - a) Internal Carotid Artery Left (LICA)
 - b) Internal Carotid Artery Right (RICA)
 - c) Basilar Artery (BA)
2. the arteries forming the CoW:
 - a) Anterior Communicating Artery (ACoA)
 - b) A1 segment of Anterior Cerebral Artery Left (A1-ACA-L)
 - c) A1 segment of Anterior Cerebral Artery Right (A1-ACA-R)
 - d) M1 segment of Middle Cerebral Artery Left (M1-MCA-L)
 - e) M1 segment of Middle Cerebral Artery Right (M1-MCA-R)
 - f) Posterior Communicating Artery Left (PCoA-L)
 - g) Posterior Communicating Artery Right (PCoA-R)
 - h) P1 segment of Posterior Cerebral Artery Left (P1-PCA-L)



Please mark the arteries if they can be detected in the image above.

- 1. Internal carotid artery left (LICA)
- 2. Internal carotid artery right (RICA)
- 3. Basilar artery (BA)
- 4. Anterior communicating artery (ACoA)
- 5. A1 segment of anterior cerebral artery left (A1-ACA-L)
- 6. A1 segment of anterior cerebral artery right (A1-ACA-R)
- 7. M1 segment of middle cerebral artery left (M1-MCA-L)
- 8. M1 segment of middle cerebral artery right (M1-MCA-R)
- 9. Posterior communicating artery left (PCoA-L)
- 10. Posterior communicating artery right (PCoA-R)
- 11. P1 segment of posterior cerebral artery left (P1-PCA-L)
- 12. P1 segment of posterior cerebral artery right (P1-PCA-R)

Figure 4.1: This is an example of the questionnaire that was filled in by the participating radiologists and the expert neuro-radiologist. In addition to the transverse MIP, they were allowed to analyze the raw data on their workstations.

i) P1 segment of Posterior Cerebral Artery Right (P1-PCA-R)

For this comparison, the radiologists analyzed the raw data on their workstations and marked the identified arteries in a standardized questionnaire. Another example is shown in Figure 4.1. The answers of the experienced neuro-radiologist are taken as the ground truth that is referred to as the gold standard. To verify the methods of this work, the visually quantified results were compared against this gold standard. The results from the radiologists were also compared against the gold standard. The sensitivity, specificity and Negative Predictive Value (NPV) are computed to measure the ability to identify the arteries in the CoW.

The results of the study are considered as binary classifications. The sensitivity metric, or true positive rate, measures the proportion of existing segments that could be correctly identified. The specificity metric, or true negative rate, measures the proportion of missing arteries that could be detected as absent. Finally, the NPV is the proportion of the correctly classified absent arteries. In order for the proposed methodology to be considered to have good performance, all three of these metrics have to be relatively high. They are defined in the Equations 4.2, 4.3 and 4.4. The effectiveness of our methodology is compared against radiologists.

The approach in this work uses a labeling strategy where the Latin names of the segments are not obtained, except for the main arteries. Therefore, the visualized results of our approach had to be interpreted by our domain expert, who verified if the arteries could be correctly identified. This evaluation was done with a special UI composition that is shown in Figure 4.2. The results are shown with three display methods. The first is the radial vessel graph of the extracted CoW. In Figure 4.2 the RICA node is selected, which is highlighted in yellow in the vessel tree. The segmentation result is displayed in the slice view, where the voxels are marked in red. For the evaluation, the expert selects the nodes in the visualization and checks the corresponding segments in the 3D vessel tree view. The slice view is used to verify if an artery is correctly detected by our approach.

In order for an artery to be considered as correctly detected by our approach, it has to fulfill the following prerequisites:

1. An artery has to be assigned to the correct respective subtree in the radial vessel graph (L-, R- or B-sector).
2. The point at which the artery originates has to be detected. However, if an artery is represented in more segments in the model than it actually has, it is still regarded as correct. An arterial segment could be represented by more than one segment in our radial vessel graph. We consider a segment as the part between two branching points. However, noise in the volume could cause false branching points. Therefore, the evaluation tolerate the separation of a true arterial segment into more than one in our radial vessel graph. Otherwise, the evaluation would purely analyze the segmentation approach instead of the entire quantification.
3. Lastly, a segment could be only rated as correctly identified, if more than two-thirds of the entire segment length was detected.

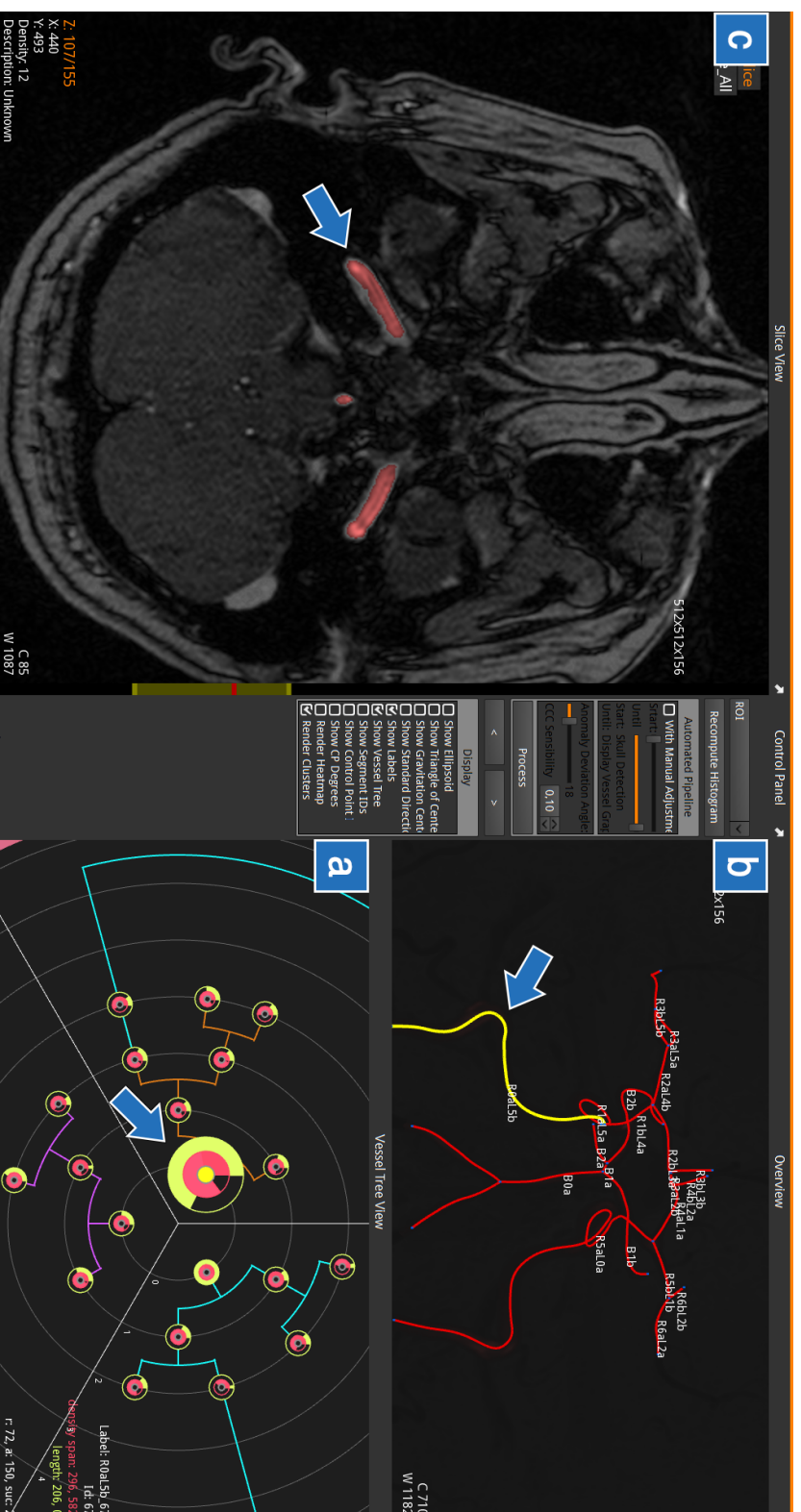


Figure 4.2: The figure shows the UI composition for the evaluation of the results from the proposed methodology. (a) displays the radial vessel graph, the nodes can be selected. The selected node is enlarged as indicated by the arrow. The corresponding segment is highlighted in the vessel tree model indicated in (b). In the slice view, the segmentation is shown in order to evaluate the identity of the extracted arteries. The third arrow points to the segmented voxels in the RICA, which is selected by the expert.

The comparisons between the result of the proposed methodology and the three radiologists are summarized in Figure 4.3, 4.7 and 4.9. Detailed results for individual data sets are presented in the following section where the final visualization of the pipeline as well as the intermediate results of the quantification are displayed.

4.1 Evaluation

The task of identifying the presence of segments in the CoW is considered as a binary classification problem where the segments are either classified as present or not. For the statistical measure the following terms are used:

1. TP is the number of true positive cases. A TP case describes an artery that is regarded as present by the gold standard and by the radiologist/proposed methodology.
2. TN is the number of true negative cases. A TN case describes an artery that is regarded as absent/missing by the gold standard and by the radiologist/proposed methodology.
3. FP is the number of false positive cases. A FP case describes an artery that is regarded as absent by the gold standard, but is considered present by the radiologist/proposed methodology.
4. FN is the number of false negative cases. A FN case describes an artery that is regarded as present by the gold standard, but is considered to be absent by the radiologist/proposed methodology.

The results are then compared to the gold standard and the sensitivity, specificity and NPV metrics are computed for the answers given by the radiologists and the proposed methodology. They reflect the ability of the method to identify the arteries in the circle. The overlap or accuracy metric might be an obvious criterion for analyzing the quality of the results. But it is not feasible for the evaluation of the results in this study due the high number of positive cases (present arteries). The accuracy metric is defined as follows:

$$\text{accuracy} = \frac{\text{TP} + \text{TN}}{\text{TP} + \text{TN} + \text{FP} + \text{FN}} \quad (4.1)$$

Answer	Gold Standard		Total
	Present	Absent	
Present	517	8	525
Absent	107	124	231
Total	624	132	756

Table 4.1: The outcome of the proposed methodology.

Answer	Gold Standard		Total
	Present	Absent	
Present	583	49	632
Absent	58	66	124
Total	641	115	756

Table 4.2: The outcome of radiologist 1.

In the CoW, the majority of the segments is usually present. This circumstance causes the accuracy metric to be generally high even though the answers might be inaccurate. For example, the accuracy for answers where every segment is regarded as present would score an accuracy of 84.7% compared to the gold standard. Yet, this value is meaningless in this case. Therefore, the quality of the results is measured on three criteria: sensitivity, specificity and the NPV. These metrics are defined in the following:

$$\text{sensitivity} = \frac{TP}{TP + FN} \quad (4.2)$$

$$\text{specificity} = \frac{TN}{TN + FP} \quad (4.3)$$

$$\text{NPV} = \frac{TN}{TN + FN} \quad (4.4)$$

Global Evaluation

We compare the sensitivity, specificity and NPV between the three participating radiologists and our approach. Thereby each artery is considered as a single case, which means that there are in total 189 (63×3) cases for the main arteries and 756 (63×12) cases for the arteries of the entire CoW. The separate evaluation of the main arteries and the entire CoW is motivated by the way our approach works. We proposed a method that identifies the main arteries by certain attributes, which we described in Section 2.6. However, the remaining arteries are not directly identified. Our method displays their connections to the main arteries and the branching structure that lies between them, hence the arteries are visually described. The contingency matrices for the TP, TN, FP and FN cases are shown for our approach and the participants in the Tables 4.1, 4.2, 4.3 and 4.4.

Answer	Gold Standard		Total
	Present	Absent	
Present	617	44	661
Absent	24	71	95
Total	641	115	756

Table 4.3: The outcome of radiologist 2.

Answer	Gold Standard		Total
	Present	Absent	
Present	569	27	596
Absent	72	88	160
Total	641	115	756

Table 4.4: The outcome of radiologist 3.

Sensitivity

Figure 4.3 displays the sensitivity of the proposed methodology's and the radiologists' results. They were evaluated against the gold standard. The sensitivity for main arteries is 94.62%, which means that the majority of them could be correctly identified by our methodology. The value shows that the proposed identification of the main arteries is nearly as good as the radiologists are. This task is considered to be an easy task for the radiologists, since main arteries are usually relatively large and clearly visible. However, stenoses, low blood flow and artifacts can cause significant challenges for the proposed methodology. The high sensitivity value at the main arteries shows a good performance of the identification of the LICA, RICA and BA (root segments) by our approach.

For the arteries of the entire CoW, a sensitivity of 80.66% has been achieved. This value is somewhat below the performance of the radiologists. The false identification of the arteries causes the FN cases to increase, which in turn decreases the sensitivity. An increase of FN cases has three explanations. First, the arteries are not correctly segmented due to their low intensity values. The patient in Figure 4.4 was diagnosed with a stenosis in the RICA, which causes the artery to appear with relatively low intensity values. This effects the RICA to be considered *missing* by our clustering method. As a result, the entire right anterior subtree is empty since the subtree is not labeled. But according to the gold standard, the RICA and its supplied arteries are present, which causes the entire right anterior subtree to be incorrectly identified by our approach. In this case the false identification of the RICA causes the right-sided A1 and M1 segments to be false as well.

Second, disconnections or noise in the volume also cause an increase of FN cases. This circumstance is discussed in Section 2.6. Figure 4.5 demonstrates an example where the root segment could be detected but not the supplied arteries due to a disconnection. This is a good example where the radiologists perform significantly better than our approach. The reason is that they are not disturbed by the low intensity values, whereas our approach is not able to reconnected the segments.



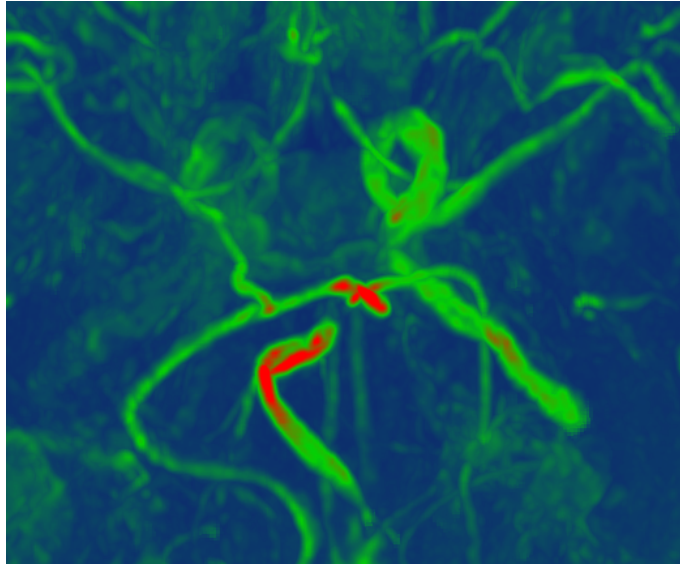
Figure 4.3: Sensitivity. Almost all main arteries could be correctly identified. The arteries in the entire CoW could be detected with a sensitivity of 80.66%. The values show that our approach performs slightly below the performance of the radiologists

Lastly, the communicating arteries appear with low contrast, which causes problems during the segmentation step. As a result, the connections between the subtrees cannot be established. An example is demonstrated in Figure 4.6. It shows that our approach detects the ACoA at the wrong voxels.

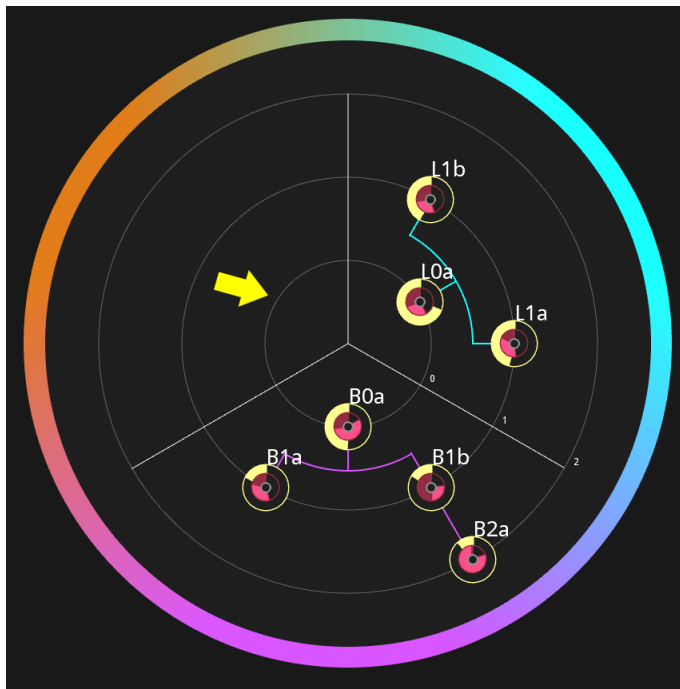
Even though these deviations from the gold standard reduce the sensitivity measurement of the proposed methodology, it can still be regarded to provide an indication of problematic areas. Our approach seems to mostly deviate from the gold standard in those cases where the arteries are represented by relatively low intensity values. In some cases the segmentation approach could not detect the arteries since they could not be distinguished clearly from the background due to low contrast. However, these cases are likely related to pathologies. For example, the stenosis in the patient in Figure 4.4 is clearly indicated by our radial vessel graph. The ability to detect the absence of arteries can potentially be of great interest. This is measured by the specificity and NPV.

Specificity

Figure 4.7 compares the specificity at the main arteries and the entire CoW. According to the gold standard, the RICA is absent in two and the LICA is absent in one data set. All three cases have been correctly classified by the proposed methodology. The specificity is therefore 100%. Only Radiologist 1 seems to agree with the gold standard here. The specificity of the participating

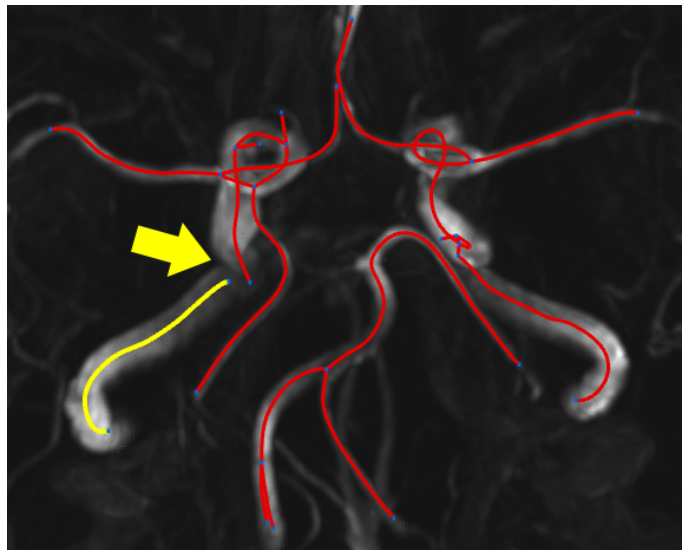


(a) The MIP.

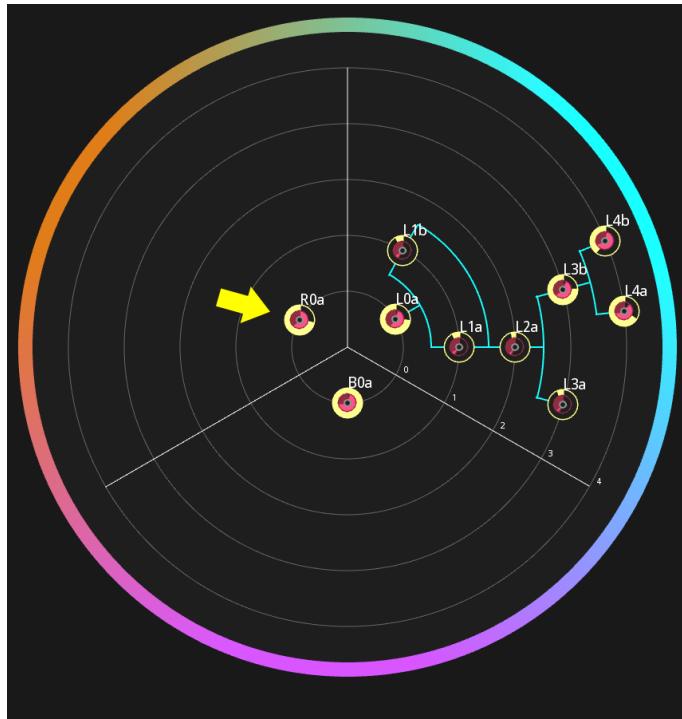


(b) The correspondent radial vessel graph.

Figure 4.4: (a) displays the MIP of an example CoW where the RICA is affected by a stenosis. (b) displays the radial vessel graph. The R-sector is empty since the RICA is considered to be absent. Without the RICA, the entire right anterior subtree can not be identified.

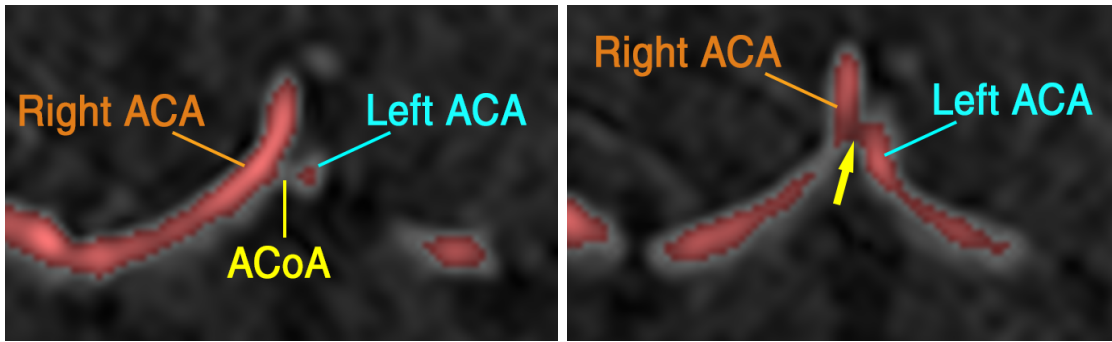


(a) The MIP and the vessel tree.



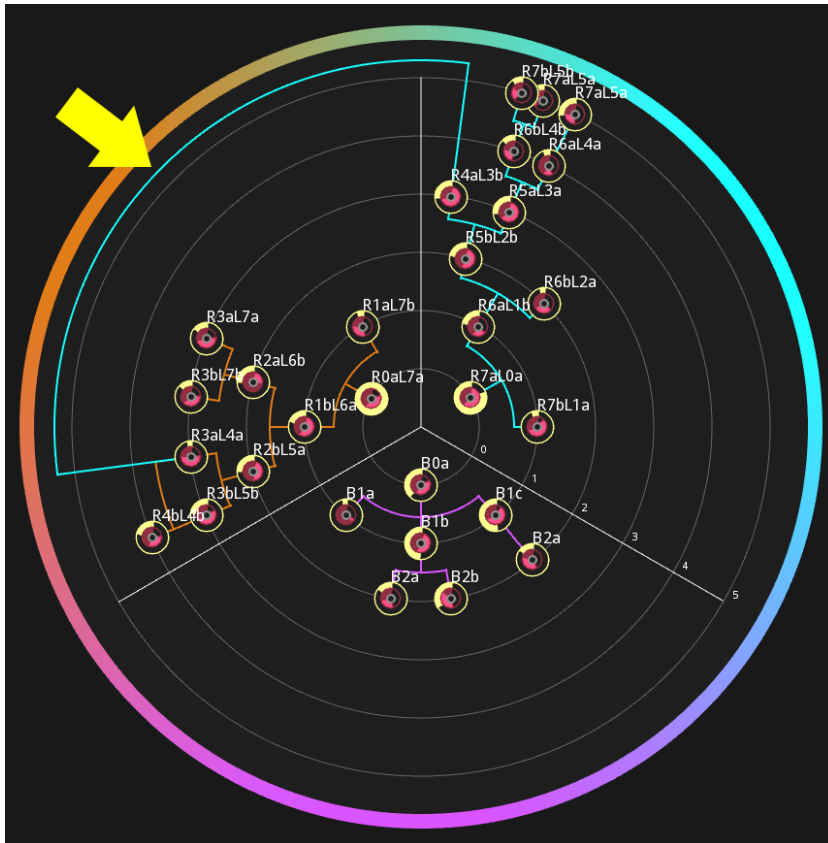
(b) The correspondent radial vessel graph.

Figure 4.5: (a) displays the MIP of an example CoW where the root segment is highlighted in yellow. The arrow points to a disconnection in the RICA, which is caused by low intensity values. (b) displays the radial vessel graph. Only the node for the root segment is shown in the R-sector, which is the RICA. It was correctly identified, but the remaining right anterior subtree could not be identified due to the disconnection.



(a) The actual location of the ACoA.

(b) The falsely detected ACoA.



(c) The radial vessel graph.

Figure 4.6: The figures display the transverse slice view of an example CoW where the ACoA is incorrectly identified by our approach. The segmented arteries are marked in red. (a) displays the transverse slice at $z = 60$ where ACoA is shown. Due to low intensity values, this artery could not be segmented by our approach. (b) shows the slice at $z = 58$. The two ACAs are connected by our approach (which can be interpreted as the ACoA). In the radial vessel graph in (c), the L- and R-sector are incorrectly connected by the cyan arc-shaped edge that represents the connection formed by the ACoA. However, since our approach failed to detected the true ACoA, the artery is considered to be falsely identified during the evaluation.



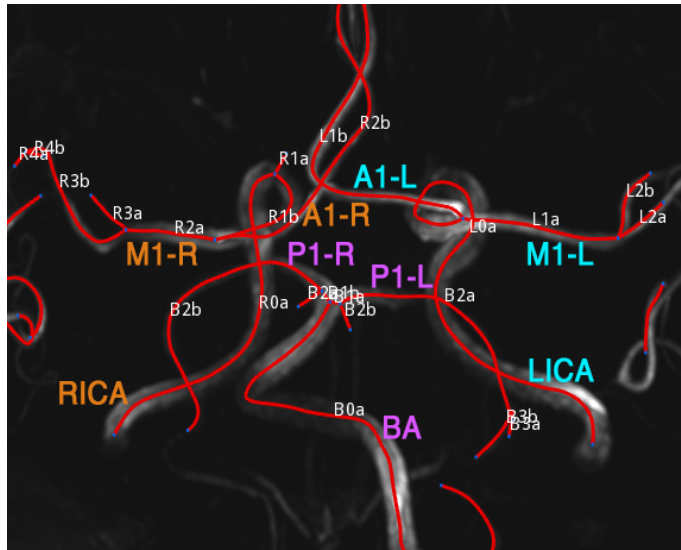
Figure 4.7: Specificity. Our approach identified every case with a missing main artery. A specificity of 93.04% for the entire CoW indicates that our approach performs better in detecting missing arteries.

radiologists is in general lower compared to our methodology. This is because of increased FP cases. The radiologists have the highest FP cases in the communicating arteries, which means they tend to identify the presence of an ACoA or PCoA when the gold standard states the opposite.

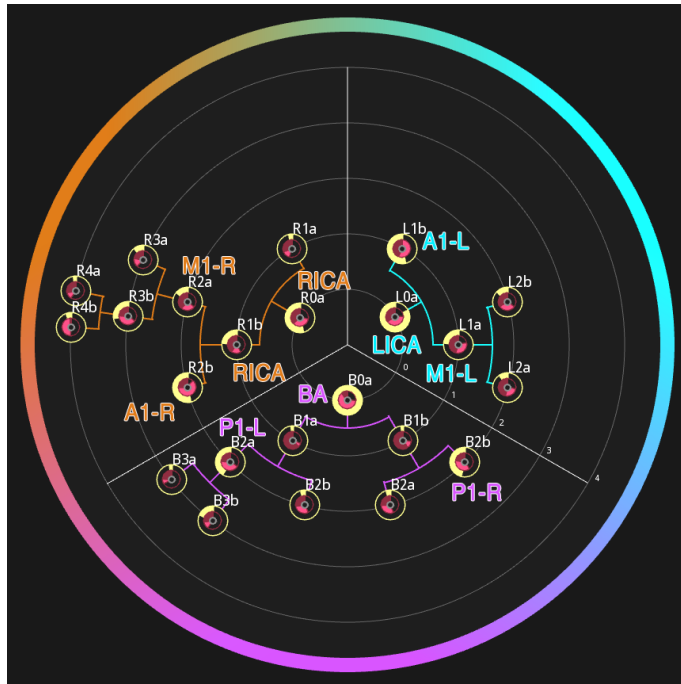
Considering the entire CoW, our approach scored a specificity of about 93%. This value suggests that our methodology is able to detect the absence of arteries. An absent artery can be an indicator for a pathology, such as an occlusion or a total obstruction of blood flow in this artery. Due to the meaningfulness of this information, the high specificity validates our approach. The Figure 4.8 shows an example Cow, where all communicating arteries are missing according to the gold standard. This circumstance is successfully depicted in our radial vessel graph visualization. It shows that the subtrees in the sectors are not connected with each other.

The main reason for the 7% error is caused by a false connection between the left and right anterior subtree. This connection is usually formed by the ACoA. According to the gold standard, the ACoA could not be identified in 33% of the cases. However, the closing operation tends to connect the ACAs, which then can be interpreted as the ACoA. This limitation is discussed in Section 2.5.

The high specificity indicates that our approach has a very good performance in detecting the absence of arteries, which is part of our clustering approach. However, this metric alone is not conclusive if the NPV is not considered as well.



(a) The labeled vessel tree and the transverse MIP.



(b) The radial vessel graph.

Figure 4.8: The Figures (a) and (b) display an example CoW where every segment is correctly identified by our approach. We manually assigned the Latin names in order to show the corresponding segments in our radial vessel graph. In Figure (b) the radial vessel graph displays no connections between the L-, R- and B-sectors, since the ACoA and both PCoAs could not be detected. According to the gold standard these arteries are absent, which is correctly depicted in the radial vessel graph.

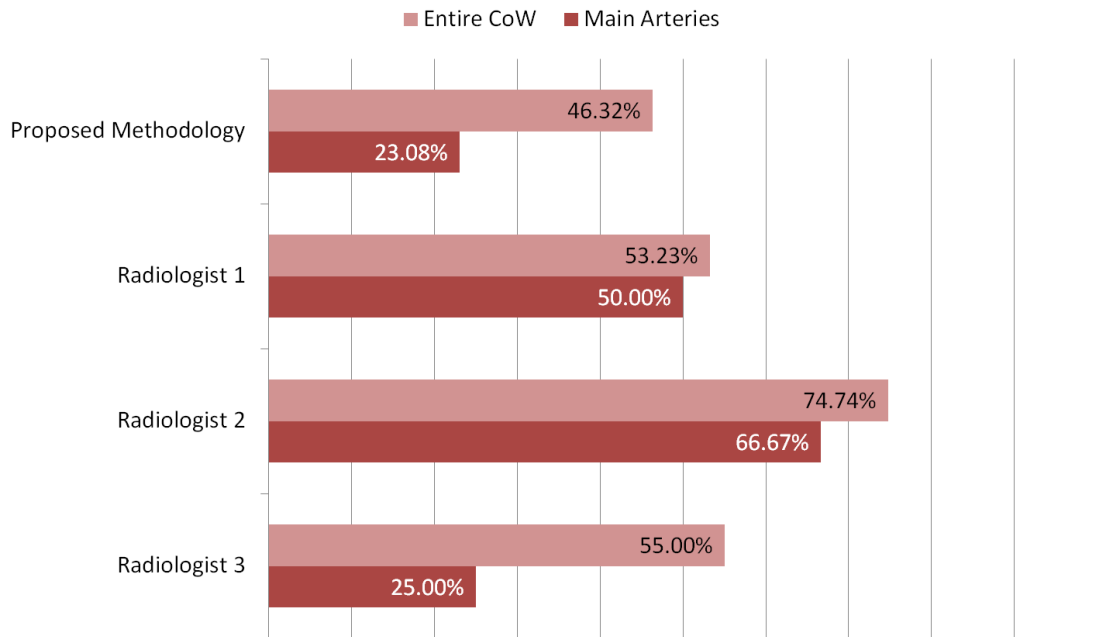


Figure 4.9: The negative predictive value is shown in the figure. This metric is drastically reduced by the FN cases. The NPV seems in general to be quite low, which means that the radiologists and our approach are not as good as the experienced domain expert in handling the low contrast in special cases.

NPV

Figure 4.9 displays the NPV of the main arteries and the entire CoW. Whereas the specificity only measures the percentage of absent arteries that could be detected as such, the NPV measures the correctness of the negative cases by taking the FN cases into account. The reasons for the increase of FN cases are already described in Section 4.1. It seems that our approach is prone to relatively low intensity values in the arteries. However, the figure shows that this value in general is quite low. Compared to the radiologists the proposed methodology has the lowest NPV. This means, that there exist various cases where an artery is considered as absent by our approach but not by the gold standard.

Another limitation of our approach is the method which associates a segment to a subtree. The division of the segments into subtrees depends on the number of branching points that lie between them and the root segment. If the trees are connected by the ACoA, the segment is assigned to the subtree that has the lowest enumerator. This reflects the physiological configuration of the CoW. However, artifacts in the data set can cause an artery to be separated in multiple segments. This results in a high number of branching points and therefore increases the enumerator significantly. As a consequence, the segments are assigned to the wrong subtree. This however, is not a limitation of the radial vessel graph or labeling method but rather of the segmentation approach.

Furthermore, low contrast in the arteries cause problems during the segmentation phase. These arteries are often only partially segmented due to their low intensity values. In some cases, less than two-thirds of an artery were segmented and it was therefore regarded as incorrectly identified. If they are end-segments then they can be potentially recognized as artifacts during the vessel tree pruning step and therefore mistakenly removed. An example is shown in Figure 4.10.

Conclusion

After all, these three metrics suggest that our approach has a good performance compared to radiologists. The sensitivity clearly demonstrates the ability of the approach to identify the arteries. The performance is slightly below the average radiologist.

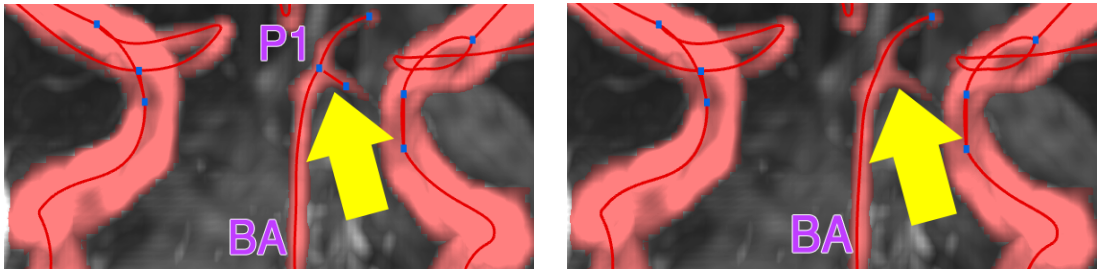
The proposed method scored the highest specificity compared to the radiologists. This validates our approach for the detection of missing arteries. However, the method scored a relatively low NPV. Here, the main difference between the radiologists and this work becomes visible. The radiologists handle uncertainty much better than the applied methods. They seemed to recognize the arteries despite only low intensity differences to the background. Our approach is not able to detect these arteries. A solution to this limitation might be a segmentation approach that considers the local surroundings of an artery too. Nevertheless, the NPV scored by the radiologists is low in general. The biggest mismatch is at the communicating arteries, which are hardly visible.

In conclusion, the overall performance of our proposed methodology can be considered similar to those of the radiologists. None of the absent main arteries were missed by our method. The evaluation showed the proposed methodology is oversensitive in the detection of absent arteries, therefore the lower NPV. Our approach rather detects an artery as *missing* than *present*.

Individual Artery Evaluation

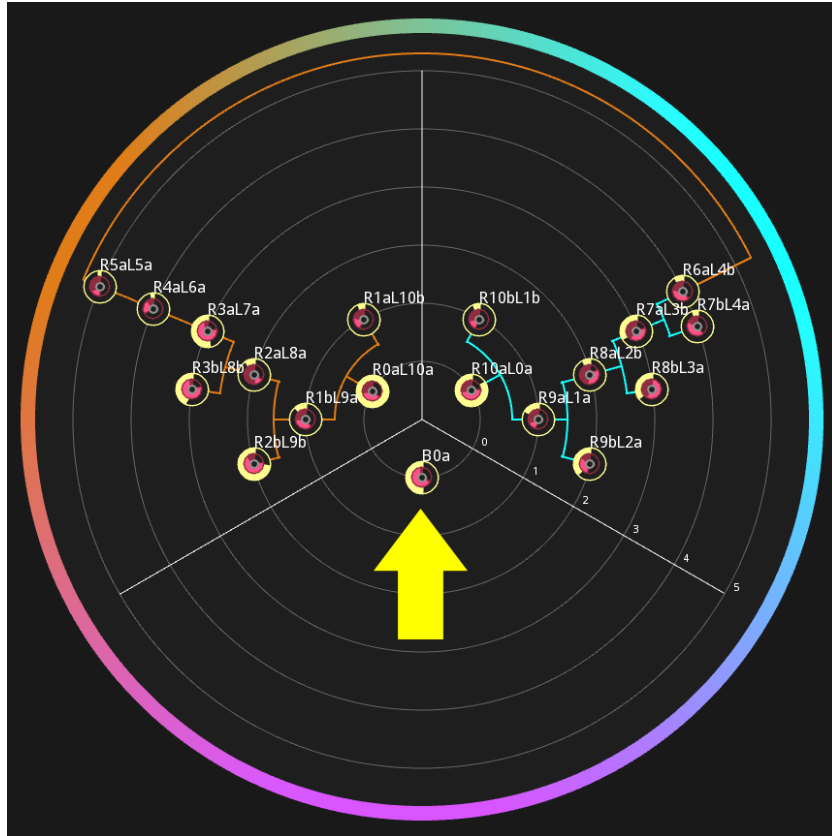
Figure 4.11 shows the scored metrics for the individual arteries. As comparison, the sensitivity, specificity and NPV of the radiologists' results are shown in Figures 4.12, 4.13 and 4.14. We can see that in all cases the highest sensitivity is achieved in the main arteries. They are identified using the approach described in Section 3.2. We described a method that identifies the main arteries by their characteristic attributes. The radiologists and the proposed methodology seem to perform similarly well. These arteries are the largest in the CoW and are normally represented by the highest intensity values. Therefore, they are easy to identify for the radiologists. Nevertheless, occlusions in the main artery seem to cause disagreement between the radiologists and the gold standard. For example, the RICA of the CoW shown in Figure 4.4 is considered to be present by the gold standard. The RICA is not visible in the transverse MIP, even by using a heat map. This artery is therefore regarded as missing by the radiologists as well as by our proposed methodology. Cases like this decrease the NPV drastically.

The lowest scores are achieved for the ACoA. As Figure 4.6 (a) shows, it is a relatively short and thin artery that appears with low contrast in the TOF-MRA data. In numerous cases, the segmentation algorithm seem to fail to detect this artery due to an overestimated threshold. Another reason for the low sensitivity and NPV at the ACoA are the FN detections. The ACoA bifurcates from the ACAs, which have a pathway very close to each other. The closing operation during the morphological step merges the two ACAs and falsely forms a connection between



(a) Before removal of short end-segments.

(b) After removal of short end-segments.



(c) The radial vessel graph.

Figure 4.10: The figures display an example CoW, where the right P1 segment is missing and the left P1 segment is hypoplastic according to our domain expert. Figures (a) and (b) display the coronal view of the vessel tree. In (a) the arrow points to a particular short end-segment, which is the left superior cerebellar artery. It is removed due to its shortness and the result is shown in Figure (b). Since the CoW has no right P1 segment, the two remaining consecutive segments are merged into one. As a result, the branching point between the BA and the left P1 segment is removed. Even though our approach initially detected this segment, it is merged after the removal of the superior cerebellar artery. Since the bifurcation is not detected, the left P1 segment is therefore regarded as incorrectly identified. The radial vessel graph in (c) shows that only one segment is detected in the posterior subtree.

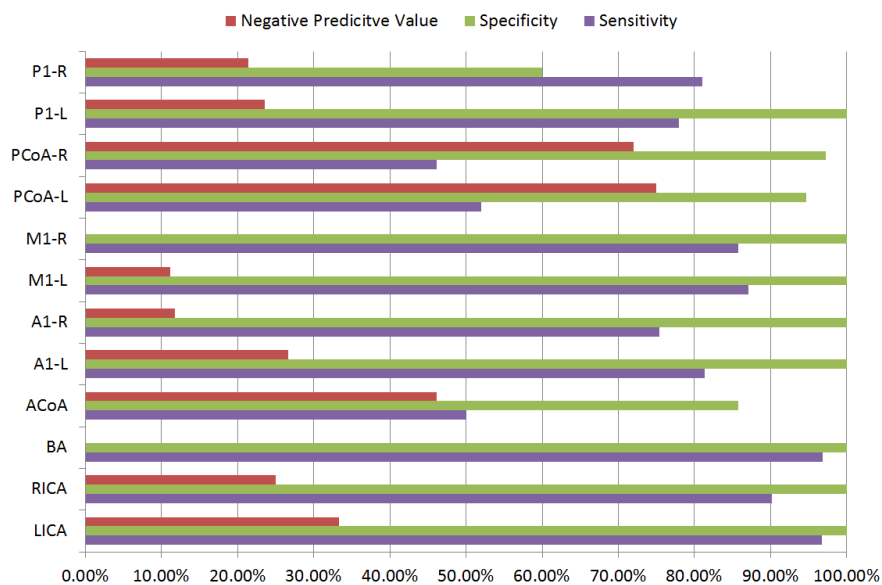


Figure 4.11: The figure shows the performance for each artery of the proposed methodology.

the left and right anterior parts. This circumstance is demonstrated in Figure 4.6. The scores achieved by the radiologists are also the lowest at the ACoA. According to our domain expert this artery is rather difficult to detect.

In general, the performance seems to be the lowest with the communicating arteries. The reason for this limitation is related to the low contrast or artifacts in the volume. The sensitivity and NPV of our approach at the A1 segments are rather low compared to those of the radiologists. One explanation for this circumstance is the failure in the subtree division, which is based on the enumerator of the segments. The A1 segments are assigned to the wrong subtree, which is then counted as incorrectly identified. The explanation for this case has already been given above for the reduction of the sensitivity. Furthermore, the performance for the A1 and M1 segments seems to drop in a small subset of the studied data sets. These data sets have a different volume size compared to the rest and the CoW lies in a different location inside the volume. For this reason, the automated ROI placement is inaccurate due to the deviating ratio between the CoW's location and the volume size. This limitation has already been discussed in the Section 3.1. An example is shown in Figure 4.15 (b), where the ROI is placed too low by our automated method. The A1 segment, being the segment with the highest location in the CoW, is left out of the ROI. Another problem with these data sets is the poor contrast. The arteries of the CoW have relatively low intensity values and are hardly distinguishable from the surrounding soft tissue or veins. An example is shown in Figure 4.16. In this case, only the main arteries could be segmented.

In conclusion, the sensitivity, specificity and NPV seem to vary between the different arteries. The main arteries are easily identified by our approach, but the communicating arteries are often not detected. The low NPV demonstrates the limitations of our approach. Despite the limitations, the overall outcome of the study is positive and validates our approach. The follow-

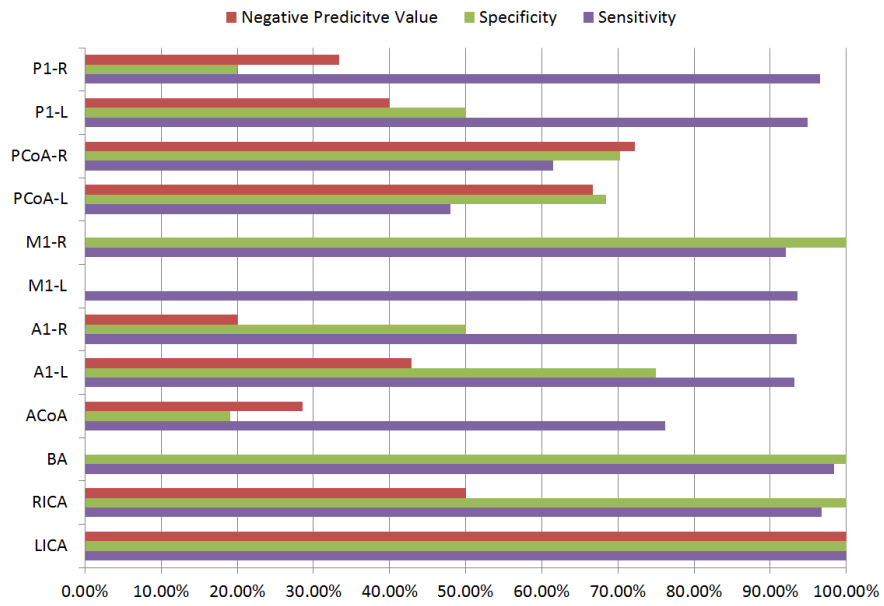


Figure 4.12: The figure shows the performance for each artery of radiologist 1.

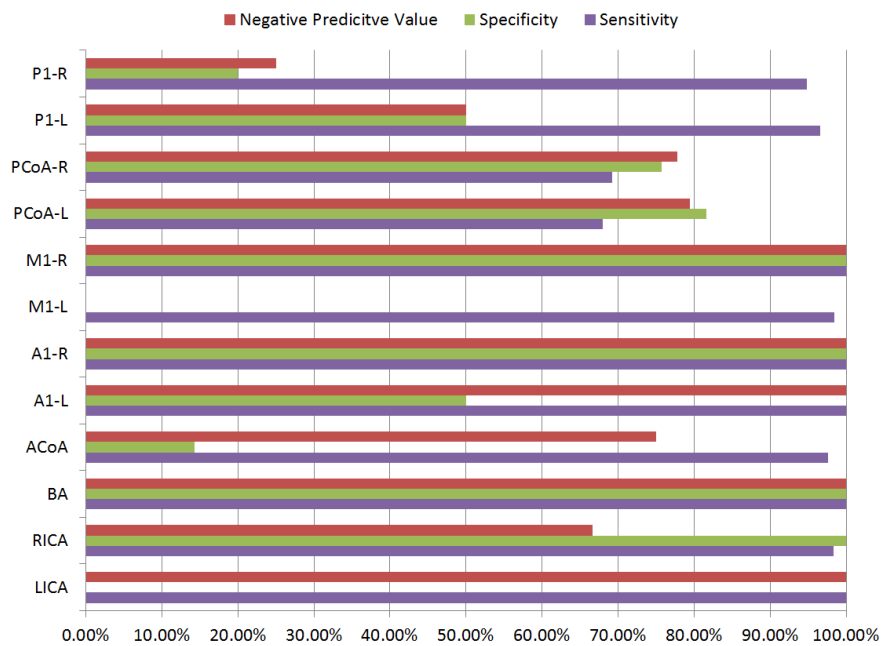


Figure 4.13: The figure shows the performance for each artery of radiologist 2.

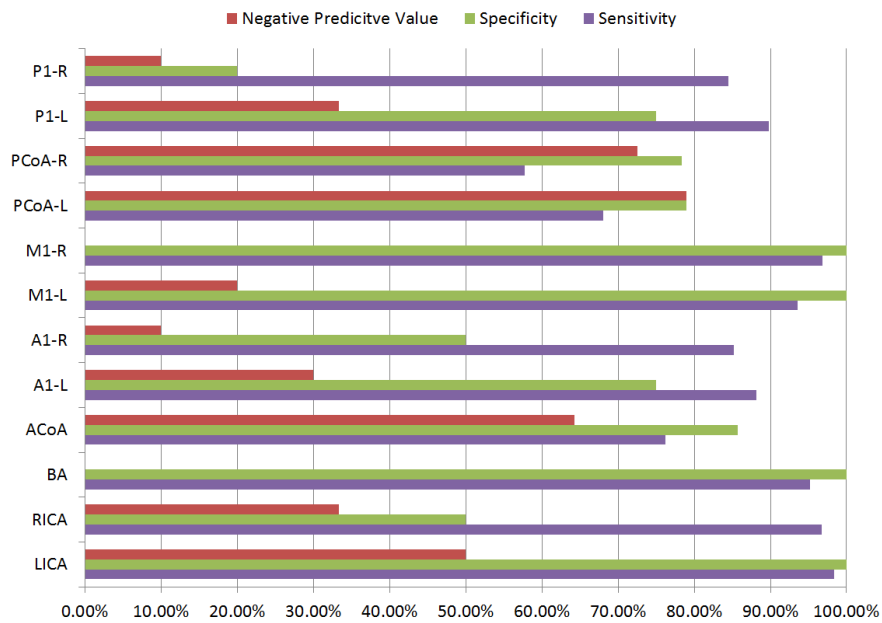
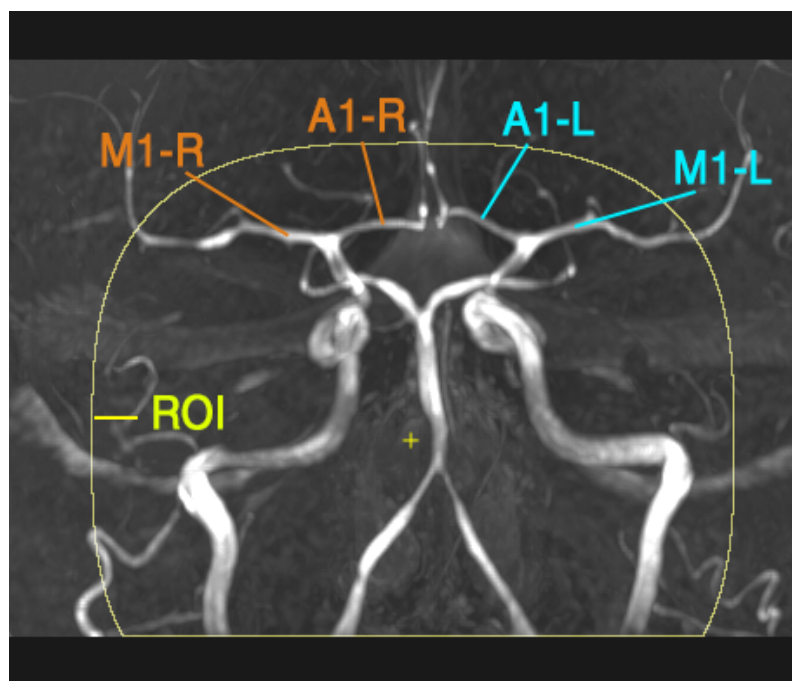
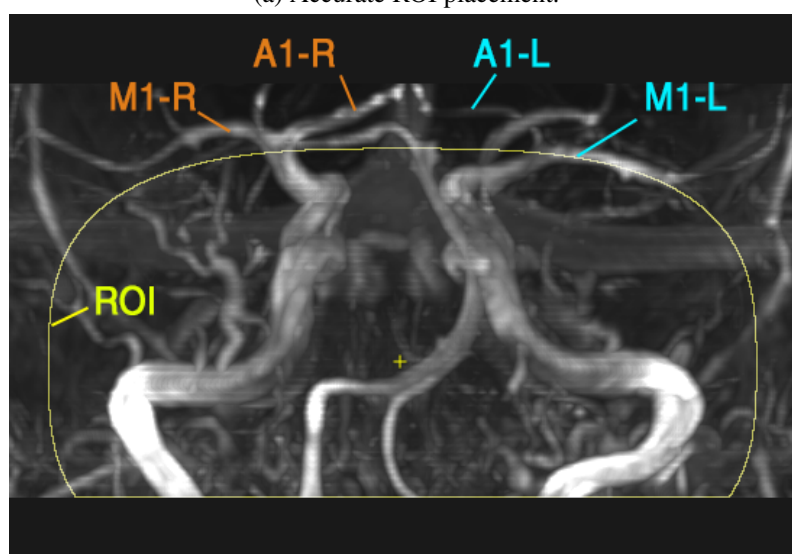


Figure 4.14: The figure shows the performance for each artery of radiologist 3.

ing scenario puts the limitations into perspective: The radiologist is interested in retrieving all data sets, where the RICA is absent. Instead of investigating the raw data of all 63 data sets, he applies our approach, which automatically processes these 63 data sets. In the resulting radial vessel graphs, he quickly finds 8 cases where the RICA could not be identified. He reduced the number of data sets he has to investigate from 63 to 8. In 2 of the 8 data sets, the RICA is truly missing (hence the 25% NPV) and the remaining 6 are FN cases. Figure 4.19 displays these 8 data sets. It can be seen, that in at least 5 cases, there is some abnormality with the RICA since it is not recognizable. Hence, these data sets can still be of interest to the radiologist.

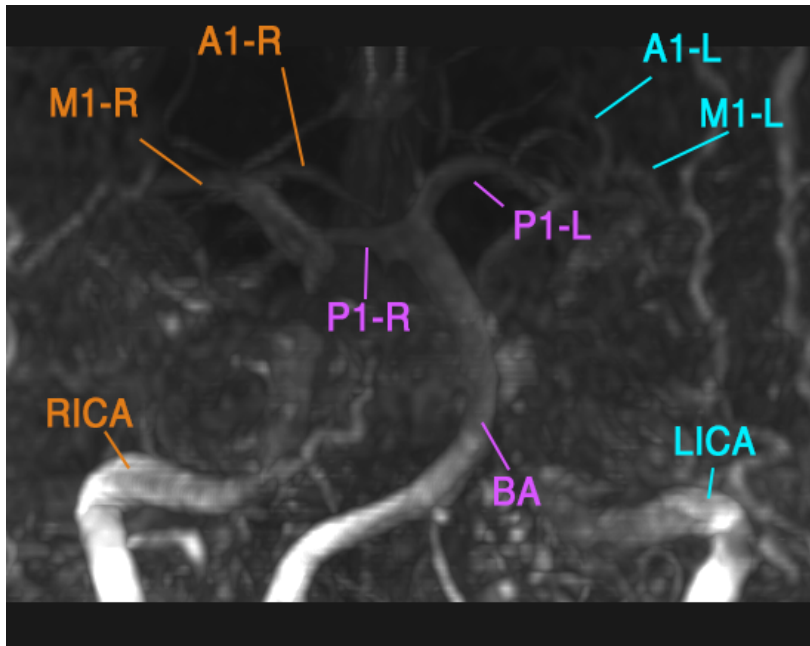


(a) Accurate ROI placement.

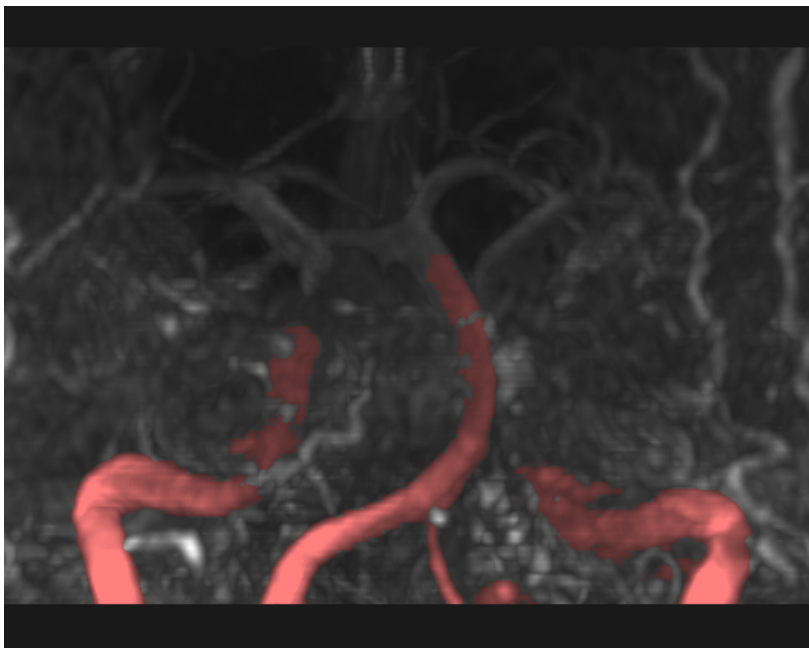


(b) Inaccurate ROI placement.

Figure 4.15: The Figures (a) and (b) display the result of our automated ROI placement method in the coronal view. In the majority of cases, the automated placement is accurate. (a) demonstrates such an example. The entire CoW is inside the ROI. However, due to a change in the ratio between volume size and the CoW's location, the ROI can be placed too low, which is demonstrated in (b). As the figure shows, the left A1, the right A1 and the right M1 segments are outside of the ROI. As a consequence, they can not be correctly identified by our approach.



(a) An example poor contrast.



(b) Segmentation result.

Figure 4.16: Figure (a) shows the coronal MIP of a data set with low contrast. The low contrast causes problems for our segmentation approach. The result is shown in (b). Only the main arteries could be segmented.

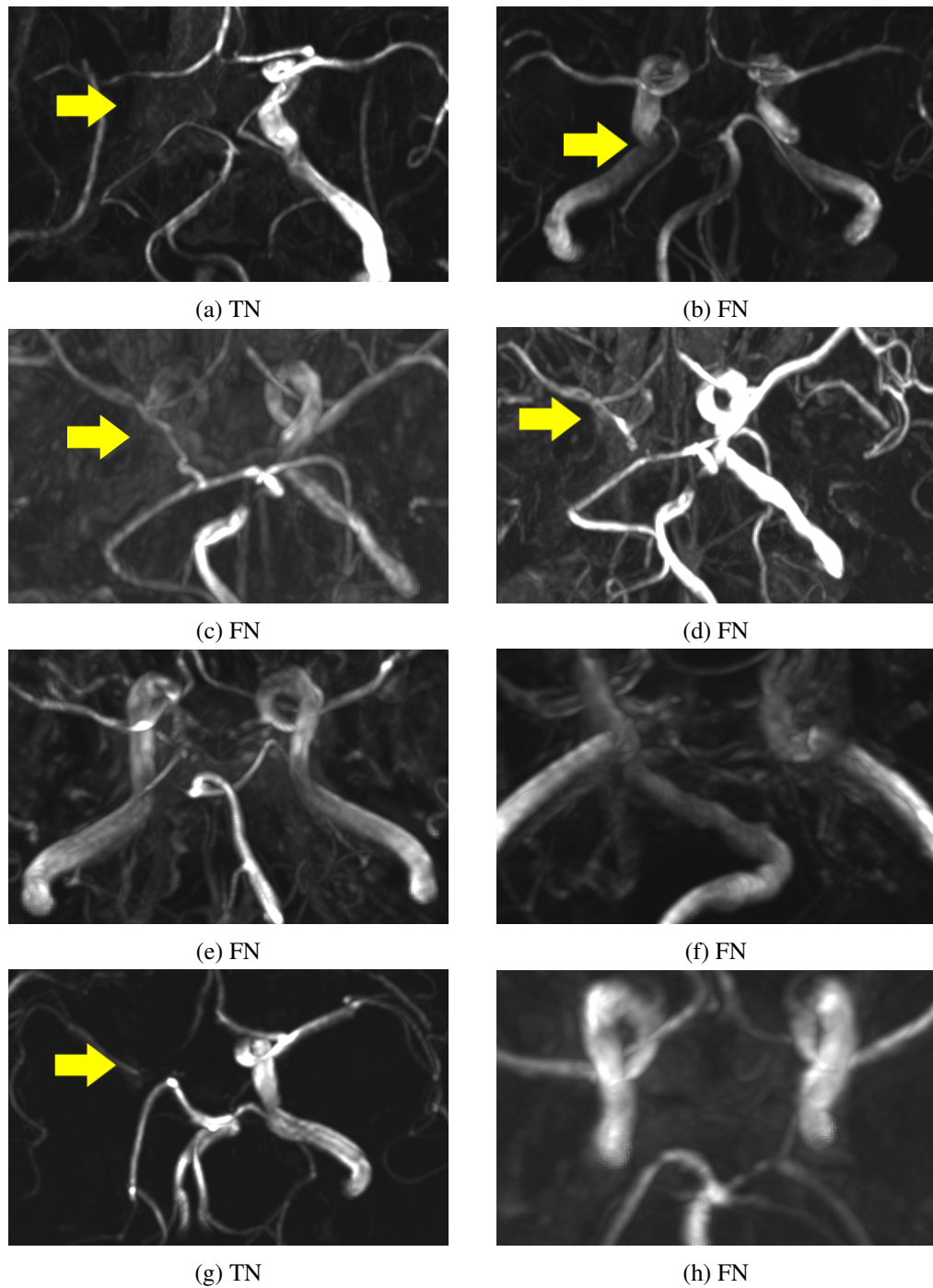


Figure 4.17: The cases where the RICA is detected as missing by our approach. They are compared to the gold standard and considered either a TN or FN case. (a) and (g) were correctly identified by our approach. Figures (c) and (d) show that the RICA is not recognizable, but still regarded as present by the gold standard. In (b) the RICA is disconnected. In (e), (f) and (h) the arteries could not be segmented due to low contrast.

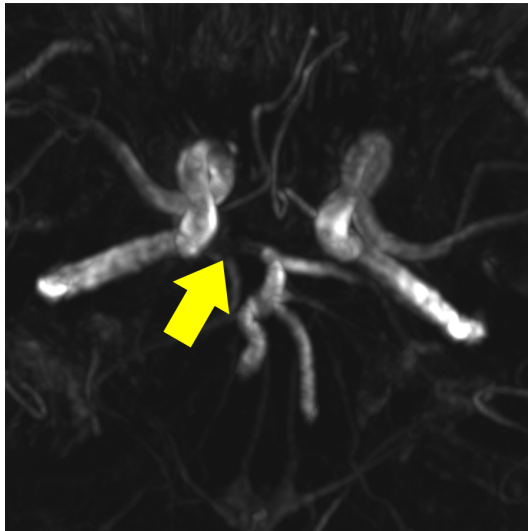
4.2 Application of the Proposed Methodology

63 data sets were automatically processed by our methodology. The proposed method in this work is demonstrated on an example in Chapter 3, where different intermediate results are shown. The benefits and limitations of our approach have already been demonstrated in the previous section with different examples from the studied data sets. For demonstration purposes, the results of two other data sets are investigated in this section. The first example scored good results and demonstrates the effectiveness of the proposed methods. The majority of the data sets in the study are similar to this example. In the second example, the limitations of this work are demonstrated. Both data sets have a volume size of $512 \times 512 \times 156$ with voxel dimensions of $0.37 \times 0.37 \times 0.5mm^3$.

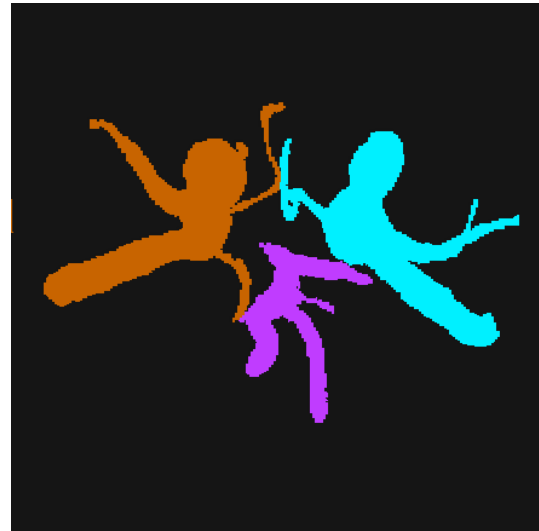
Demonstration

In the first example, all arteries of the CoW are present except for the left PCoA according to the gold standard. Figure 4.18 shows the transverse MIP, the segmentation and clustering result, the labeled vessel tree and the resulting radial vessel graph. Figure 4.18 (a) displays the transverse MIP. According to the gold standard, the left PCoA is the only absent artery. The intensity values at the right P1 segment are low compared to the other arteries as indicated by the arrow. As a result it is not segmented as shown in Figure 4.18 (b). The volume is segmented with a ROI size of $117 \times 103 \times 249$ voxels and thresholds of $t_h = 443$ and $t_l = 255$. In Figure 4.18 (b) the division of the segmentation result into the subtrees is shown. The orange colored part shows the right anterior subtree, the cyan colored part shows the left anterior tree and the violet part displays the posterior subtree. Figure 4.18 (c) illustrates the extracted vessel tree model in the coronal view. The RICA (R0aL7a), the LICA (R7aL0a) and BA (B0a) are correctly identified. The radial vessel graph is visualized in Figure 4.18 (d). The three root segments are placed at the level 0 of the radial vessel graph. A connection between the two anterior subtrees is indicated by the cyan colored arc edge, which is formed by the ACoA. In the B-sector the BA bifurcates into two segments. One is the left P1 segment. The other segment is the superior cerebellar artery. The right P1 segment could not be identified due to low intensity values. The right PCoA is also correctly detected but not represented by a connection to the B-sector since the right P1 segment is not correctly identified.

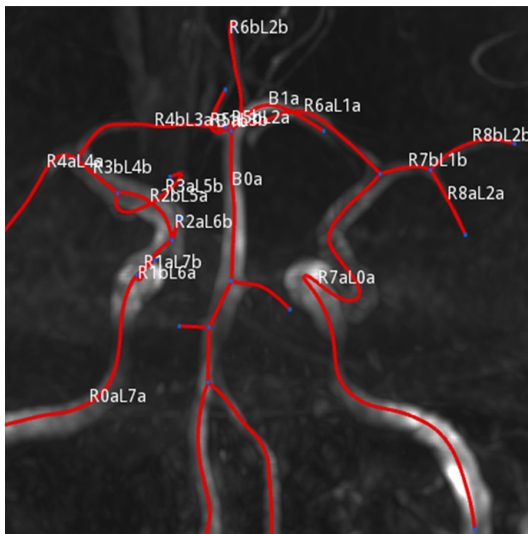
The second example in the Figures 4.19 (a), (b), (c) and (d) partially demonstrate the limitations of the proposed methodology. According to the gold standard, the LICA can not be identified. The only other missing artery is the ACoA. If our approach detects a missing root segment, the entire subtree will be regarded as missing. But this is false since the left M1, A1 and PCoA are present according to the gold standard. The arrow in Figure 4.19 (a) points to the position where the LICA is usually located. The absence of this artery is detected by our clustering method. The labeled vessel tree is displayed in Figure 4.19 (c). Due to the missing LICA, the entire left anterior subtree is neither segmented nor labeled. Furthermore, the segments only carry one labeling term since the right PCoA could not be correctly identified by our approach. The visualized radial vessel graph is shown in Figure 4.19 (d). There, the L-sector is empty. Examples like this increase the FN cases tremendously, since our approach depends on the identification of the root segment.



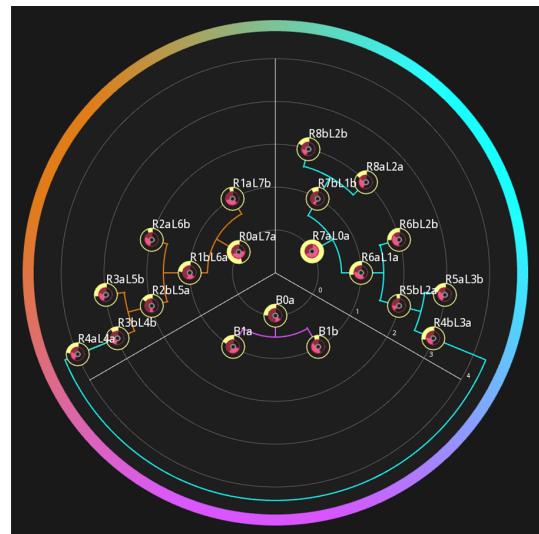
(a) Transverse MIP.



(b) Segmentation and clustering result.

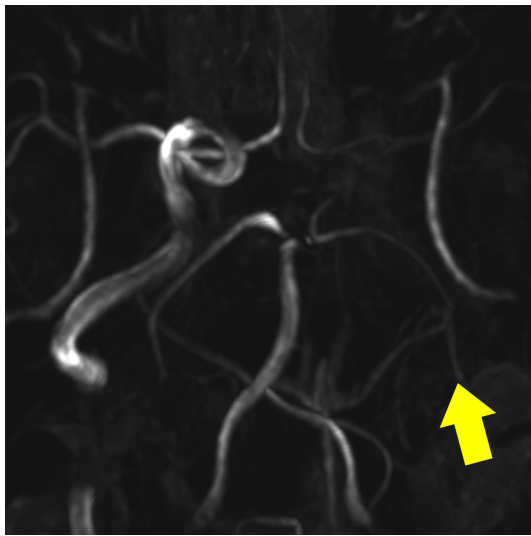


(c) Labeled vessel tree.

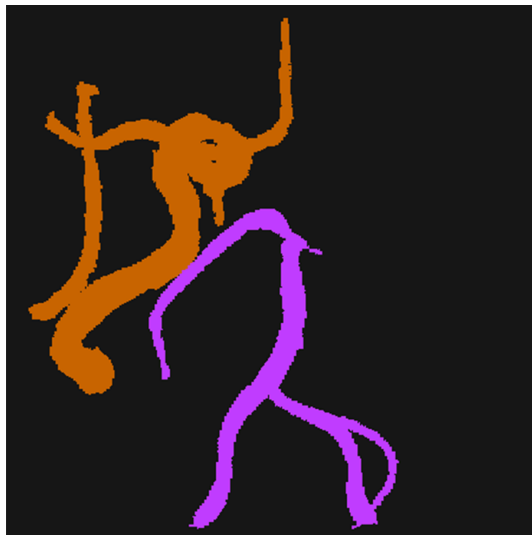


(d) Radial vessel graph.

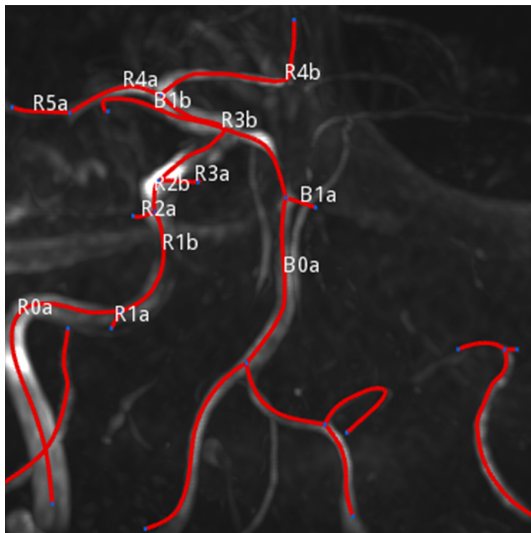
Figure 4.18: The figures display an example that shows good results for our proposed methodology. For a better view, the vessel tree in Figure (c) is shown from the coronal perspective. In this subject 91% of the arteries could be correctly identified with the proposed methodology.



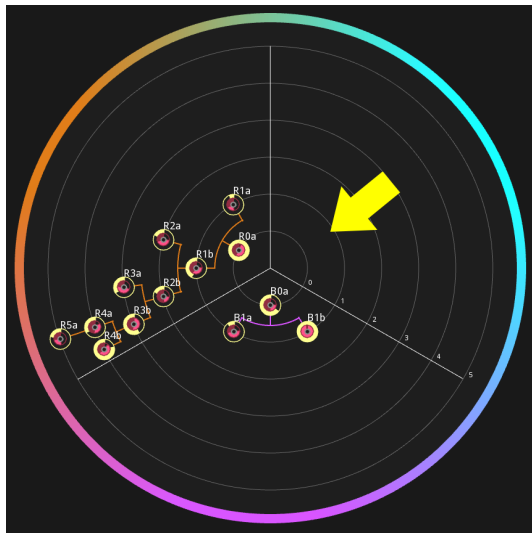
(a) Transverse MIP.



(b) Segmentation and clustering result.



(c) Labeled vessel tree.



(d) Radial vessel graph.

Figure 4.19: The figures display an example that demonstrates the limitations of our approach. The vessel tree in Figure (c) is shown from the coronal perspective. In this subject only 58% of the arteries could be correctly identified with the proposed methodology.

According to the gold standard, 115 out of the 756 arteries are missing. Because of the relatively small number of absent arteries in the gold standard, the FN detection of an entire subtree can reduce the NPV drastically.

4.3 Discussion and Limitation

The bottleneck of the proposed method is the detection of the root segments for each subtree. An incorrectly detected segment causes the entire subtree to be labeled wrongly. Furthermore, disconnections inside the main arteries cause the same problem since the enumeration during the labeling step stops at the disconnection. These disconnections can result from stenoses or artifacts. In both cases, the respective subtree is not reached during the enumeration causing it to be excluded from the final visualization. These arteries are consequently not shown in the radial vessel graph. On the one hand, an entire subtree is not detected and therefore not visible in the radial vessel graph. As discussed before, the FN cases are increased. On the other hand, it also indicates an abnormality in the CoW, which potentially provides valuable information.

In the study, the proposed methodology is compared to the performance of the radiologists leading to the conclusion that our approach seems very promising and worth to be further investigated. Especially the high specificity suggests an extensive detection rate of missing arteries. The high specificity is hampered by the low NPV. There is a fundamental difference between the methods applied by the radiologists and the proposed method. Whereas the radiologist draws on prior knowledge about the CoW, the proposed method mostly relies on what is actually present in the data set and cannot detect arteries that are not represented with sufficiently high intensity values. Prior knowledge about the shape, location and length of the main arteries is encoded and applied during the labeling phase. However, only little prior knowledge is applied during the segmentation phase. This makes the identification of the communicating arteries a challenging task. Especially the identification of the ACoA requires an experienced radiologist. In general, it seems that our approach is more prone to artifacts in TOF-MRAs than the radiologists. They seem to handle uncertainty and incomplete information much better.

In order to create an effective visualization of the CoW, it is necessary to extract the underlying model. We consider this part as the quantification of the CoW. The quantification of the arteries in the CoW is a challenging task and consists of different aspects. This work is not focused on one particular aspect but rather on the entire pipeline, which is necessary to visually quantify the CoW. For future work, single steps in this pipeline can be replaced by other approaches. Improved intermediate results would also enhance the final visualization.

The proposed radial vessel graph is suggested to be a complementary display during the diagnostic process. The feasibility of such a visualization in a clinical environment was not subject of the study, even though the outcome of the study seems quite promising.

Conclusion and Outlook

5.1 Conclusion

In this thesis a novel approach for the visual quantification of the CoW is presented. This arterial circle is of particular interest due to its affiliation to cerebral vascular diseases. The analysis of the cerebral arteries is a rather complex process. In clinical practice, the computer is currently simply used as a display medium but does not provide assistance in recognizing the configuration of the CoW. This opens a possibility where the visualization aims to provide complementary information for the radiologist rather than replacing the traditional methods.

This work applies well-known methods from the field of image processing as well as introduces novel methods for the visual quantification of the CoW. Among others, a method for the identification of the main arteries, based on the analysis of the transverse, coronal and sagittal planes of the volume is described. The extracted main arteries constitute the basis for the labeling of the CoW's vascular model. Thereby, a solution based on the enumeration of arterial segments is proposed. This approach differs from state-of-the-art methods since it does not focus on finding the Latin names of the arteries but rather aims to describe their topology. This is based on the theory that the arteries can be immediately identified by affiliating them to the main arteries.

In the second part, particular attention is paid to the effective visualization of the CoW. This work introduces a standardized visualization method that uses the radial tree layout to represent the three subtrees of the CoW. We refer to this standardized visualization method as the radial vessel graph, where a main artery forms the root of each subtree. The labeled vessel tree provides the underlying data for this visualization. This visualization of the CoW offers an abstract display of the CoW's topology that could be potentially used for the visual indication of problematic areas. The second application of this standardized method addresses the possibility of an overview comparison between different CoWs using the radial vessel graph instead of traditional display methods such as MIP or slice views.

The feasibility of the described methods is demonstrated in a study of 63 subjects. The proposed methodology is compared to the performance of three radiologists. From the study's

outcome it can be concluded that the performance of the proposed methodology is matchable to the ones of the radiologists. The absence of arteries can be detected with high specificity. This suggests that our proposed methodology is worth investigating further.

5.2 Future Work

This work presents an automated method to visually describe a patient's CoW. The main concern is the automation of the pipeline. An interactive method where the expertise of the radiologist is consulted would allow a considerable improvement of the quantification result. However, the practical feasibility of an interactive method for clinical practice has not been part of this work and remains to be addressed.

A common challenge with fully automated methods is generality. This means that the proposed methods have to be able to consider standard as well as special cases. Considering the high variance of the CoW and the fact that stroke patients usually represent exceptions, each method has to be very robust. This is the key limitation of this work. As the proverb says, a chain is only as strong as its weakest link. If only one step in the pipeline fails or provides insufficient results, the quality of the final visualization will be affected. Future work could include the replacement of the weakest links in the pipeline with other approaches. Currently, our segmentation approach processes the majority of the provided data sets with little errors. However, it is limited by low contrast or artifacts in the volume. In this work, we proposed a pipeline for the visually description of the CoW. Of course, some steps can be done differently than we proposed. However, our focus was on the entire pipeline that is required for a visual quantification of the CoW instead of certain aspects.

Since the developed application does not introduce new work steps, it has great potential to be applied in clinical practice. The most promising application scenario is the automated construction of a data base. According to our domain expert, there are thousands of volumes saved on their PACS. Once a scan is investigated by a radiologist, it is normally archived. In order to retrieve a requested volume, numerous data sets have to be manually investigated, which is very time-consuming. Here, the automated processing capabilities of the software developed for this work can be most helpful. The enumeration method used for the labeled vessel tree and the standardized visualization are possible abstractions of the CoW and can be utilized to reduce a data set to a number of images. For future work, the proposed methodology could be applied to build a data base where every CoW is visually quantified using the described approaches and the radial vessel graph is taken as a thumbnail display of a patient's CoW. This enables the comparison of numerous CoWs with a standardized method. It would allow drawing conclusions from a broad spectrum of patients.

Bibliography

- [1] S. Aylward, E. Bullitt, S. Pizer, and D. Eberly. Intensity ridge and widths for tubular object segmentation and description. In *Proceedings of IEEE Workshop Mathematical Methods in Biomedical Image Analysis 1996*, pages 131–138, 1996.
- [2] M. Bilgel, S. Roy, A. Carass, P. A. Nyquist, and J. L. Prince. Automated anatomical labeling of the cerebral arteries using belief propagation. In *Proceedings of SPIE 8669, Medical Imaging 2013: Image Processing*, 2013.
- [3] C. M. Bishop. *Pattern Recognition and Machine Learning*. Springer, 2006.
- [4] H. Bogunovic. *Geometric Modeling and Characterization of the Circle of Willis*. PhD thesis, Universitat Pompeu Fabra, 2012.
- [5] E. Bullitt, S. Aylward, Liu, J. Stone, S. K. Mukherji, C. Coffey, G. Gerig, and S. M. Pizer. 3D graph description of the intracerebral vasculature from segmented MRA and tests of accuracy by comparison with x-ray angiograms. In *Information Processing in Medical Imaging*, volume 1613 of *Lecture Notes in Computer Science*, pages 308–321. Springer, 1999.
- [6] E. Bullitt, G. Gerig, S. M. Pizer, W. Lin, and S. R. Aylward. Measuring tortuosity of the intracerebral vasculature from MRA images. *IEEE Transactions on Medical Imaging*, 22(9):1163–1171, 2003.
- [7] E. Bullitt, K. E. Muller, I. Jung, W. Lin, and S. Aylward. Analyzing attributes of vessel populations. *Medical Image Analysis*, 9(1):39–49, 2005.
- [8] J. Canny. A computational approach to edge detection. *IEEE Transactions on Pattern Analysis and Machine Intelligence*, 8(6):679–698, 1986.
- [9] J. A. Chalela, C. S. Kidwell, L. M. Nentwich, M. Luby, J. A. Butman, A. M. Demchuk, M. D. Hill, N. Patronas, L. Latour, and S. Warach. Magnetic resonance imaging and computed tomography in emergency assessment of patients with suspected acute stroke: a prospective comparison. *The Lancet*, 369(9558):293–298, 2007.
- [10] A. Charnoz, V. Agnus, G. Malandain, L. Soler, and M. Tajine. Tree matching applied to vascular system. In *Graph-Based Representations in Pattern Recognition*, volume 3434 of *Lecture Notes in Computer Science*, pages 183–192. Springer, 2005.

- [11] A. Condurache and T. Aach. Vessel segmentation in angiograms using hysteresis thresholding. In *Proceedings of the IAPR Conference on Machine Vision Applications 2005*, pages 269–272, 2005.
- [12] G. A. Donnan, M. Fisher, M. Macleod, and S. M. Davis. Stroke. *The Lancet*, 371(9624):1612–1623, 2008.
- [13] R. Donner, S. Haas, A. Burner, M. Holzer, H. Bischof, and G. Langs. Evaluation of fast 2D and 3D medical image retrieval approaches based on image miniatures. In *Medical Content-Based Retrieval for Clinical Decision Support*, volume 7075 of *Lecture Notes in Computer Science*, pages 128–138. Springer, 2012.
- [14] R. Donner, B. H. Menze, H. Bischof, and G. Langs. Fast anatomical structure localization using top-down image patch regression. In *Medical Computer Vision. Recognition Techniques and Applications in Medical Imaging*, volume 7766 of *Lecture Notes in Computer Science*, pages 133–141. Springer, 2013.
- [15] M. Dorfer, R. Donner, and G. Langs. Constructing an un-biased whole body atlas from clinical imaging data by fragment bundling. In *Medical Image Computing and Computer-Assisted Intervention*, volume 8149 of *Lecture Notes in Computer Science*, pages 219–226. 2013.
- [16] G. M. Draper, Y. Livnat, and R. F. Riesenfeld. A survey of radial methods for information visualization. *Visualization and Computer Graphics, IEEE Transactions on*, 15(5):759–776, 2009.
- [17] Nifti Data Format. <http://nifti.nimh.nih.gov/>, April 2015.
- [18] The AngioVis framework. <http://www.angiovis.org/>, April 2015.
- [19] Universitätsklinikum Tulln Institut für Radiologie. <http://www.tulln.lknoe.at/abteilungen/institut-fuer-radiologie.html>, April 2015.
- [20] E. Gansner. and S. C. North. An open graph visualization system and its applications to software engineering. *Software Practice and Experience*, 30(11):1203–1233, 2000.
- [21] Graphviz. <http://www.graphviz.org/>, April 2015.
- [22] M. J. Hartkamp and J. van der Grond. Investigation of the circle of Willis using MR angiography. *MedicaMundi*, 44(1):20–27, 2000.
- [23] M. Hernandez and A. Frangi. Non-parametric geodesic active regions: Method and evaluation for cerebral aneurysms segmentation in 3DRA and CTA. *Medical Image Analysis*, 11(3):224–241, 2007.
- [24] What is Stroke - American Stroke Association. http://www.strokeassociation.org/STROKEORG/AboutStroke/About-Stroke_UCM_308529_SubHomePage.jsp, April 2015.

- [25] K-Means. <http://de.wikipedia.org/wiki/K-Means-Algorithmus>, April 2015.
- [26] C. Kirbas and F. K. H. Quek. Vessel extraction techniques and algorithms: A survey. In *Proceedings of Third IEEE Symposium on Bioinformatics and Bioengineering*, pages 238–245, 2003.
- [27] G. Langs, R. Donner, P. Peloschek, and H. Bischof. Robust autonomous model learning from 2D and 3D data sets. *Medical Image Computing and Computer Assisted Intervention*, pages 968–976, 2007.
- [28] DOT Graph Description Language. [http://en.wikipedia.org/wiki/DOT_\(graph_description_language\)](http://en.wikipedia.org/wiki/DOT_(graph_description_language)), April 2015.
- [29] T.-C. Lee, R. L. Kashyap, and C.-N. Chu. Building skeleton models via 3-D medial surface/axis thinning algorithms. *Graphical Models and Image Processing*, 56(6):462–478, 1994.
- [30] S. P. Lloyd. Least squares quantization in PCM. *IEEE Transactions on Information Theory*, 28(2):129–137, 3 1982.
- [31] C. Lundstrom, P. Ljung, A. Persson, and A. Ynnerman. Uncertainty visualization in medical volume rendering using probabilistic animation. *IEEE Transactions on Visualization and Computer Graphics*, 13(6):1648–1655, 2007.
- [32] G. Mistelbauer. Automated processing and visualization of vessel trees. Master’s thesis, Vienna University of Technology, 2010.
- [33] G. Mistelbauer. *Smart Interactive Vessel Visualization in Radiology*. PhD thesis, Vienna University of Technology, 2013.
- [34] Circle of Willis Illustration. http://en.wikipedia.org/wiki/File:Circle_of_Willis_en.svg, April 2015.
- [35] M. Piccinelli, S. Bacigaluppi, E. Boccardi, B. Ene-Iordache, A. Remuzzi, A. Veneziani, and L. Antiga. Geometry of the ica and recurrent patterns in location, orientation and rupture status of lateral aneurysms: An image-based computational study. *Neurosurgery*, 68(5):1270–1285, 2011.
- [36] T. Pock. Robust segmentation of tubular structures in 3D volume data. Master’s thesis, Graz University of Technology, 2004.
- [37] B. Preim. *Visual Computing for Medicine*. Elsevier, 2013.
- [38] G. Ristovski, T. Preusser, H. K. Hahn, and L. Linsen. Uncertainty in medial visualization: Towards a taxonomy. *Computer & Graphics*, 39(0):60–73, 2013.
- [39] Z. I. Salah. *Segmentation and Illustrative Visualization of Medical Data*. PhD thesis, Eberhard-Karls-Universität Tübingen, 2006.

- [40] R. Schernthaner, D. Fleischmann, A. Stadler, M. Schernthaner, J. Lammer, and C. Loewe. Value of MDCT angiography in developing treatment strategies for critical limb ischemia. *Vascular and Interventional Radiology May 2009*, 192(5):1416–1424, 2009.
- [41] M. Straka. *Processing and Visualization of Peripheral CT-Angiography Datasets*. PhD thesis, Vienna University of Technology, 2006.
- [42] Superellipsoid. <http://en.wikipedia.org/wiki/Superellipsoid>, April 2015.
- [43] R. Tamassia. *Handbook of Graph Drawing and Visualization*. CRC Press, 2014.
- [44] W. Tang and A. Chung. Cerebral vascular tree matching of 3D-RA data based on tree edit distance. In *Medical Imaging and Augmented Reality*, volume 4091 of *Lecture Notes in Computer Science*, pages 116–123. Springer, 2006.
- [45] World Health Organization The top 10 causes of death. <http://www.who.int/mediacentre/factsheets/fs310/en/>, April 2015.
- [46] Cagatay Uston. Neurowords Dr. Thomas Willis’ famous eponym: The Circle of Willis. *Journal of the History of the Neurosciences: Basic and Clinical Perspectives*, 14(1):16–21, 2005.